

Mars Entry Simulation of Slotted Compression Ramp Probe

A project present to
The Faculty of the Department of Aerospace Engineering
San Jose State University

in partial fulfillment of the requirements for the degree
Master of Science in Aerospace Engineering

by

Anthony DiQuattro

May, 2018

approved by

Dr. P. Papadopoulos
Faculty Advisor



San José State
UNIVERSITY

ABSTRACT

MARS ENTRY SIMULATION OF SLOTTED COMPRESSION RAMP PROBE

by Anthony DiQuattro

This report summarizes parametric geometry design, reacting hypersonic computational fluid dynamics simulations, heating and trajectory analysis performed using the Slotted Compression Ramp (SCRAMP) probe geometry for a Mars entry mission.

TABLE OF CONTENTS

1	INTRODUCTION	1
	1.1 Background.....	1
	1.2 Previous Work.....	2
	1.3 Objective.....	7
2	SIMULATION SETUP	8
	2.1 Geometry Parameterization.....	8
	2.2 Test Case Selection.....	11
	2.3 Hypersonic Flow Field Modeling.....	13
	2.4 Reacting Flow.....	14
3	AERODYNAMIC RESULTS	16
	3.1 Newtonian Approximation.....	16
	3.2 Simulation Results.....	16
	3.3 Analysis.....	17
4	THERMAL PROPERTIES & TRAJECTORY ANALYSIS	21
	4.1 Heat Load Calculation.....	21
	4.2 Simulation Analysis.....	23
	4.3 Trajectory Parametric Study.....	25
5	CONCLUSION	27
	REFERENCES	29
	APPENDIX	
	A Simulation Result Data Plots	32
	B Geometry Parametric Surface Plots	45
	C Body Parameterization Script	53
	D Trajectory Calculation Script	58

NOMENCLATURE

A	<i>reference area</i>	m^2
B	<i>Mars atmosphere scale height</i>	$(11100\text{ m})^{-1}$
C_A	<i>axial force coefficient</i>	
C_P	<i>pressure coefficient</i>	
k_{Mars}	<i>Mars atmosphere thermal conductivity</i>	$1.9027E-4\text{ W/m-k}$
g	<i>gravitational constant</i>	9.81 m/s^2
H	<i>atmospheric interface altitude</i>	m
m	<i>mass</i>	kg
P	<i>pressure</i>	Pa
Pr	<i>Prandtl number</i>	
Q	<i>dynamic pressure</i>	Pa
q	<i>heat flux</i>	$W/m^2, W/cm^2$
R	<i>radius</i>	M
Re	<i>Reynolds number</i>	
T	<i>temperature</i>	k
V	<i>velocity</i>	m/s
Θ	<i>body angle</i>	<i>degrees</i>
HL	<i>heat load</i>	$J/m^2, J/cm^2$
β	<i>ballistic coefficient</i>	
γ	<i>flight path angle</i>	<i>degrees</i>
ρ	<i>density</i>	kg/m^3
$()_{ent}$	<i>atmospheric interface value</i>	
$()_f$	<i>forward reaction parameter</i>	
$()_{LE}$	<i>leading edge parameter</i>	
$()_0$	<i>altitude=0 reference value</i>	
$()_r$	<i>reverse reaction parameter</i>	
$()_S$	<i>stagnation point value</i>	
$()_{TE}$	<i>trailing edge parameter</i>	
$()_{\infty}$	<i>free stream parameter</i>	

CHAPTER 1

INTRODUCTION

1.1 Background

There is a great scientific interest in exploring Mars for geological data to determine its current and past characteristics. The polar regions are of particular interest because they currently contain water-ice on their surface, which raises the possibility of conditions on Mars surface that support liquid water. Missions involving sending experiments to Mars are both costly and high risk, since only 7 of 14 payloads sent to conduct experiments on the surface functioned after landing successfully [1].

The SCRAMP probe geometry presents a unique opportunity for future experiments. Its geometry provides an atmospheric entry vehicle with an aerodynamic center aft of the center of gravity, it is passively stable with a greater margin of static stability than a conventional sphere-cone entry vehicle geometry [2]. By eliminating active entry control systems such as attitude control thrusters, probability of mission failure is decreased. The probe can be implemented initially as a Space Station sample return vehicle with potential for scalability as a planetary probe. Testing has been performed with this geometry in suborbital reentry experiments, but comprehensive aerodynamic simulations are required to validate the SCRAMP as a solution for Mars atmospheric entry [3].



Figure 1.1 - Slotted Compression Ramp Probe.

A freestream flow Mach number of greater than 5 defines a hypersonic flow, which is significant due to phenomena in the shock region and boundary layer of an aerodynamic body. These high velocities experienced by vehicles entering an atmosphere create a strong upstream shockwave and alters the state of the fluid in its wake. The internal energy of the fluid in the free stream is overshadowed by the great kinetic energy of the free stream flow. Density of the flow around the body increases with the Mach number in the hypersonic regime, which forces the shock layer closer to the body [3].

The high density ratio across the shock wave in a hypersonic flow allows the mass of the fluid to be compressed into a smaller area, thus the thin shock wave [4]. This characteristic can create physical challenges when the shock layer begins interacting with the boundary layer.

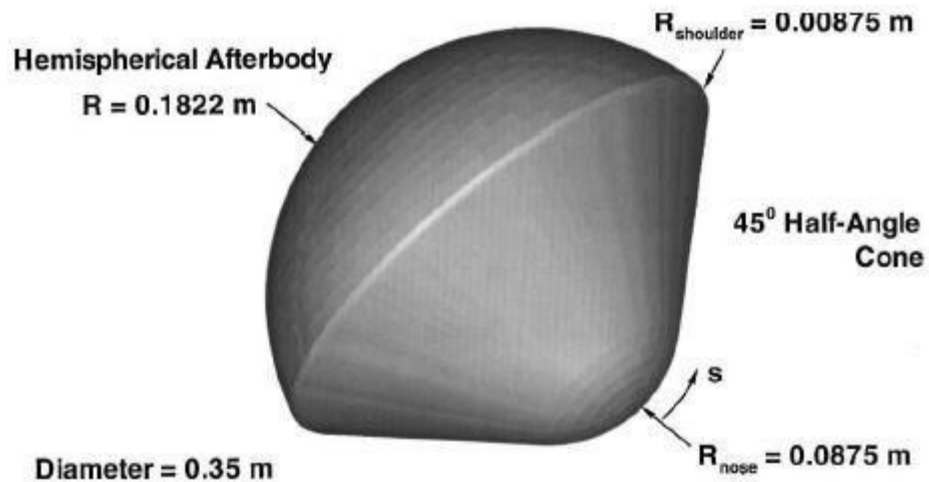


Figure 1.2 – Conventional sphere-cone geometry of DS-2 Mars probe [5].

1.2 Previous Work

The NASA Deep Space 2 mission included two small probes that landed on the Martian South Pole with the goal of demonstrating viability and collecting data on the properties of the

atmosphere and surface. Both the probes and the accompanying lander failed to transmit data after landing. The mission was developed and executed with limited time and funding, leading to engineering decisions to bypass testing and make educated assumptions on propulsion and control systems. This lack of testing resulted in an unknown cause of failure. Although entry data was not returned, this experiment provided a great deal of test data and theoretical analysis on Mars entry for small probes [5].

Similarly, the European Space Agency's Beagle 2 Mars lander mission failed to transmit data following entry and landing on Mars. In 2015, the NASA Mars Reconnaissance Orbiter captured and transmitted images of Beagle 2 on the planet surface. These images provided evidence that the lack of transmission was most likely due to failure of solar panel deployment, blocking the antenna. Confirmation of mission success up to landing shows that the aerodynamic entry modeling was sufficient [6].

The Stardust mission involved a probe spacecraft collecting dust samples from the trail of a comet as well as cosmic dust from within the solar system. The samples were collected in space and returned in a small reentry capsule for analysis. The probe entered at 12.9 km/s and encountered peak deceleration of 34 g, the fastest Earth entry of any scientific mission [7].

The Genesis mission profile, similar to Stardust, sent a probe to deep space for autonomous collection of solar wind particles and return to Earth for analysis. The probe reentered successfully but an error in integration prevented its parachute from deploying, causing damage and contaminating samples [8].

The SCRAMP body concept is a new approach to small probe atmospheric entry. By using passive stabilization methods, utilizing the shock-shock interactions and including multiple probes, probability of success can be increased.

To provide a solution for a given payload, the problem must be defined by the mission profile. This boils down to a given combination of drag, heating and stability requirements for the entry vehicle. The closest successful comparison missions to the potential ATROMOS payload by mass are the DS-2 probes. The Microprobe utilized a blunted cone heatshield fore body and hemispherical aft section to meet mission requirements. In part, the availability of previous flight data on the sphere-cone body from successful Venus and Jupiter probes was a major factor due to limited financial resources for research and testing. The entry vehicle design is flight proven to be dynamically stable if the center of gravity is set toward the cone fore body. Although the body is dynamically unstable when leading with the hemispherical side, the chance of the spacecraft reaching the unstable attitude can be minimized with spin stabilization. The hemispherical back shell also decreases dynamic instability in the transonic regime. The blunt cone fore body is selected for its drag and heating characteristics; the nose radius on the cone is a tradeoff between stability and heating characteristics. By increasing the nose radius, heating at the stagnation point is decreased but stability is lowered. The allowable heating is determined by material properties and volumetric constraints, and finally the entry vehicle can be sized for the desired ballistic coefficient [5].

By choosing a flight proven design, much of the previous research can be applied to the vehicle. We know that at hypersonic conditions above Mach 10, the bow shock has enough energy to disassociate CO₂ molecules. At the microprobe scale, gasses do not equilibrate across the thin shock layer. There is also existing wind tunnel data on sphere-cone probe geometries to predict supersonic aerodynamics, although there is less available in the transonic regime due to difficulties in testing and simulation.

The Mars Pathfinder entry vehicle also provided entry, descent and landing data of interest to the Mars entry vehicles [10]. A study of wake flow about the Mars Pathfinder entry vehicle determined that accounting for ablation reduced fore body heating by 40-50%, whereas ablation effects on the aft body were nearly identical in ablating non ablating models [11]. A study in uncertainty analysis shows that in chemically reacting hypersonic flow simulations, surface heat flux is the greatest uncertainty. The biggest factor in heat flux uncertainty is variation in gas density, which greatly varies thermal properties at the entry vehicle shoulder and stagnation point [12].

Although NASA typically follows a “test as you fly” methodology for developing flight hardware, this sometimes isn’t the case for reentry vehicles. Full scale flight condition thermal protection system testing is rarely performed due to cost, scheduling and limited facility resources. NASA Ames Research Center has developed a small probe platform named SPRITE (Small Probe Re-entry Investigation of TPS Engineering) for which there is published test data [13]. This serves as a baseline and comparison for a potential SCRAMP probe.

A series of small models were tested in an arc-jet. The objective of the study was to determine feasibility of full scale arc jet testing, perform in situ measurements and use software such as DPLR, FIAT and MARC to predict aerothermal flow properties and ablation effects of the vehicle. There were a few non ideal design compromises in the study. The first was modification of the vehicle geometry in removing the hemispherical back shell from the body for the model to mate with the arc-jet sting arm. This compromise was acceptable because the hypersonic nature of the testing means that results are mostly dictated by the fore body geometry. The design was also compromised by constructing the ablative heat shield out of two machined blank blocks of PICA material available at no cost instead of a single continuous shell.

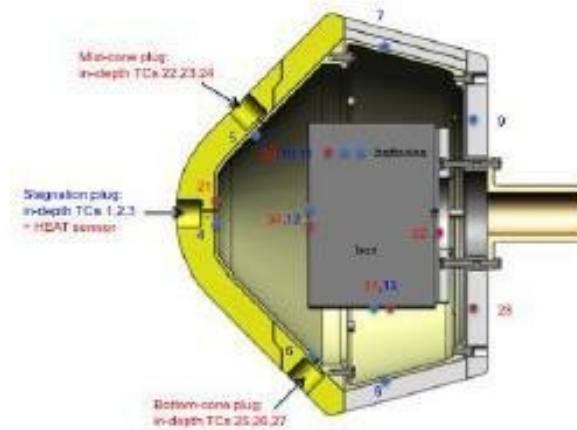


Figure 1.3 – Modified SPRITE geometry for arc-jet testing [13].

The results showed excellent agreement between simulated and actual flow separation on the body, which translates to accurate prediction of aerodynamic forces. The discrepancy in heat flux between test results and simulations can be attributed to two known sources of error; the non-uniformity of bulk enthalpy in the flow from the arc-jet, and the software requirement of uniform inflow initial conditions. The non-uniform bulk enthalpy in the flow from the arc-jet has yet to be characterized and the software is not yet capable of non-uniform inflow conditions [14].

Aerothermal loading in hypersonic shock interactions generated by the SCRAMP geometry have been studied previously due to significance in hypersonic aircraft aerodynamics and scramjet engine design. These interactions have been classified by quantitative flow characteristics into six patterns. The patterns relevant to the SCRAMP simulations in ballistic flow are Type III (Shear Layer Attachment) and Type IV (Supersonic Jet Impingement) [15].

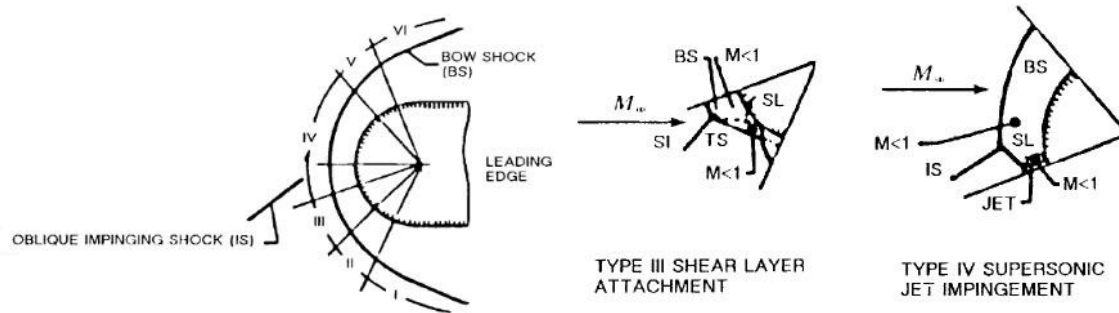


Figure 1.4 – Shock Impingement Diagram [15].

Previous studies suggest that generally peak heat transfer and pressure increases with Mach number and transition of the shear layer to turbulence. While Type III flow is relatively predictable with conventional methods, turbulent flow in Type IV interactions creates large variations in heat transfer, resulting in an overall increase of peak heating. Conversely, a body swept 15 to 30 degrees experiences a reduction in overall centerline heating of 20 to 30 percent. This would be applicable in the SCRAMP shock-shock interaction by reducing the flare angle, effectively sweeping the body [15].

1.3 Objective

The objective of this project is to parameterize the SCRAMP entry vehicle geometry, perform parametric simulations of SCRAMP probe designs to characterize the aerodynamic and thermal load properties in Mars entry conditions and determine a suitable trajectory.

CHAPTER 2

SIMULATION SETUP

2.1 Geometry Parameterization

The first step in the approach is to parameterize the geometry of the SCRAMP body and determine an optimal aerodynamic configuration for entry by performing idealized simulations. Simulations in free molecular flow, supersonic and hypersonic flow with disassociating gasses are required to determine optimized geometry. Once optimal geometry is selected, increase detail of geometry and determine aerodynamic characteristics for nominal flight path.

The geometry parameterization completed in MATLAB script to create a data set of two-dimensional coordinates of the desired body profile in axisymmetric form. This provides a complete geometry for the model with any desired parameter of variables, including the following: nose radius, body length, body ramp angle, fin thickness, fin radius (total width), fin shoulder radius, fin start location, gap distance, aft section type (spherical, conical or truncated), and number of data points along each section of the body. Each parameter defining the geometry is defined in Figure 2.1. The two-dimensional coordinate output text file is imported to CAD or grid generating software to create a 3D grid model of the full body by rotating about the x-axis.

Table 2.1 – List of Geometric Parameters.

Description	Variable	Nominal Value
Nose radius	R_nose	92
Body Length	l_body	623
Body Ramp Angle	t_body	0
Fin Angle	t_fin	45

Radius at Fin (Total Body Radius)	r_fin	507
Shoulder Radius	r_shld	0
Gap Distance	d_gap	50
Fin Radius; Fin Half Thickness	d_fin	10
Fin Leading Edge Location	flex	371
Aft Geometry (round, conical, straight)	aft	3 (straight)

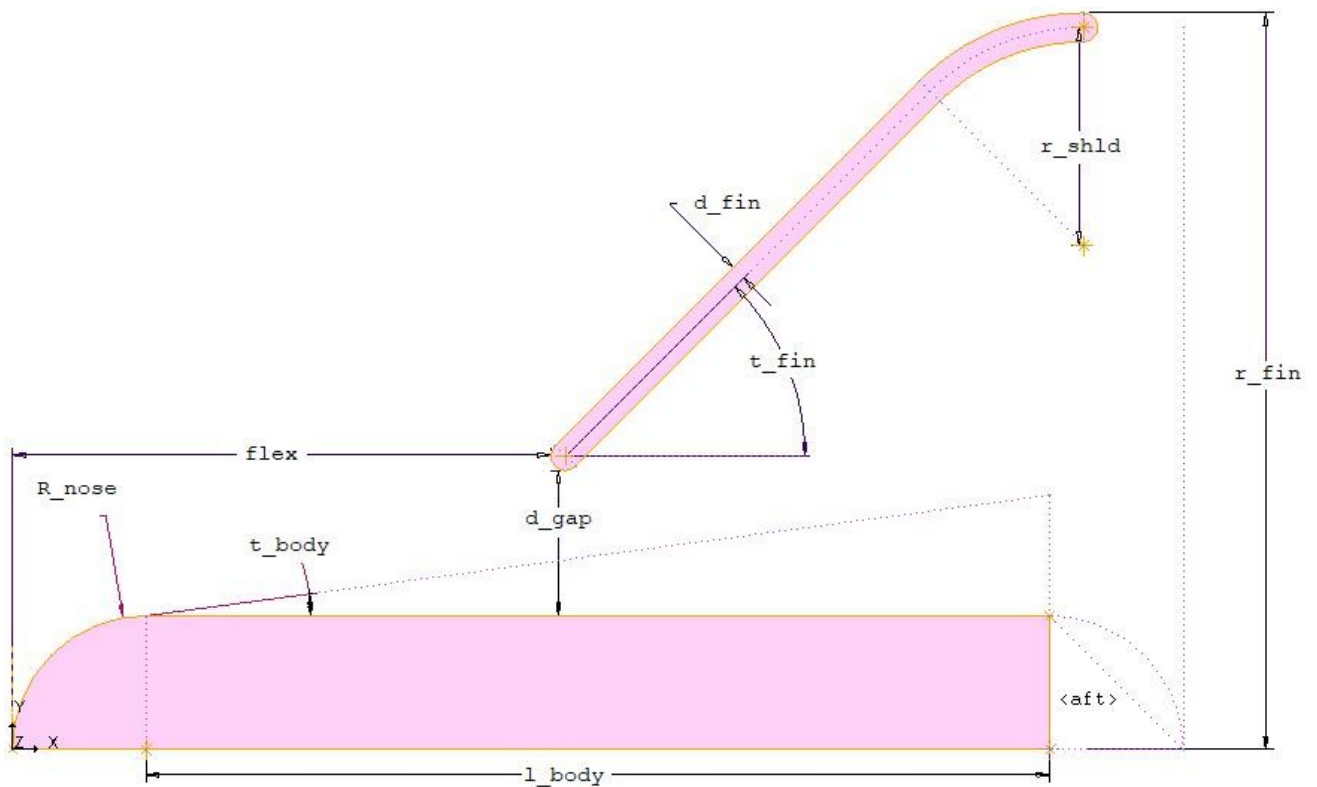


Figure 2.1 –Parameterized Axisymmetric SCRAM Geometry.

The three geometries tested include a “nominal” case with a straight 45-degree flare, an increased gap size of 50 mm, and a variation with a 100 mm radius on the fin. All use a reference length of 0.807 meters as shown in Figures 2.2 through 2.4.

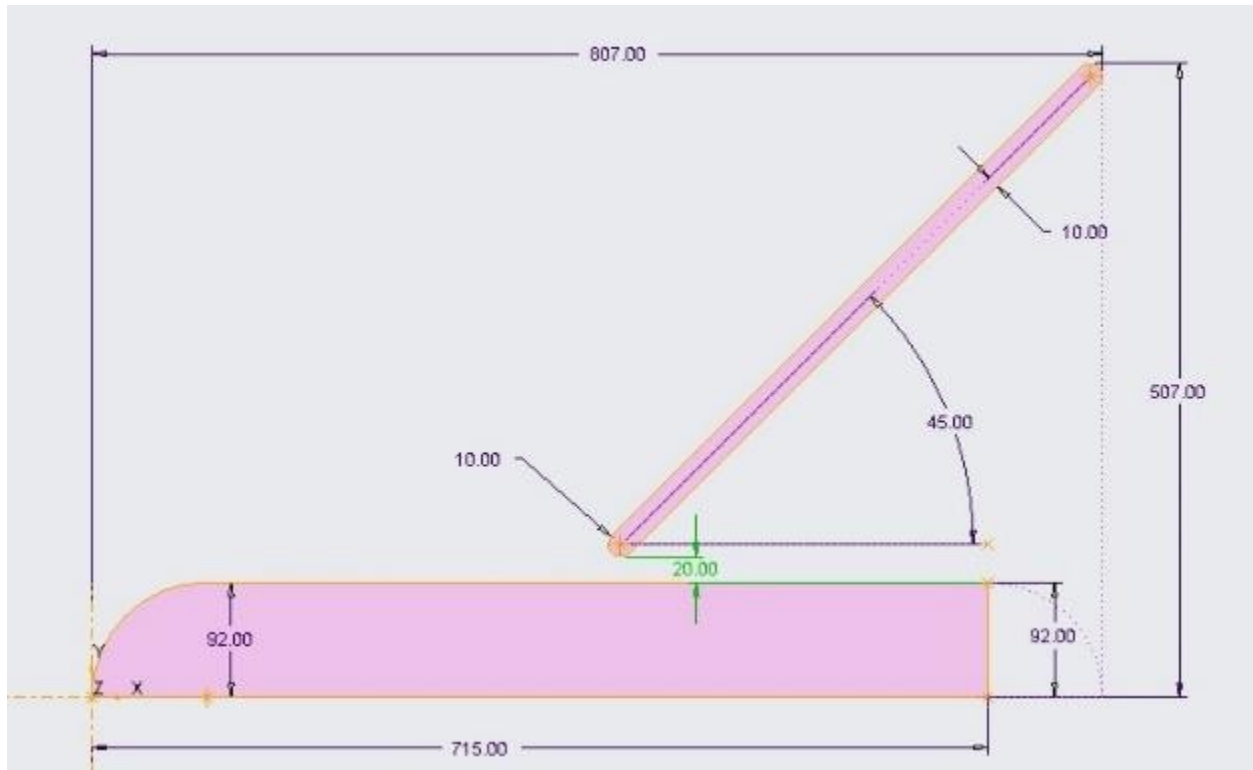


Figure 2.2 – "Nominal" Geometry

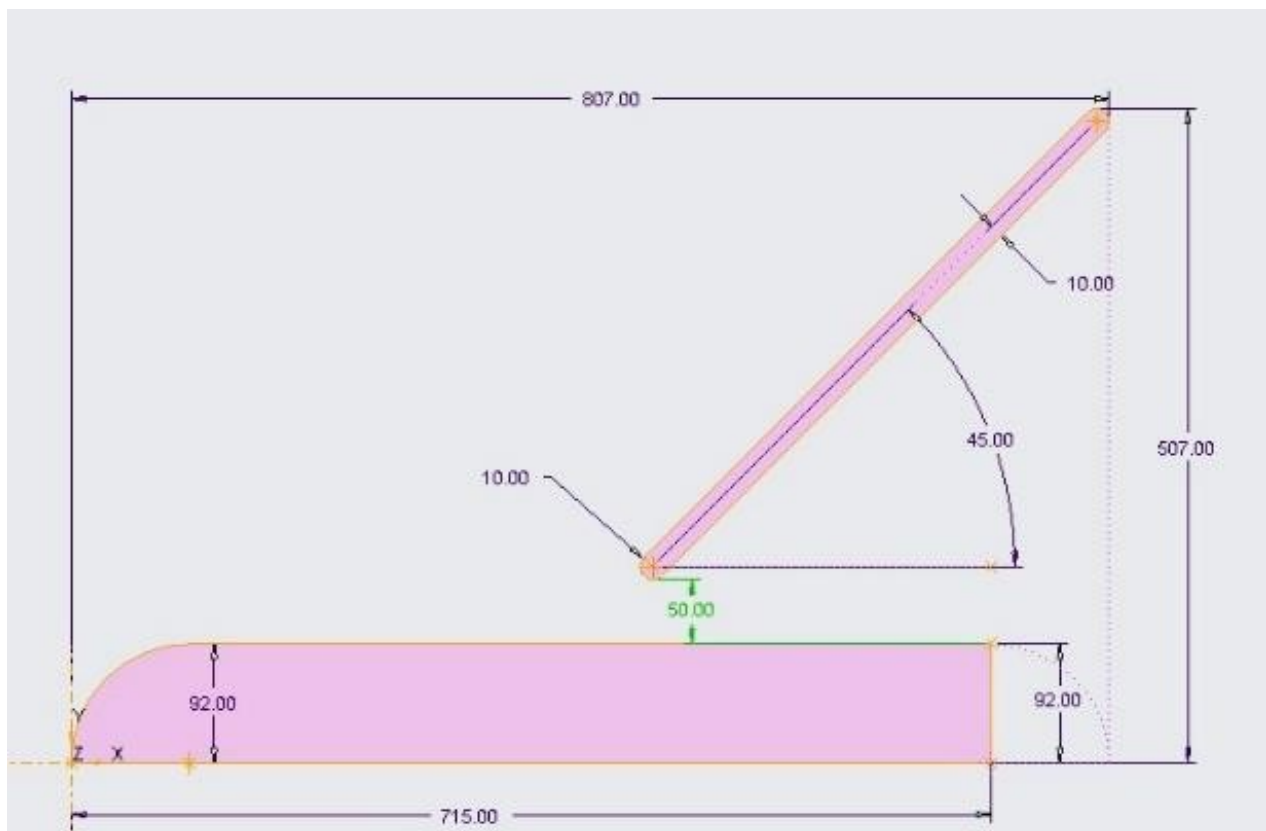


Figure 2.3 – "Gap" Geometry

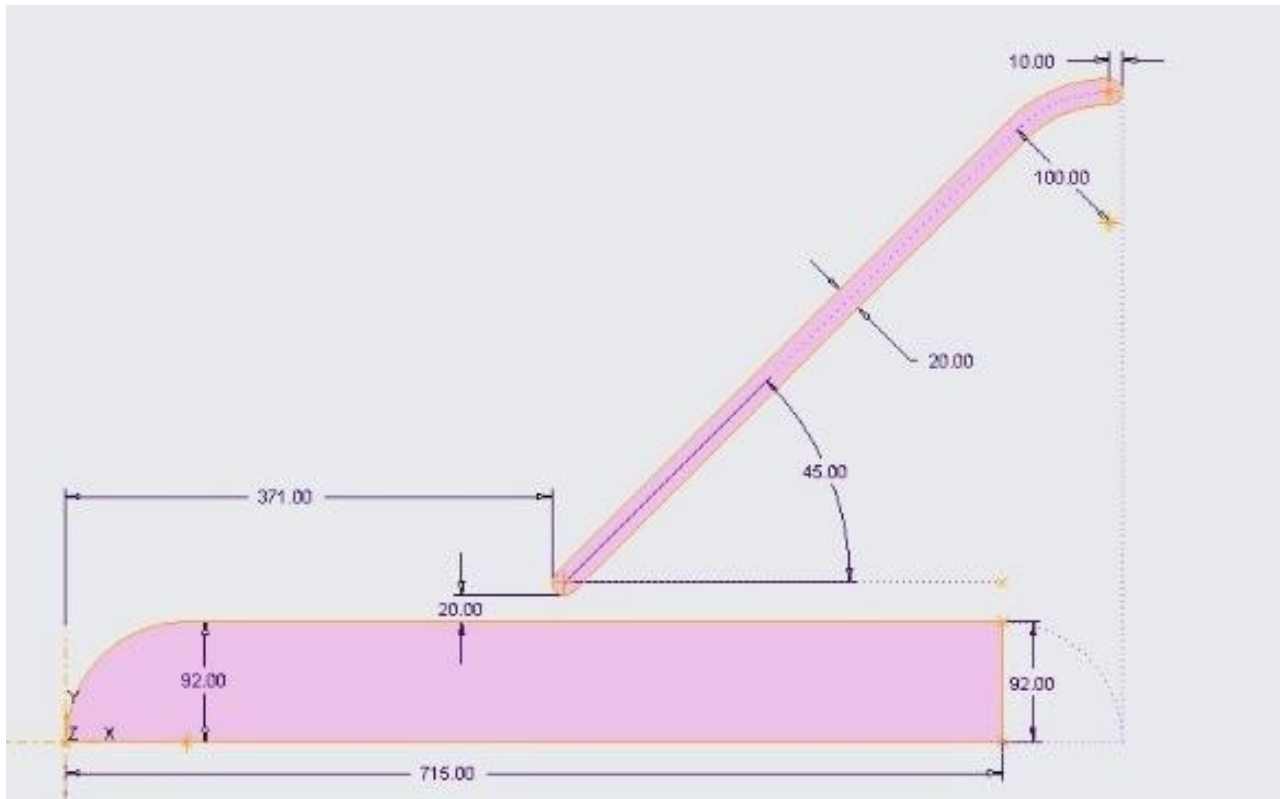


Figure 2.4 – “Shoulder” Geometry

2.2 Test Case Selection

The flight path of the probe is dependent on the aerodynamic characteristics yet to be determined, simulation test cases are selected along the flight path of the DS-2 Probes, the closest available comparison by size, weight and assumed entry velocity.

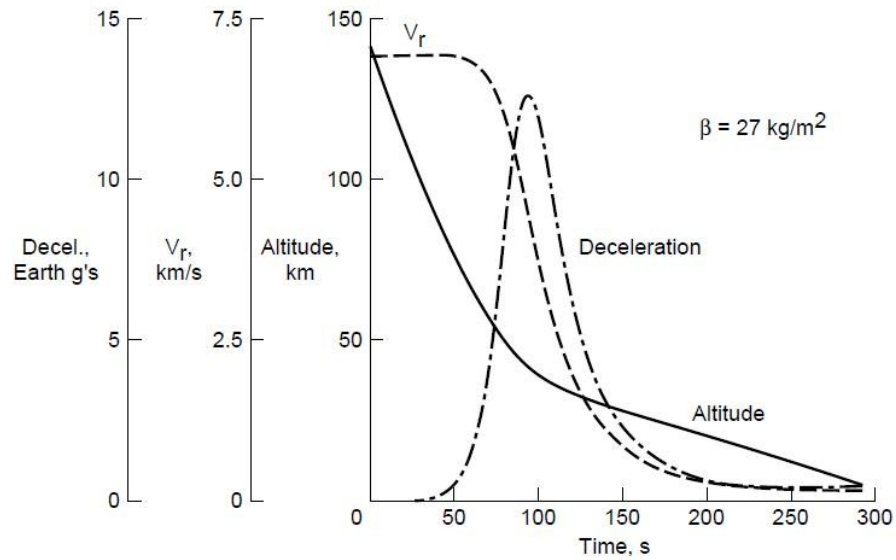


Figure 2.2 – DS-2 Entry Profile [15].

The cases selected best capture the heating and deceleration profile with a limited number of test points available. Free stream conditions of Mars atmosphere are mean values from experiment data, which fluctuate due to variable atmospheric properties with respect to seasons and local weather.

Table 2.2 – Selected Mars Entry Profile Case Conditions [16].

Case	Alt. (km)	V_∞ (m/s)	T_∞ (K)	P_∞ (Pa)	ρ (kg/m ³)	DP_∞ (Pa)
A	80	7000	129.5	0.046	1.86 E-6	45.57
B	65	6800	143.0	0.361	1.33 E-5	307.5
C	50	6000	157.0	2.25	8.26 E-5	1487
D	35	3000	171.0	13.8	4.25 E-4	1912
E	20	400	185.0	70.1	2.20 E-3	176.0

Five cases were selected initially, but the highest altitude case would not provide satisfactory simulation results due to low temperature and density properties of the free stream flow.

2.3 Hypersonic Flowfield Modeling

The simulation of flow around the body of interest is performed by leveraging the Navier-Stokes Equations. By defining a control volume around the body, the basic laws of conservation of mass and energy are applied to the system. The system control volume is divided into finite volumes small enough to accurately predict flow properties and aerodynamic forces on the body [17].

$$\rho \frac{dV}{dt} + \rho V \frac{dV}{dt} + \rho V \frac{dV}{dt} = 0 \tag{2.1}$$

$$\rho \frac{dV}{dt} + \rho V \frac{dV}{dt} + \rho V \frac{dV}{dt} = - \rho \frac{dV}{dt} + \frac{1}{\rho} [\rho \frac{dV}{dt} + \rho \frac{dV}{dt} + \rho \frac{dV}{dt}] \tag{2.2}$$

$$\rho \frac{dV}{dt} + \rho V \frac{dV}{dt} + \rho V \frac{dV}{dt} + \rho V \frac{dV}{dt} = - \rho \frac{dV}{dt} + \frac{1}{\rho} [\rho \frac{dV}{dt} + \rho \frac{dV}{dt} + \rho \frac{dV}{dt}] \tag{2.3}$$

$$\rho \frac{dV}{dt} + \rho V \frac{dV}{dt} + \rho V \frac{dV}{dt} + \rho V \frac{dV}{dt} = - \rho \frac{dV}{dt} + \frac{1}{\rho} [\rho \frac{dV}{dt} + \rho \frac{dV}{dt} + \rho \frac{dV}{dt}] \tag{2.4}$$

$$\rho \frac{dV}{dt} + \rho V \frac{dV}{dt} + \rho V \frac{dV}{dt} + \rho V \frac{dV}{dt} =$$

$$\rho \frac{dV}{dt} + \rho V \frac{dV}{dt} + \rho V \frac{dV}{dt} + \frac{1}{\rho} [\rho \frac{dV}{dt} + \rho \frac{dV}{dt} + \rho \frac{dV}{dt}] = \rho \frac{dV}{dt} \tag{2.5}$$

$$\rho \frac{dV}{dt} + \rho V \frac{dV}{dt} + \rho V \frac{dV}{dt} + \frac{1}{\rho} [\rho \frac{dV}{dt} + \rho \frac{dV}{dt} + \rho \frac{dV}{dt}]$$

To accurately simulate flow in each finite control volume, a cell must have normal faces to preserve the validity of the Navier-Stokes equations. This requirement becomes increasingly difficult to meet with spherical geometries and multiple features on a body.

The fin section of the geometry utilizes an overset structured grid to maintain quality around the shape that is otherwise prohibitively difficult to accurately model in a structured domain [18].

2.4 Reacting Flow

Hypersonic flow encountered in planetary entry will dissociate and partially ionize gases. To accurately model flow around the SCRAM, the Park-94 model is utilized [15]. The Park model utilizes previous experimental data to predict gas reactions in hypersonic flow. This model has been utilized in previous axisymmetric Mars entry simulations and verified with flight data [19].

$$K_f(T) = A_f T^{b_f} \exp(-E_f/T) \text{ [m}^3 / (\text{kmol} \cdot \text{s})] \quad (2.6)$$

$$K_r(T) = A_r T^{b_r} \exp(-E_r/T) \text{ [m}^6 / (\text{kmol}^2 \cdot \text{s})] \quad (2.7)$$

Table 2.2 – Reactions and Reaction Rate Constants [14].

#	Reaction	A _f	B _f	E _f	A _r	B _r	E _r
1	CO ₂ +O ₂ ↔ CO+O+O	6.90E18	-1.5	63275	1.14E11	-0.75	535
2	CO ₂ +O ↔ CO+O+O	1.38E19	-1.5	63275	2.28E11	-0.75	535
3	CO ₂ +C ↔ CO+O+C	1.38E19	-1.5	63275	2.28E11	-0.75	535
4	CO ₂ +C ↔ CO+CO+O	6.90E18	-1.5	63275	1.14E11	-0.75	535
5	CO ₂ +CO ₂ ↔ CO+O+CO ₂	6.90E18	-1.5	63275	1.14E11	-0.75	535
6	CO+O ₂ ↔ C+O+O ₂	2.30E17	-1.0	12900	5.13E12	-1.00	0
7	CO+O ↔ C+O+O	3.40E17	-1.0	12900	7.59E12	-1.00	0
8	CO+C ↔ C+O+C	3.40E17	-1.0	12900	7.59E12	-1.00	0
9	CO+CO ↔ C+O+CO ₂	2.30E17	-1.0	12900	5.13E12	-1.00	0
10	CO+CO ₂ ↔ C+O+CO ₂	2.30E17	-1.0	12900	5.13E12	-1.00	0

11	$O_2+C \leftrightarrow O+O+C$	1.00E19	-1.5	59500	1.00E13	-1.00	0
12	$O_2+CO \leftrightarrow O+O+CO$	2.00E18	-1.5	59500	2.00E12	-1.00	0
13	$O_2+CO_2 \leftrightarrow O+O+CO_2$	2.00E18	-1.5	59500	2.00E12	-1.00	0
14	$CO+CO \leftrightarrow CO_2+C$	2.33E6	0.5	65710	4.60E9	-0.25	0
15	$CO+O \leftrightarrow O_2+C$	3.90E10	-0.18	69200	1.34E11	-0.43	0
16	$CO_2+O \leftrightarrow O_2+CO$	2.10E10	0.0	27800	4.11E7	0.50	0
17	$O_2+O_2 \leftrightarrow O+O+O_2$	2.00E18	-1.5	59500	2.00E12	-1.00	23800
18	$O_2+O \leftrightarrow O+O+O$	1.00E19	-1.5	59500	1.00E13	-1.00	0

CHAPTER 3

AERODYNAMIC RESULTS

3.1 Newtonian Approximation

Due to the high entry velocity and low angle of attack of the trajectory, a modified Newtonian approximation of the drag provides an appropriate estimate of the drag forces at hypersonic velocities [4].

$$C_P = C_{P,Max} \sin^2 \Theta \quad (3.1)$$

$$C_{P,Max} = \frac{0.2 \gamma \infty}{\dots} \quad (3.2)$$

$$\frac{1}{\dots} \quad (3.3)$$

These values are calculated in the geometry parameterization script due to the nature of this method relying solely on the geometry of the body in axisymmetric flow. The results of test cases are listed with simulation data in Table 3.1.

3.2 Simulation Results

Computational results of the axisymmetric simulations provide three dimensional axial force coefficients shown in Table 3.1 with the Newtonian approximations. The passively stable nature of the entry vehicle geometry assumes little or no angle of attack. Complete temperature, pressure and skin friction coefficient data for each simulation is compiled in Appendix A. This data is also presented in Appendix B comparing each design at test points.

Table 3.1 – Axial force coefficient results.

	Reference Area (m ²)	C _a Newtonian	C _a B	C _a C	C _a D	C _a E
Nominal	0.807	0.986	.749	0.884	0.957	0.908
Gap	0.906	0.930	1.037	0.919	1.070	1.188
Shoulder	0.807	0.950	.704	.899	0.902	0.873

3.3 Analysis

Cases in which the shock layer is deflected entirely by the flare section exhibit properties similar to a conventional reentry geometry as shown in Figure 3.1. This is an example of Type III shock impingement, shear layer attachment in which a single shock layer is shared.

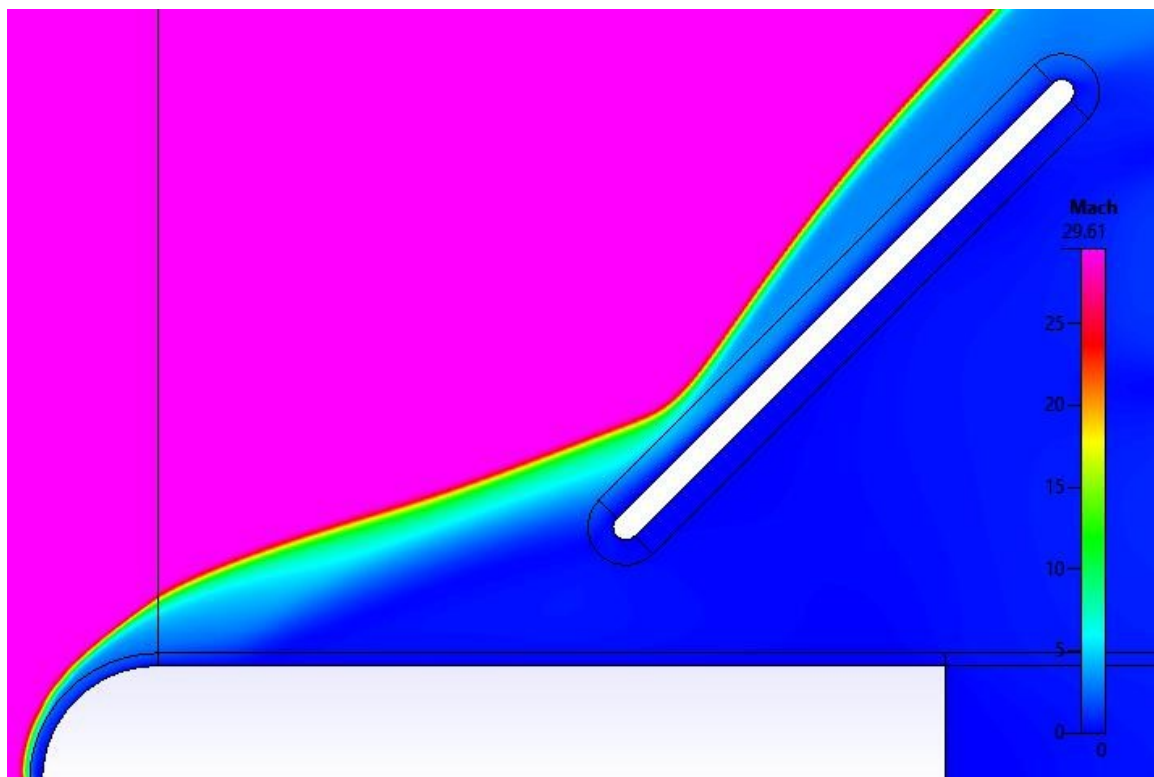


Figure 3.1 – Gap case C Mach contour.

The pressure diagram in Figure 3.2 displays the pressure and temperature fields of the same simulation. The flare encounters a pressure spike on the same order as the nose stagnation point and a temperature profile similar to the leading edge.

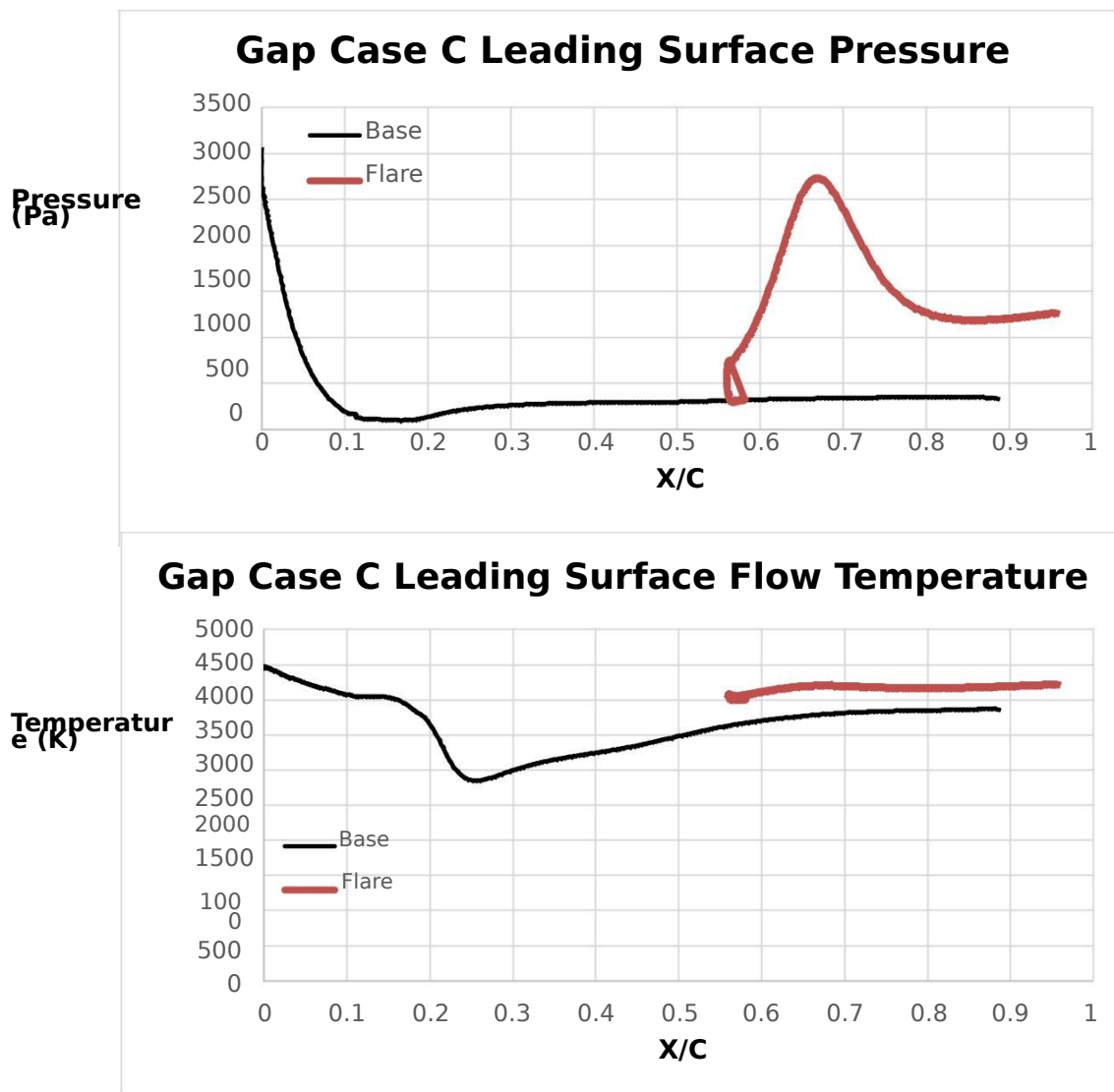


Figure 3.2 – Gap Case C contour plots.

Simulations present a higher drag coefficient in conditions where the shock layer partially flows through the gap section, shown in Figure 3.3. This property is a result of greater viscous interactions behind the shock. Temperature profiles of the flow near the probe body also appear

much higher in these cases. These characteristics may also vary with different geometry at the aft section of the body in future work. This agrees with previous work on shock impingement, cases where a Type III Shear Layer Attachment occurs resulting in lower peak heating and pressure than the Type IV interactions [15]. The “Gap” geometry experiences the greatest temperatures across the flare surface in test cases B, C and D where the greatest heat flux is expected. This is a result of the increased gap size allowing the high temperature and density fluid behind the shock to attach to the flare shock layer.

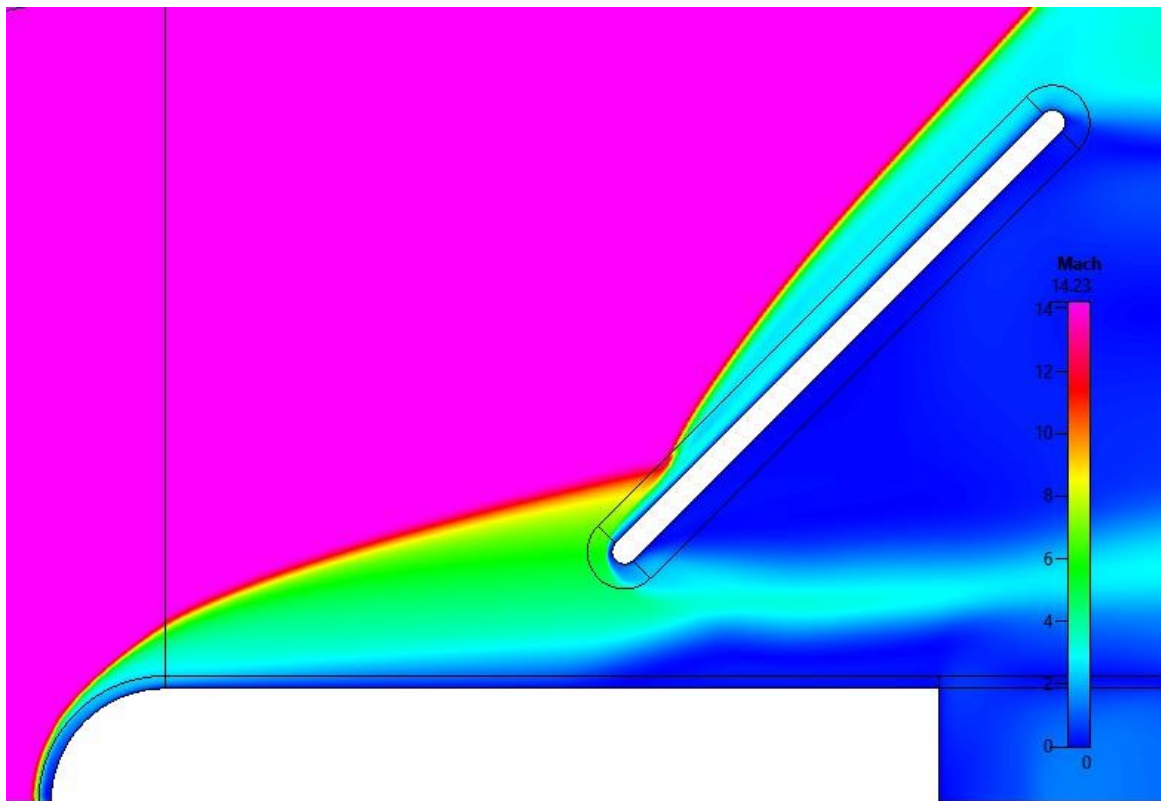


Figure 3.3 – Gap case D Mach contour.

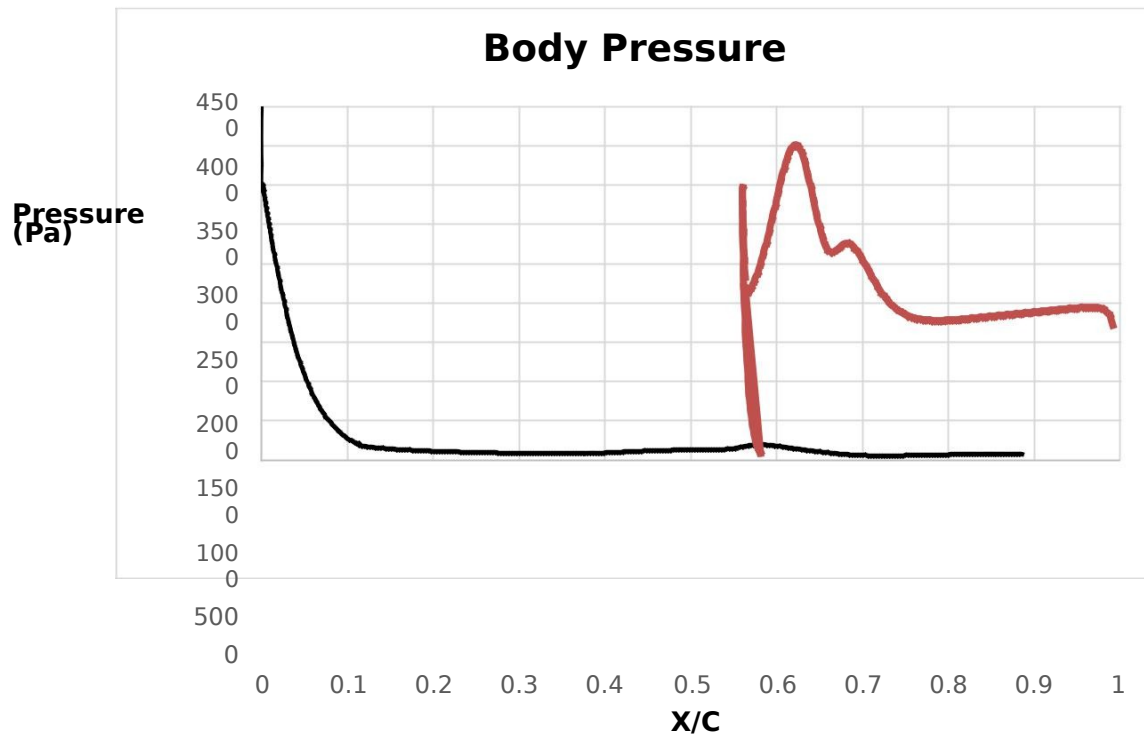


Figure 3.3 – Case D leading surface pressure plot.

The ideal geometry in terms of aerodynamic and thermal characteristics will vary based on the planned trajectory. A higher drag design may be desirable in cases which atmospheric temperatures are relatively low or the probe is implemented with a robust thermal protection system. The final systems design of the experiment payload will determine the constraining values of weight and volume allotted toward entry system structure and ablating thermal protective material. A lower drag design would be more beneficial for high velocity entries in which the total heat load becomes the constraining design variable due to limited ablation or thermal protection required by the experiment payload.

CHAPTER 4

THERMAL PROPERTIES & TRAJECTORY ANALYSIS

4.1 Stagnation Point Heating

The location of greatest interest with respect to heating and ablation is the stagnation point on the hemispherical nose. Simulation data confirms that none of the shock interactions induce a higher surface temperature than the leading edge stagnation point. Stagnation point data also provides a reference point for extrapolating full body heating estimates [5]. The Sutton-Graves heating equation provides an approximation for convective stagnation point heat flux on a hemispherical forebody entering Mars atmosphere [5].

$$q = \frac{1}{2} \rho V^3 \left(\frac{C_H}{\sqrt{r}} \right) \quad (4.1)$$

Table 4.1 – Stagnation point heat flux approximation.

Test Case	A	B	C	D	E
$q \text{ (W/cm}^2\text{)}$	29.3	71.9	123	34.9	0.188

The values obtained through Sutton-Graves calculations are proportional to comparable Mars entry missions. Although heating calculations for the spherical nose are identical since there was no variation in the fore body radius parameter, heating characteristics vary in simulations on the flare surface. One of the key results of the simulations is that the flare section of the geometry experiences temperatures on the same order of the stagnation point. In cases where the shock layer captured by the flare section, flow density is nearly equal to that of the

stagnation point as shown in Figure 4.1. The highest density in the flow appears at the shock-shock interaction at a small distance from the wall.

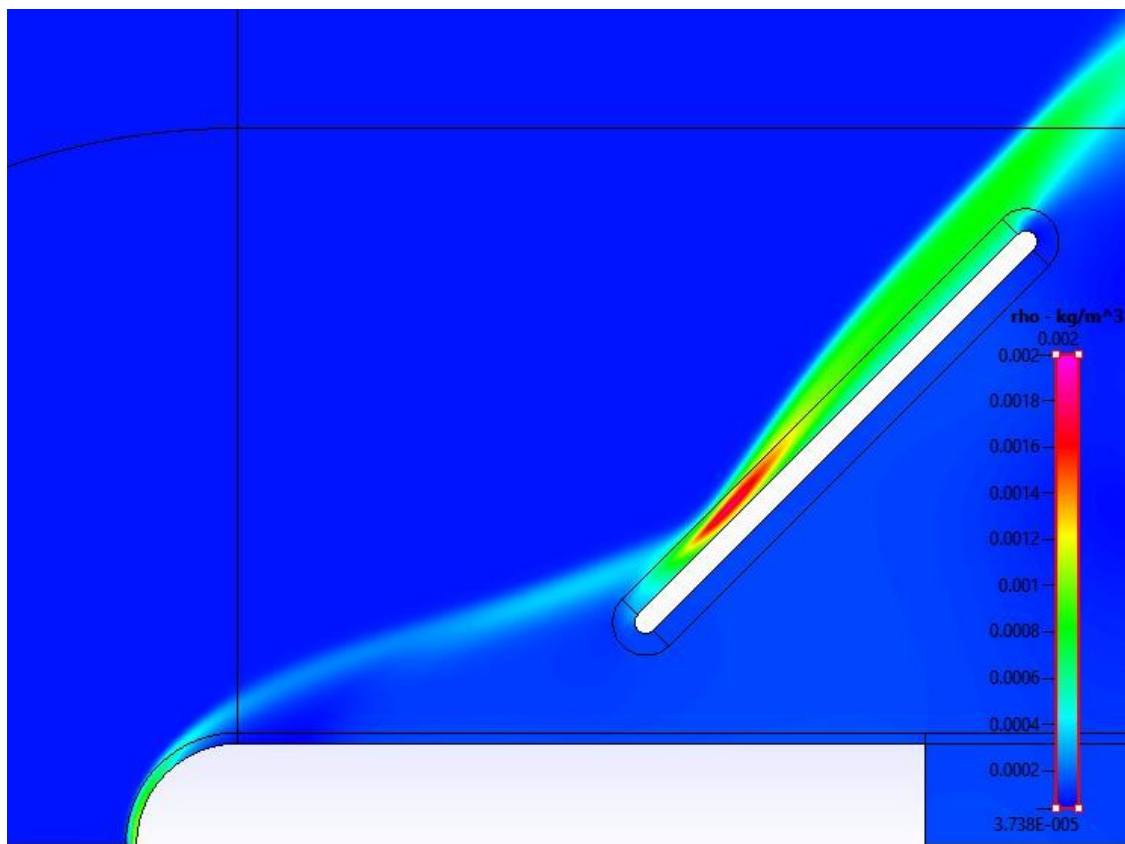


Figure 4.1 – Gap case C density contour.

These properties of the flow show that further analysis of ablation is required on the flare surface as well as the spherical nose. Analysis using ablative material in the fore body in a similar Mars entry study reduced the max heating rate by roughly 50 percent, while use of ablative material on the trailing side had a negligible effect [5].

The changes in body geometry coupled with thermodynamic and aerodynamic properties are interdependent. Changes in the thermal properties of the flow as well as physical shape of the nose and flare due to ablation will propagate into aerodynamic effects further in the trajectory.

4.2 Thermal – Trajectory Coupling

Utilizing the axial coefficient results of the “nominal” geometry, the nominal ballistic coefficient is determined to be 27.7. Utilizing the Allen-Eggers approximations with a fixed velocity-flight path following the DS-2 probe trajectory, stagnation point heat flux profile and integrated heat load are determined [21].

$$= \frac{\dots}{\dots} \quad (4.2)$$

$$V = \sqrt{\dots} \quad (4.3)$$

$$= 6.8 \times 10^{-6} \sqrt{\dots} \quad (4.4)$$

These calculations are performed in an additional MATLAB script in Appendix D to allow variable properties to control simulated trajectory. CFD simulation test cases as shown were taken at points along the flight path of the DS-2 entry, which decelerates lower in the atmosphere than SCRAMP. This explains the discrepancy in stagnation point heat flux calculated for test cases versus the scripted trajectory simulation, due to higher velocities in the lower altitude and more dense atmosphere. Using the force coefficients from the first design iteration CFD simulation, the hypersonic continuum ballistic coefficient is determined to calculate a more accurate flight path from the same entry conditions of 7000 m/s entry speed and -13.5 degree flight path angle.

The SCRAMP trajectory decelerates higher in the atmosphere than the comparable Mars entry vehicles as shown in figure 4.2. This is due to the greater surface area than the DS-2, and lower mass than the Beagle 2 lander. These properties result in peak stagnation point heating occurs in lower density flow, resulting in peak heat flux an order of magnitude lower than the

DS-2 probe. Although the calculated total heat loads are similar, the SCRAMP distributes the heat load throughout the trajectory.

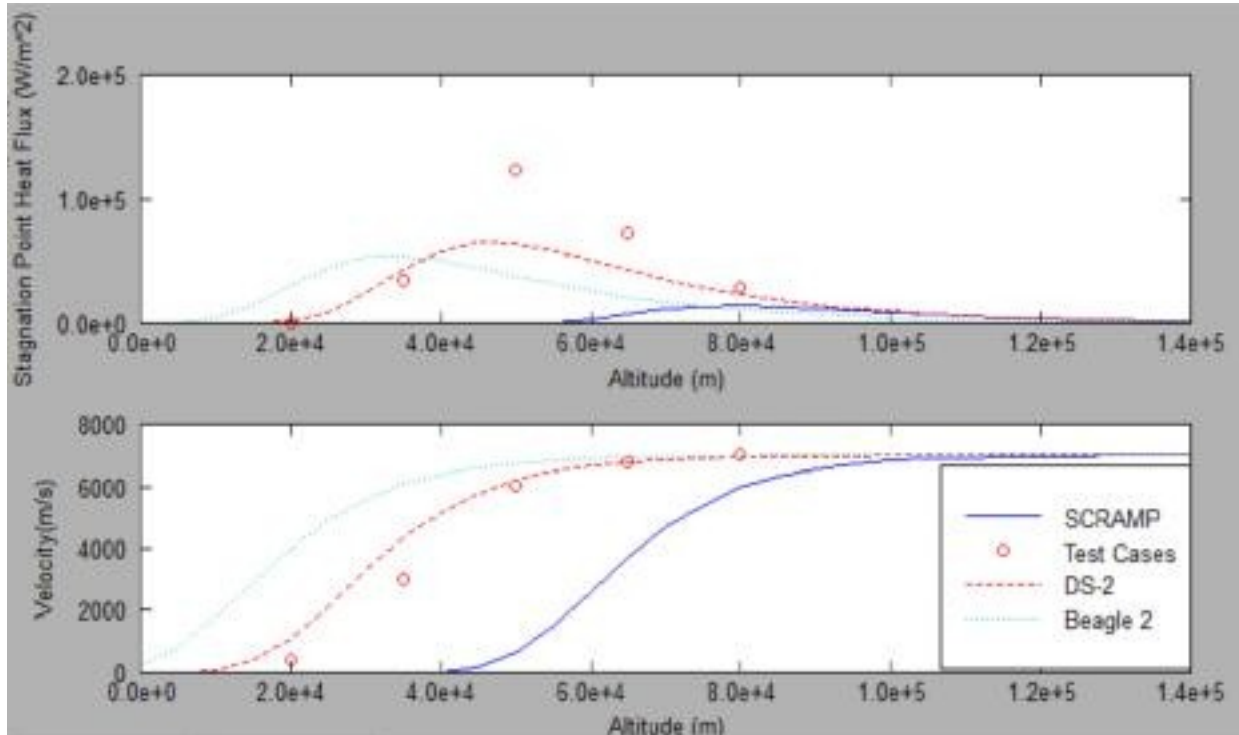


Figure 4.2 – Comparison of SCRAMP and DS-2 trajectory with fixed $V-\gamma$.

Table 4.2 - Comparison of Mars probe thermal properties.

Probe	Ballistic Coefficient (kg/m^2)	Mass (kg)	Reference Area (m^2)	Stag. Point Heat Load (J/m^2)	Peak Heat Flux (W/m^2)
DS-2 [6]	27	2.5	0.096	2.03×10^9	5.13×10^5
<i>SCRAMP</i>	27.7	20	0.807	2.00×10^9	1.44×10^4
Beagle 2 [7]	70	60	0.636	1.50×10^9	3.78×10^5

4.3 Trajectory Parametric Study

Utilizing the trajectory-heating equations, the design variables of β - γ are isolated with a fixed entry velocity of 7000 m/s to show their effects on critical trajectory results. Based on the Allen-Eggers calculations, peak deceleration varies with entry velocity and flight path angle but completely independent of the ballistic coefficient value as shown in Figure 4.5.

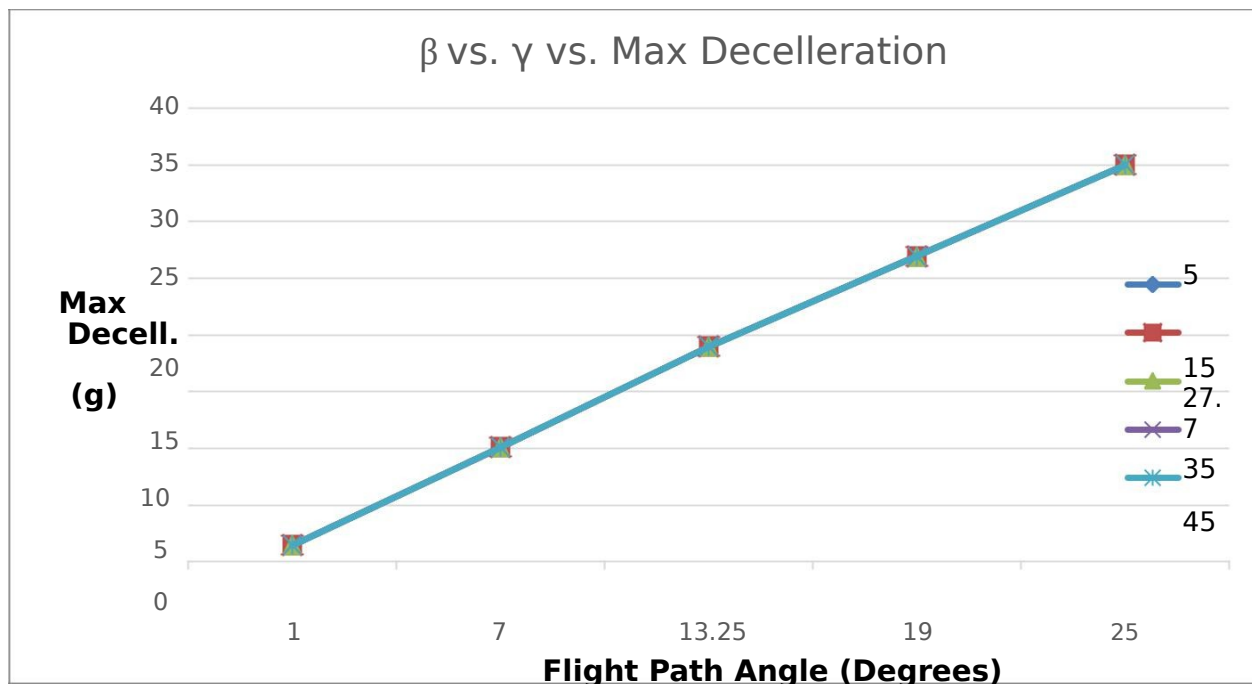


Figure 4.5 - Maximum deceleration independence of ballistic coefficient.

The key results for entry vehicle design become peak heat flux and total heat load. These properties are required to design further thermal protection system and structural details of the entry vehicle. As shown in Figures 4.3 and 4.4, as vehicle ballistic coefficient grows, thermal requirements increase. This is directly proportional to payload mass, which is critical to maximize for Mars planetary experiments.

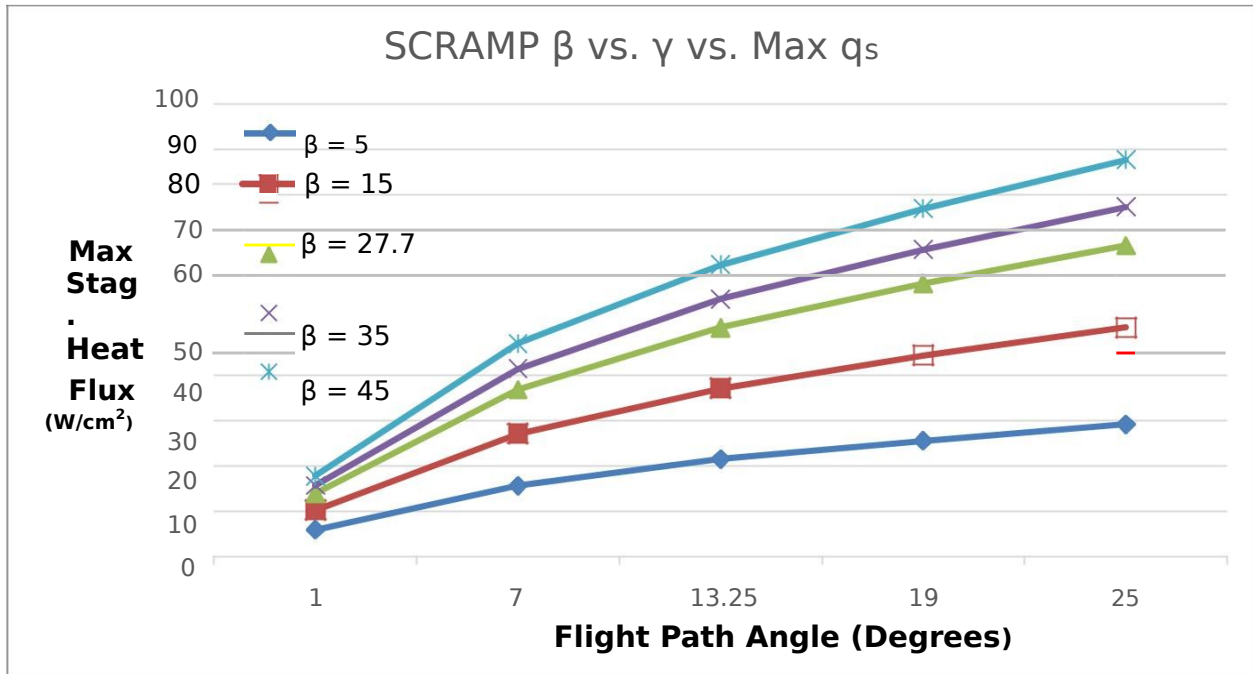


Figure 4.3 - $\beta - \gamma$ - peak heat flux relation for SCRAMP geometry.

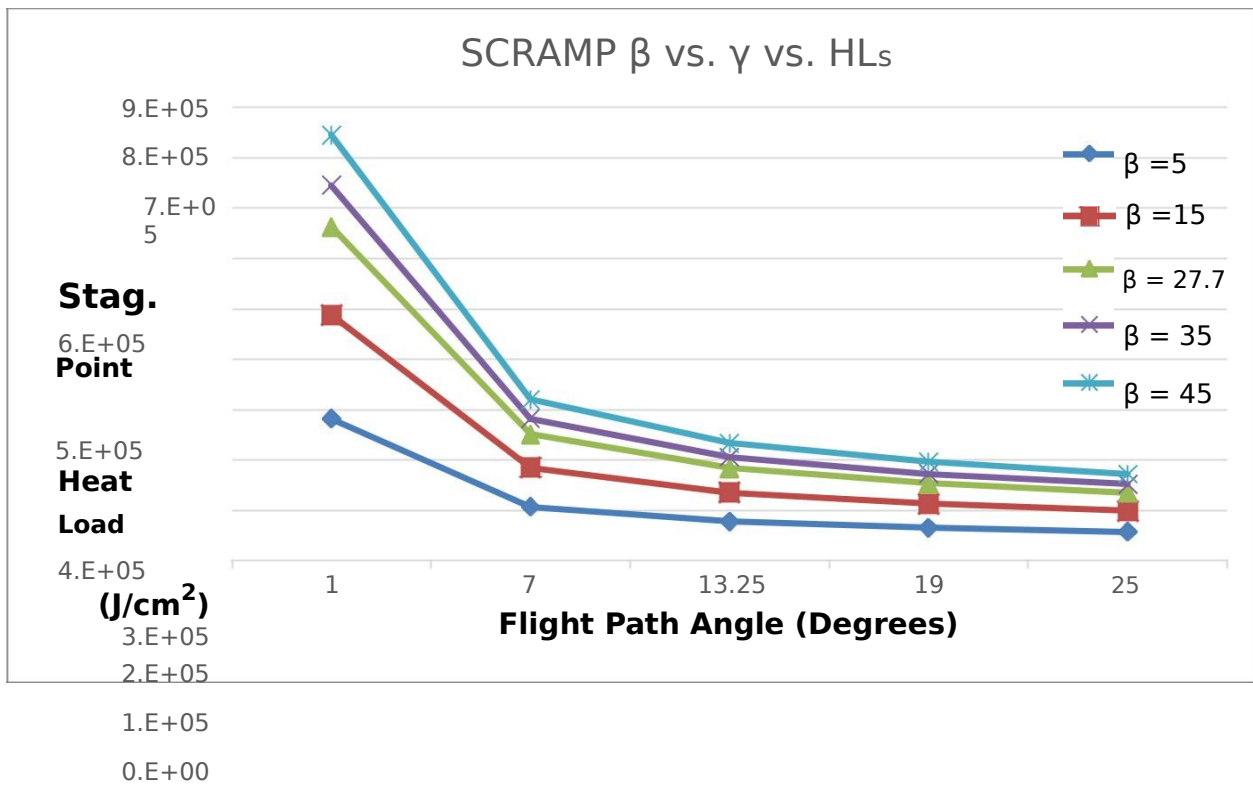


Figure 4.4 – β – γ – heat load relation for SCRAM geometry.

CHAPTER 5

CONCLUSION

This analysis has provided aerodynamic and thermal properties suitable for a first iteration of a mission design. For mission specific analysis, two or more additional design iterations would be ideal. Utilizing the trajectory calculation will provide more valuable CFD results for manipulating the entry vehicle geometry. Determining the conditions where peak heating occurs will allow for the best geometry optimization.

Aerodynamic simulations show that the SCRAMP geometry provides a ballistic coefficient similar to that of the conventional sphere-cone DS-2 probe with much more desirable aerodynamic and thermal characteristics. The wide body radius causes deceleration earlier in a given trajectory, which therefore reduces peak heating and total heat load through the trajectory. This also provides capability to deliver a greater payload to the surface of Mars for given entry conditions.

A key result of this study is that the SCRAMP design in the current configuration will utilize a gap distance under 50 mm to ensure a Type IV shock interaction between the body and flare does not occur while experiencing peak heating conditions. The optimal gap distance will be as large as possible to maximize energy dissipation behind the shock while avoiding a supersonic jet impingement inducing critically high heating on the flare surface.

Monte Carlo simulations would be required to determine mission success criteria due to uncertainties in controllability of design parameters including atmospheric interface speed and angle. There are also variable atmospheric properties including temperature, pressure, gas species and dust composition currently assumed. Use of Monte-Carlo simulations in combination with CFD simulations has been shown to provide results accurate to Mars entry

experiments [11]. These results can also be used to refine future simulations by designing grids to capture the shock layer and predict shock-shock interactions in closer detail.

REFERENCES

1. Zubrin, R., *The Case for Mars*, Simon and Schuster, 2012.
2. Murbach, M., Papadopoulos, P., White, B., & Tegnerud, E. ATROMOS: A Mars Companion Mission Enabled by Advanced EDL Concepts.
3. Zuniga, D., Murbach, M. A., Leimkuehler, T. O., Leidich, J., Chiesi, S. S., Conceptual Development of a Payload Thermal and Pressure Control System for a Small Payload Quick Return Vehicle, *40th International Conference on Environmental Systems*, Jul. 2010.
4. Papadopoulou, E., *Numerical Simulations of the Apollo 4 Re-entry Trajectory* (Doctoral dissertation, École Polytechnique Federale de Lausanne), 2014.
5. Anderson, J. D., *Hypersonic and High Temperature Gas Dynamics*, AIAA, 2010.
6. Mitcheltree, R. A., Moss, J. N., Cheatwood, F. M., Greene, F. A., Braun, R. D., Aerodynamics of the Mars Microprobe Entry Vehicles, *Journal of Spacecraft and Rockets*, Vol. 36, No. 3, 1999, pp. 392-398
7. Liever, P. A., Habchi, S. D., Burnell, S. I., Lingard, J. S., Computational Fluid Dynamics Prediction of the Beagle 2 Aerodynamic Database, *Journal of Spacecraft and Rockets*, Vol. 40, No. 5, 2003, pp. 632-638.
8. Mitcheltree, R. A., Wilmoth, R. G., Cheatwood, F. M., Brauckmann, G. J., Greene, R. A., Aerodynamics of Stardust Sample Return Capsule, *Journal of Spacecraft and Rockets*, Vol. 36, No. 3, 1999.
9. Desai, P. N., Qualls, G. D., Schoenenberger, M., Reconstruction of the Genesis Entry. *Journal of Spacecraft and Rockets*, Vol. 45, No. 1, 2008.

10. Spencer, D. A., Blanchard, R. C., Braun, R. D., Kallemeyn, P. H., Thurman, S. W., Mars Pathfinder Entry, Descent, and Landing Reconstruction. *Journal of Spacecraft and Rockets*, Vol. 36, No. 3, 1999.
11. Gnoffo, P. A., Braun, R. D., Weilmuenster, K. J., Mitcheltree, R. A., Englund, W. C., Powell, R. W., Prediction and Validation of Mars Pathfinder Hypersonic Aerodynamic Database. *Journal of Spacecraft and Rockets*, Vol. 36, No. 3, 1999.
12. Weaver, A. B., Alexeenko, A. A., Greendyke, R. B., Camberos, J. A., Flowfield Uncertainty Analysis for Hypersonic Computational Fluid Dynamics Simulations. *Journal of Thermophysics and Heat Transfer*, Vol. 25, No. 1, 2011.
13. Empey, D. M., Gorbunov, S., Skokova, K. A., Agrawal, P., Swanson, G. T., Prabhu, D. K., & Venkatapathy, E., Small Probe Reentry Investigation for TPS Engineering (SPRITE). *AIAA Paper*, 2012.
14. Prabhu, D., Flowfield Analysis of a Small Entry Probe (SPRITE) Tested in an Arc Jet. In *50th AIAA Aerospace Sciences Meeting Including the New Horizons Forum and Aerospace Exposition*, Jan. 2012.
15. Braun, R. D., Mitcheltree, R. A., Cheatwood, F. M., Mars Microprobe Entry Analysis, Proc., *IEEE Aerospace Conference Proc.*, IEEE, Feb. 1997.
16. Holden, M., Moselle, J., Wieting, A., Glass C, Studies of Aerothermal Loads Generated in Regions of Shock/Shock Interaction in Hypersonic Flow, *26th Aerospace Sciences Meeting*, Jan. 1988.
17. *Models of Mars' Atmosphere*, NASA TM 19750011035, NASA GSFC, 1974.
18. Anderson, J. D., Wendt, J., *Computational Fluid Dynamics*, McGraw-Hill, 1995.

19. Park, C., Howe, J. T., Jaffe, R. L., Candler, G. V., Review of Chemical-Kinetic Problems of Future NASA Missions, II: Mars Entries. *Journal of Thermophysics and Heat Transfer*, Vol. 8, No. 1, 1994, pp. 9-23.
20. Meakin, R. L., Composite Overset Structured Grids. *Handbook of Grid Generation*, 1999, pp. 1-20.
21. Allen, H. J., Eggers A. J, A Study of the Motion and Aerodynamic Heating of Ballistic Missiles Entering the Earth's Atmosphere at High Supersonic Speeds. NACA TM 1381, 1958.

APPENDIX A

SIMULATION SURFACE PLOTS

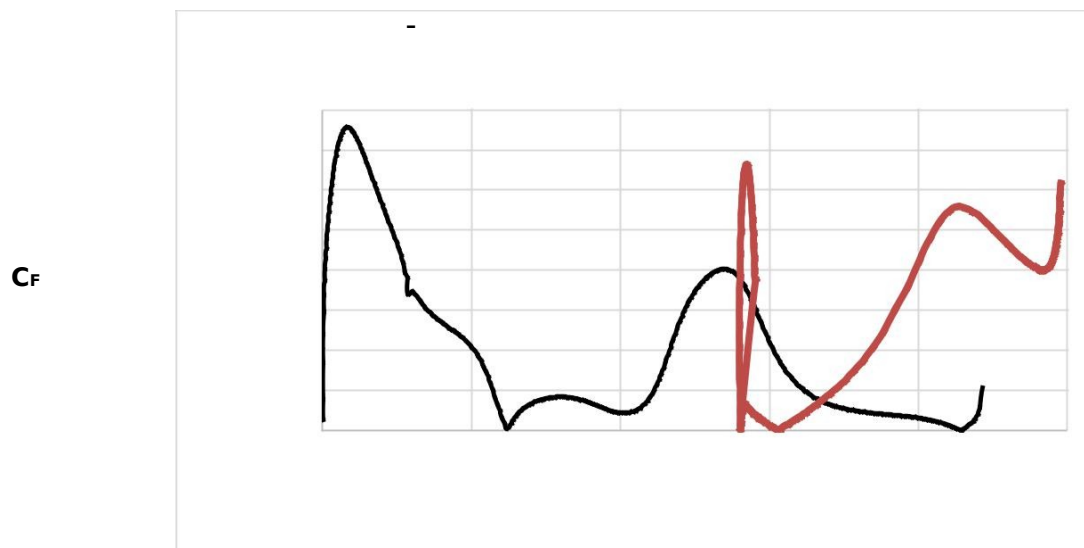
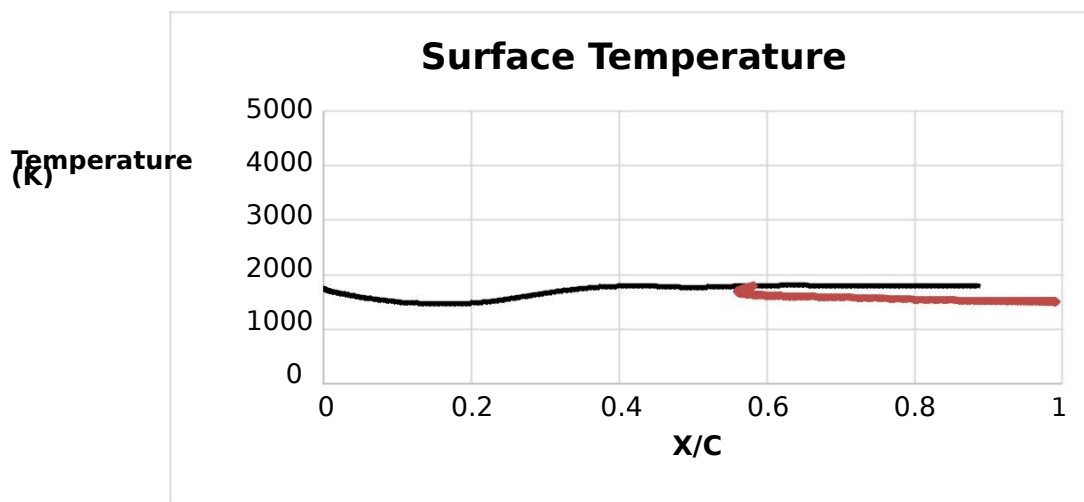
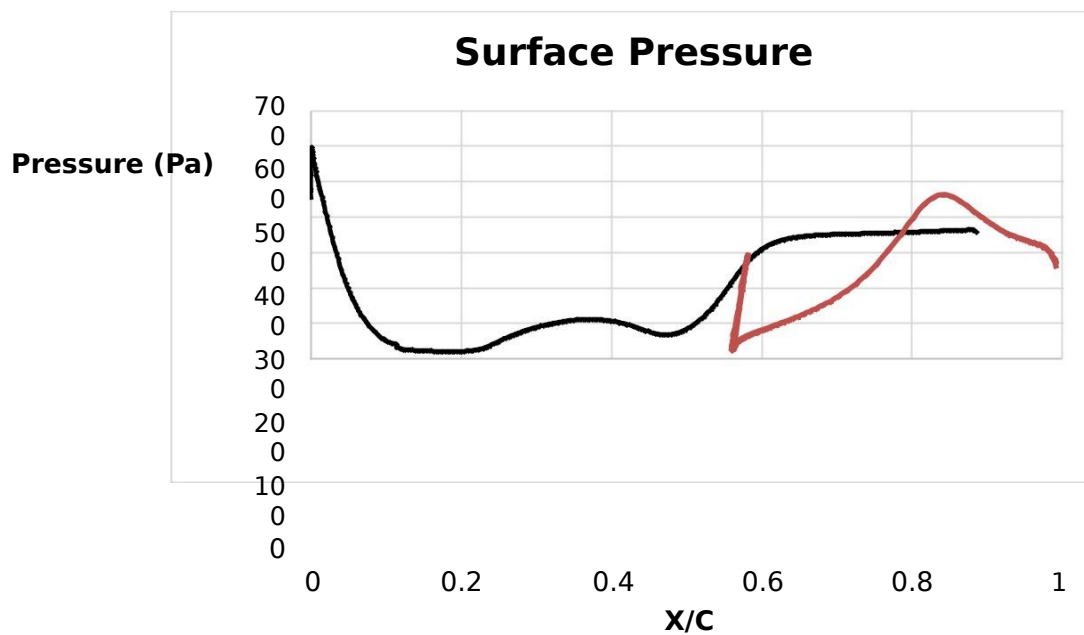
Appendix A contains surface pressure, temperature and calculated skin friction coefficient plots for each simulation. Each plot is overlaid on a near body flow field contour plot produced with the ESI CFD-VIEW post processing tool. Pressure and temperature data is presented with pressure and temperature contours while skin friction coefficient data is overlaid on the Mach contour. This data is also presented in Appendix B comparing the same data in each simulation case by body shape.

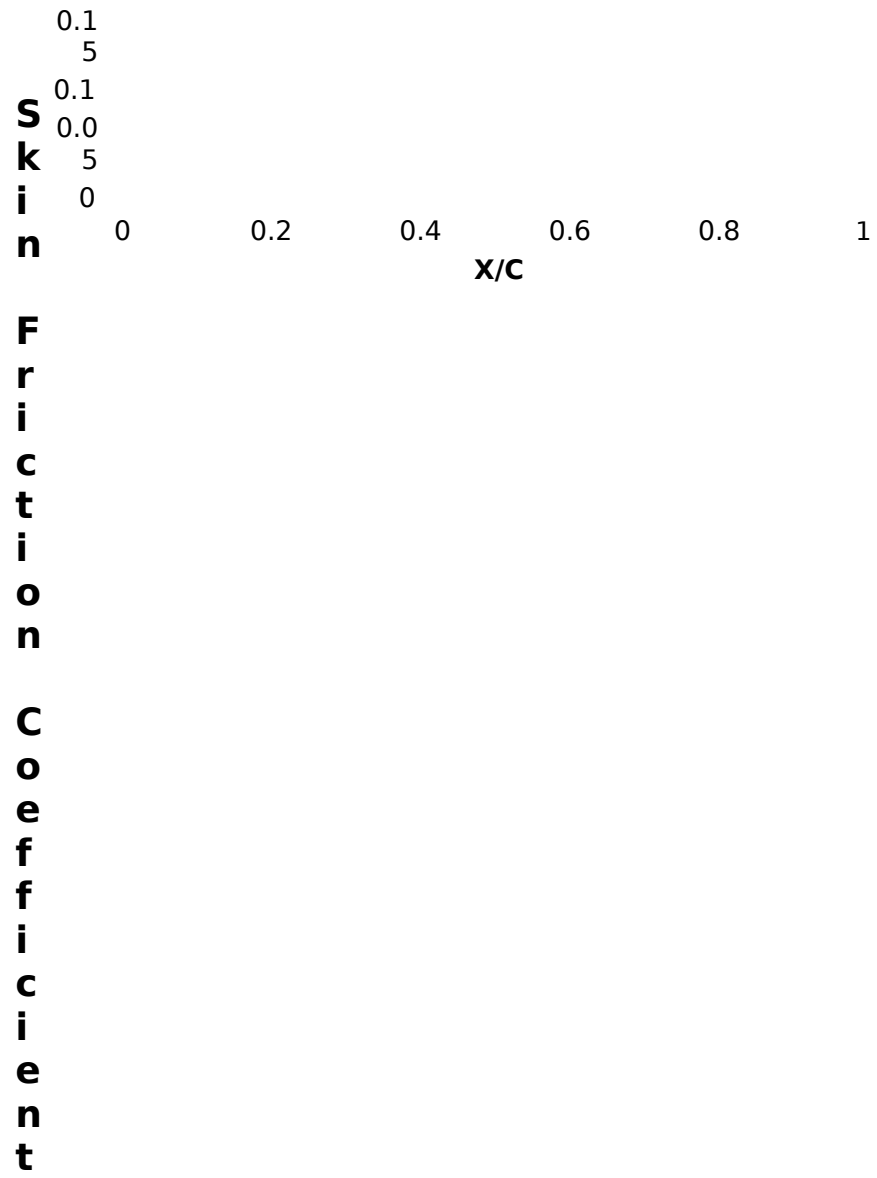
Legend applying to all plots in Appendix A:

Body Surface

Flare Front Surface

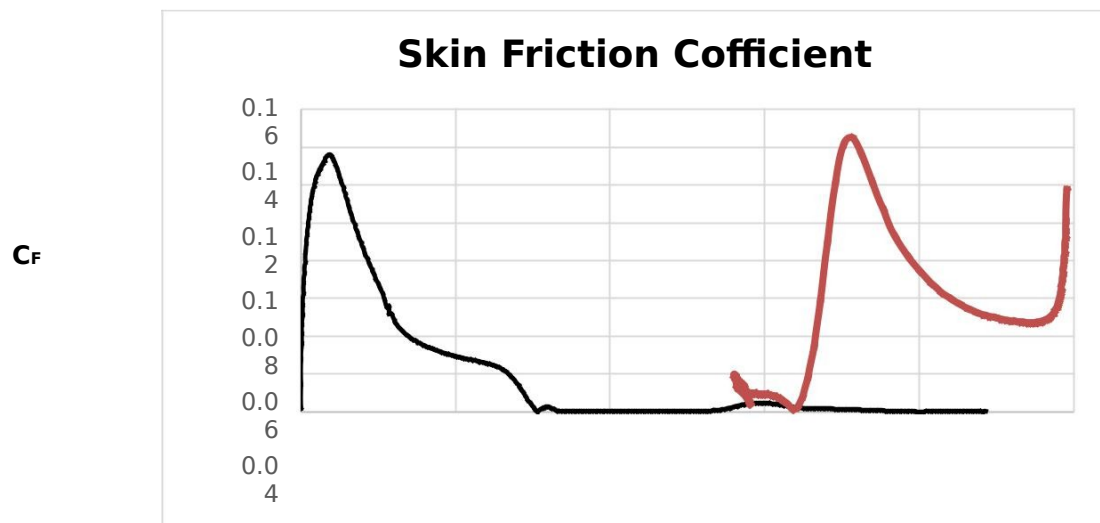
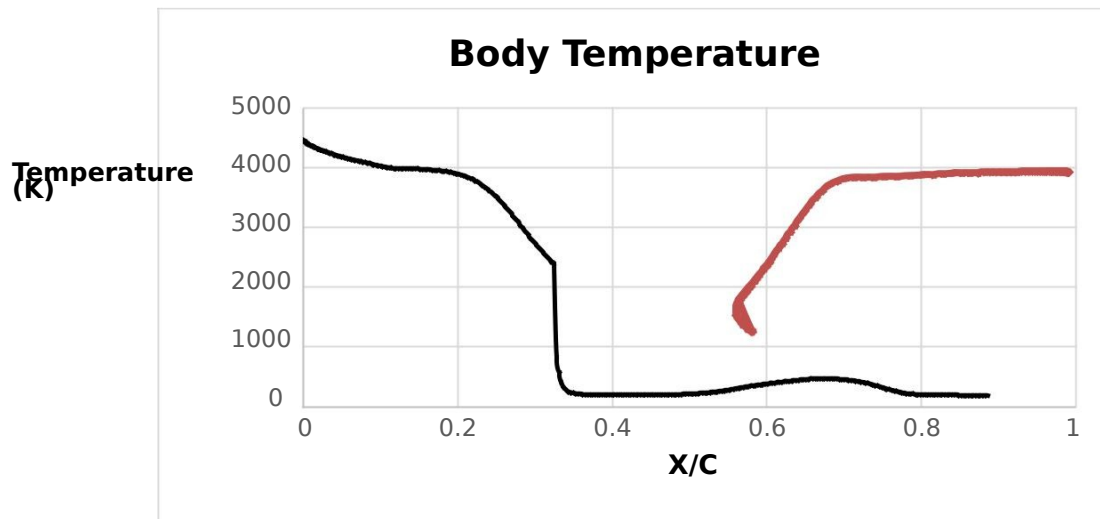
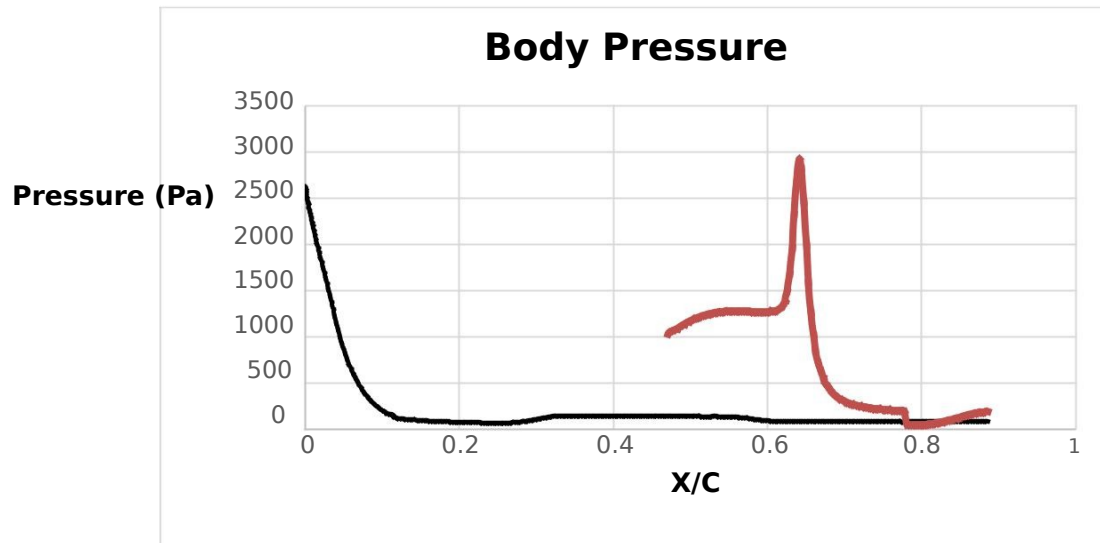
Case B – Nominal Geometry





0
 .4
 0
 .3
 5
 0
 .3
 0
 .2
 5
 0
 .2

Case C – Nominal Geometry

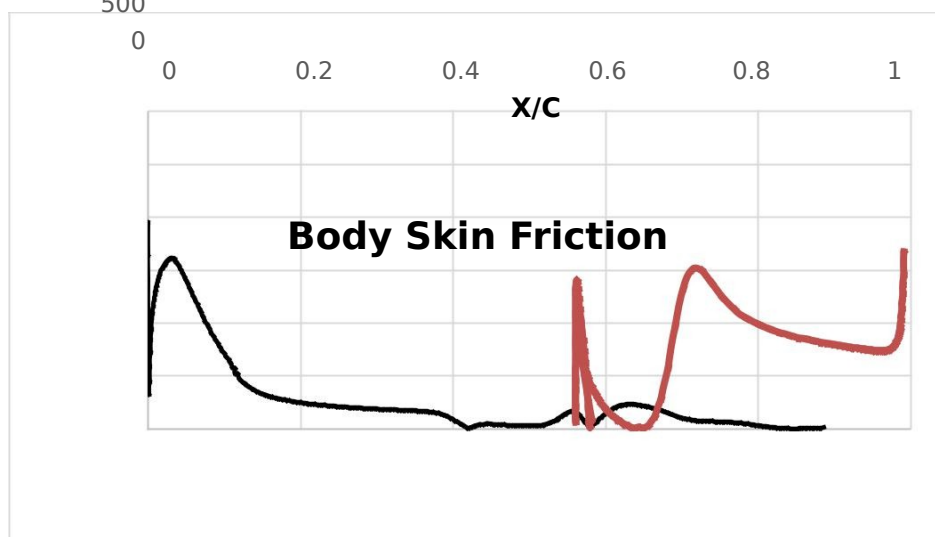
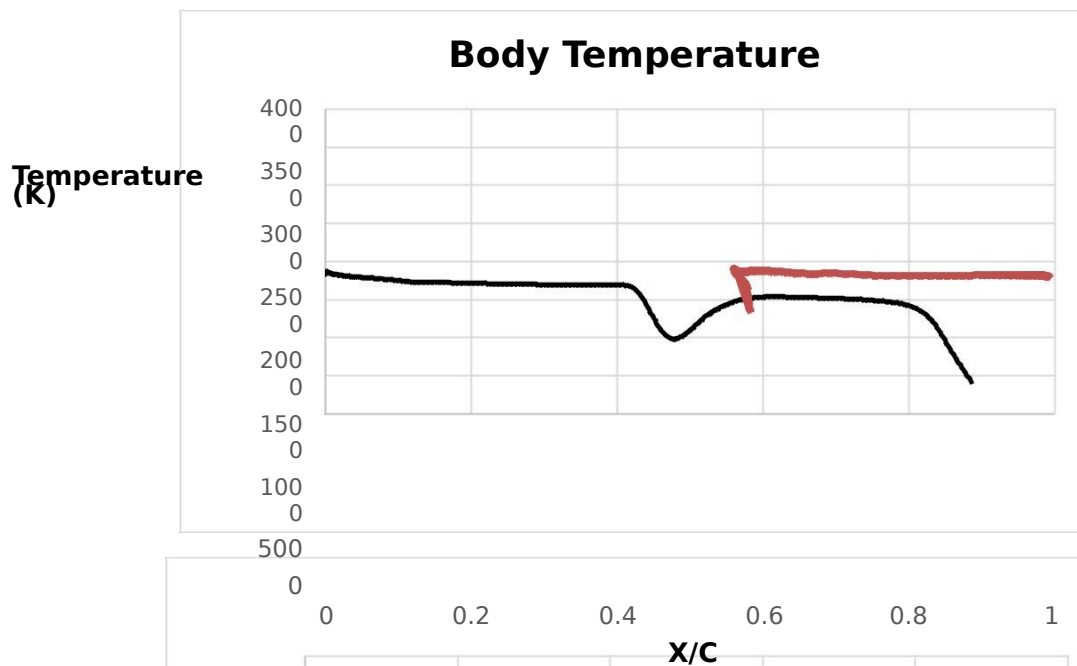
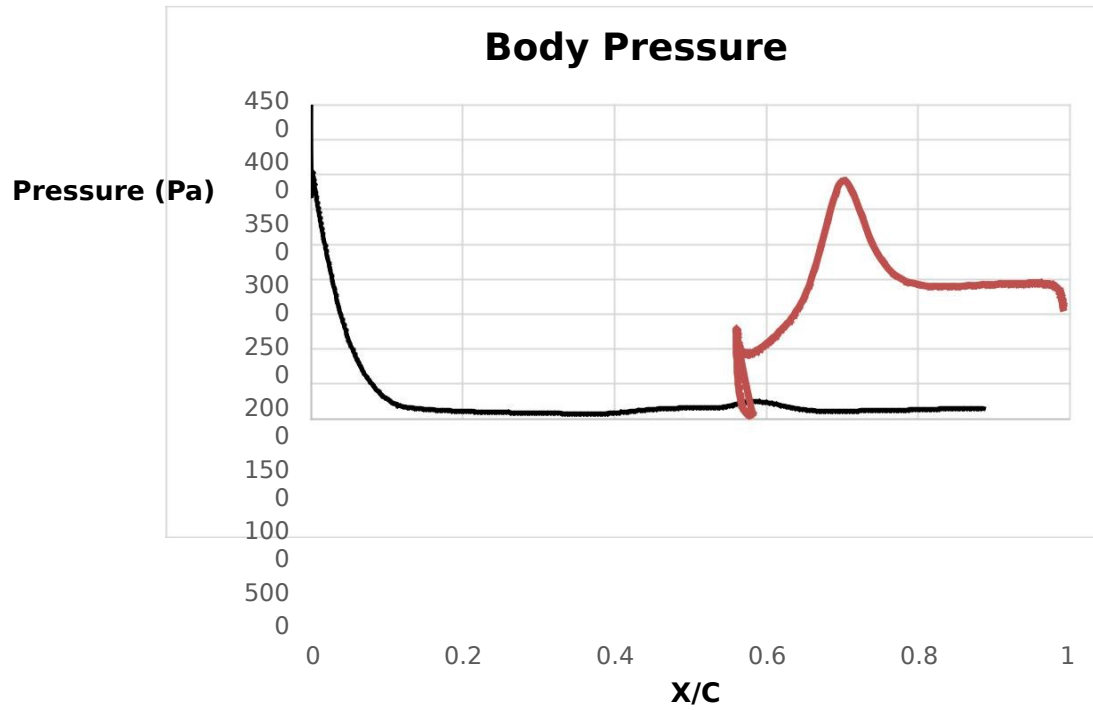


0
·
0
2

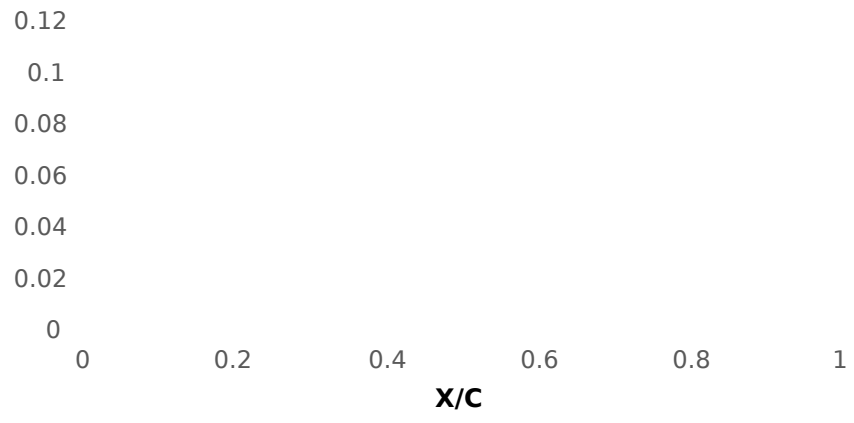
0 0.2 0.4 0.6 0.8 1

X/C

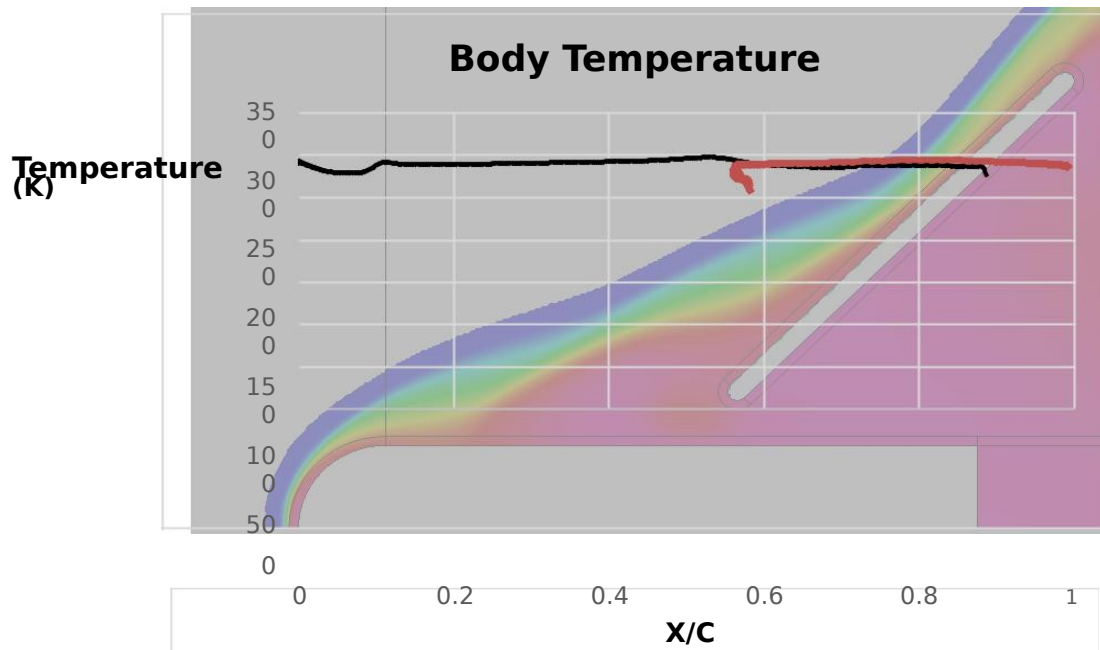
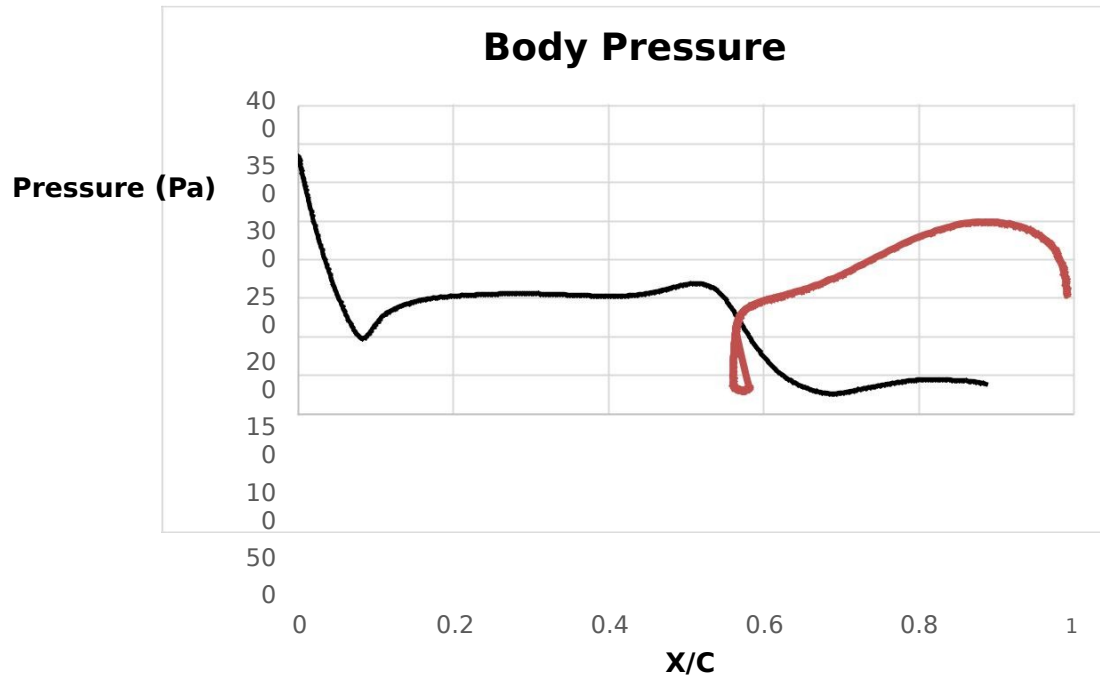
Case D – Nominal Geometry



C_F

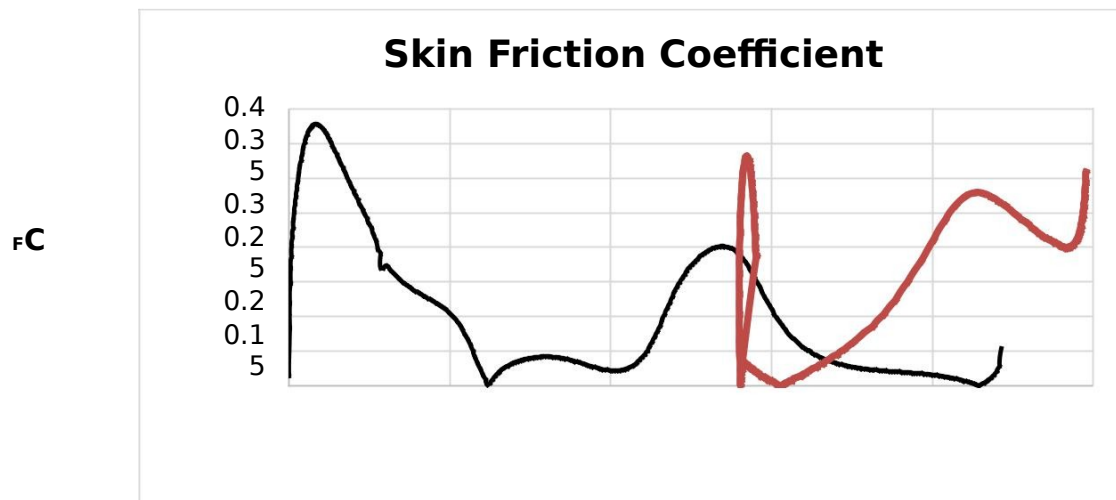
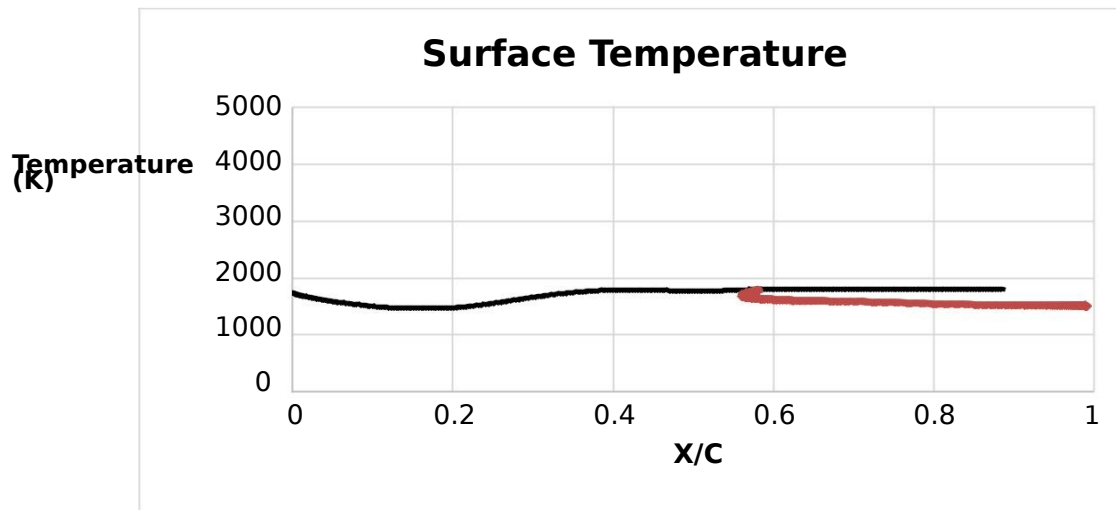
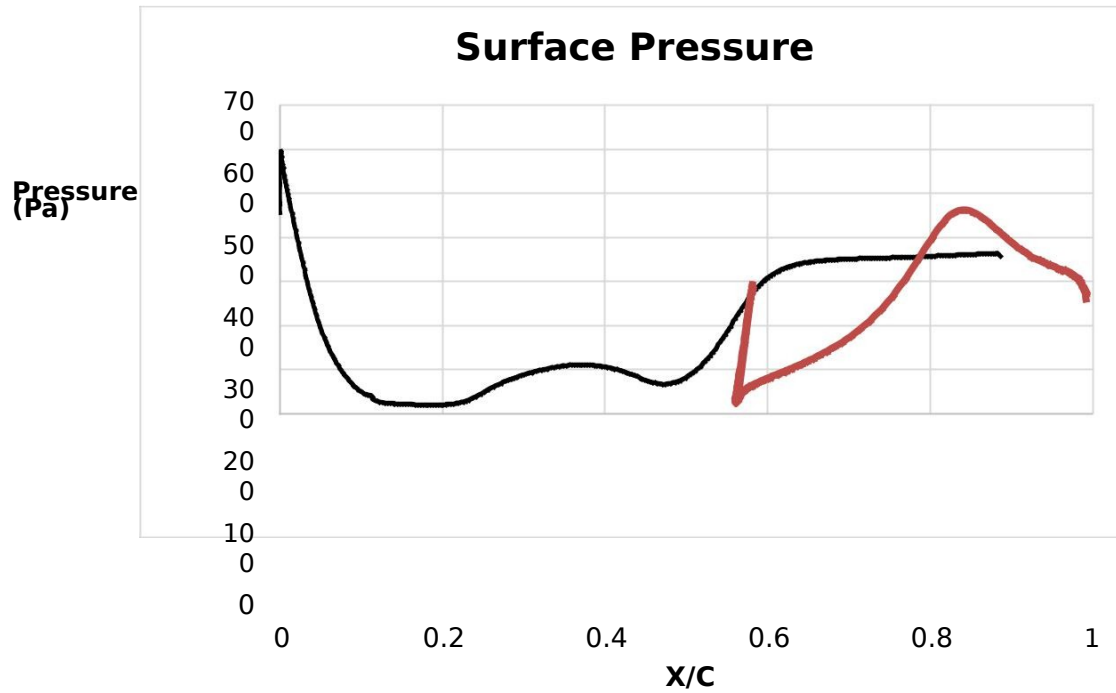


Case E – Nominal Geometry





Case B – Gap Geometry



0
.
1
0
.
0
5
0

0

0.2

0.4

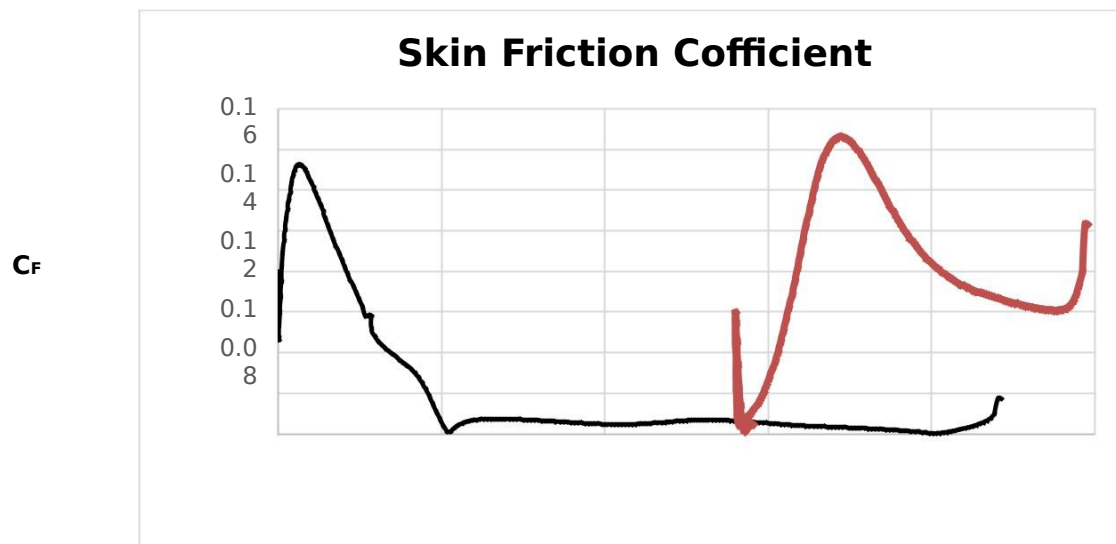
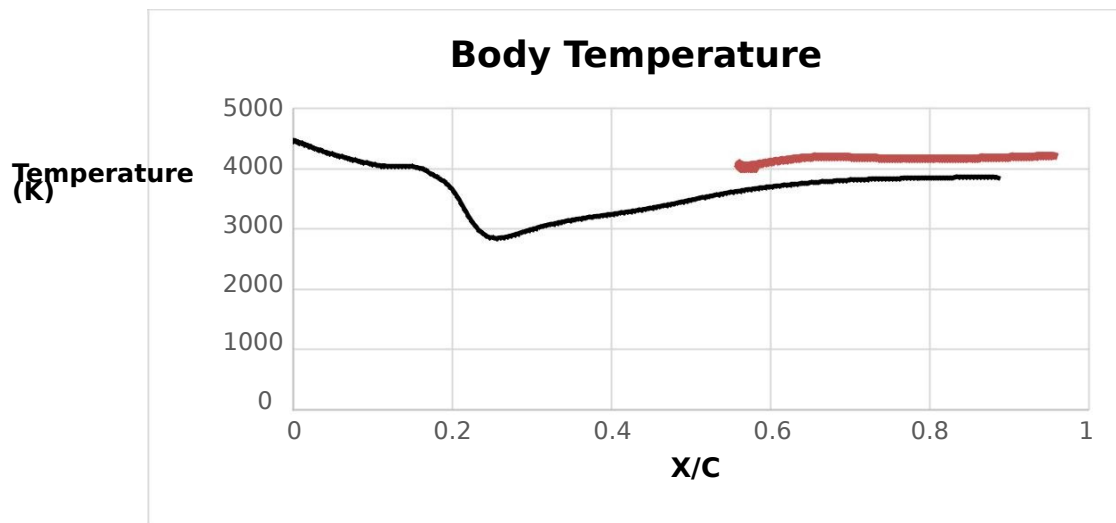
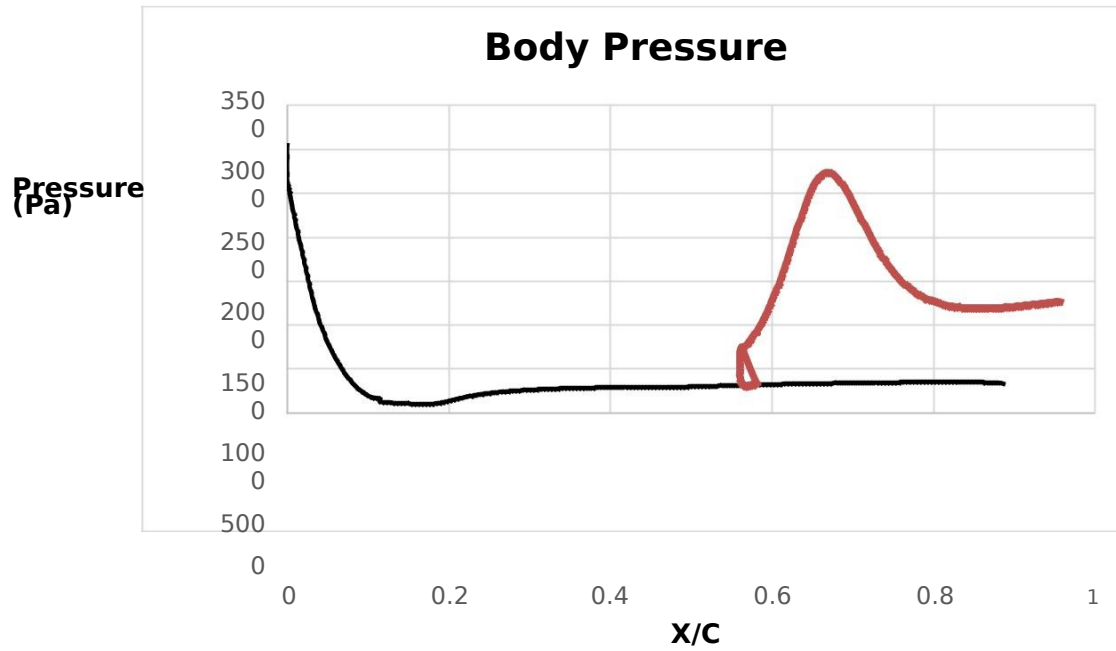
0.6

0.8

1

X/C

Case C – Gap Geometry



0
.
0
6

0.0
4
0.0
2
0

0

0.2

0.4

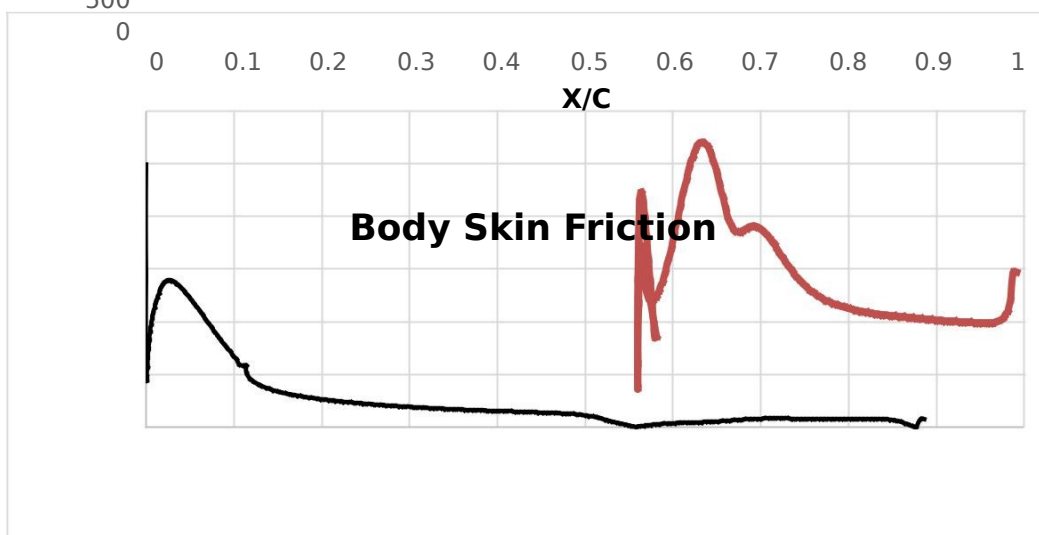
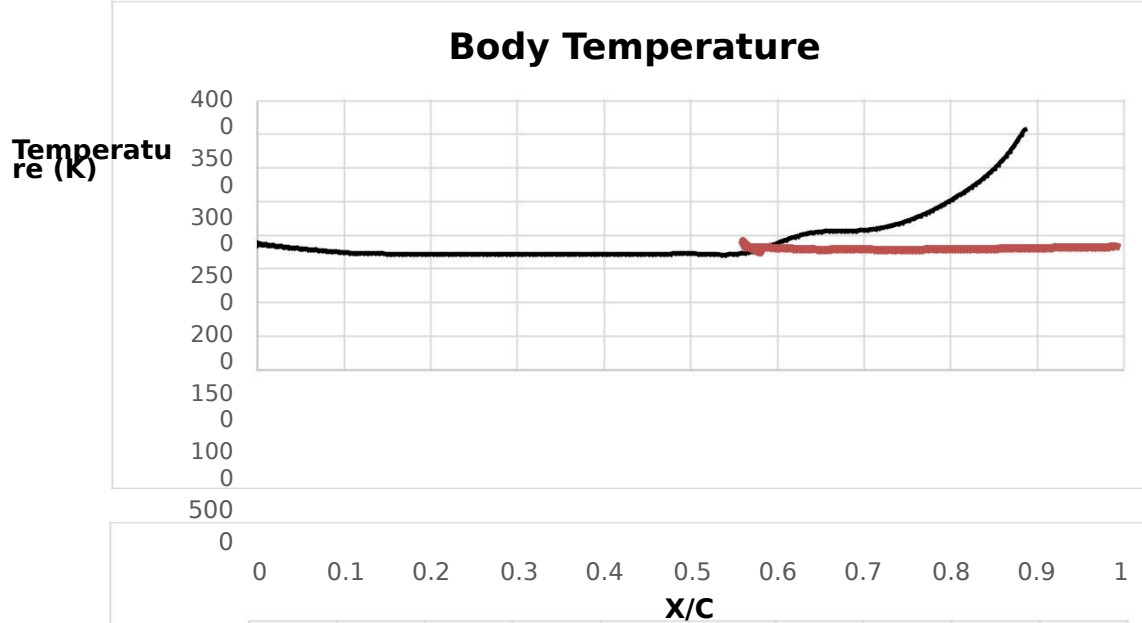
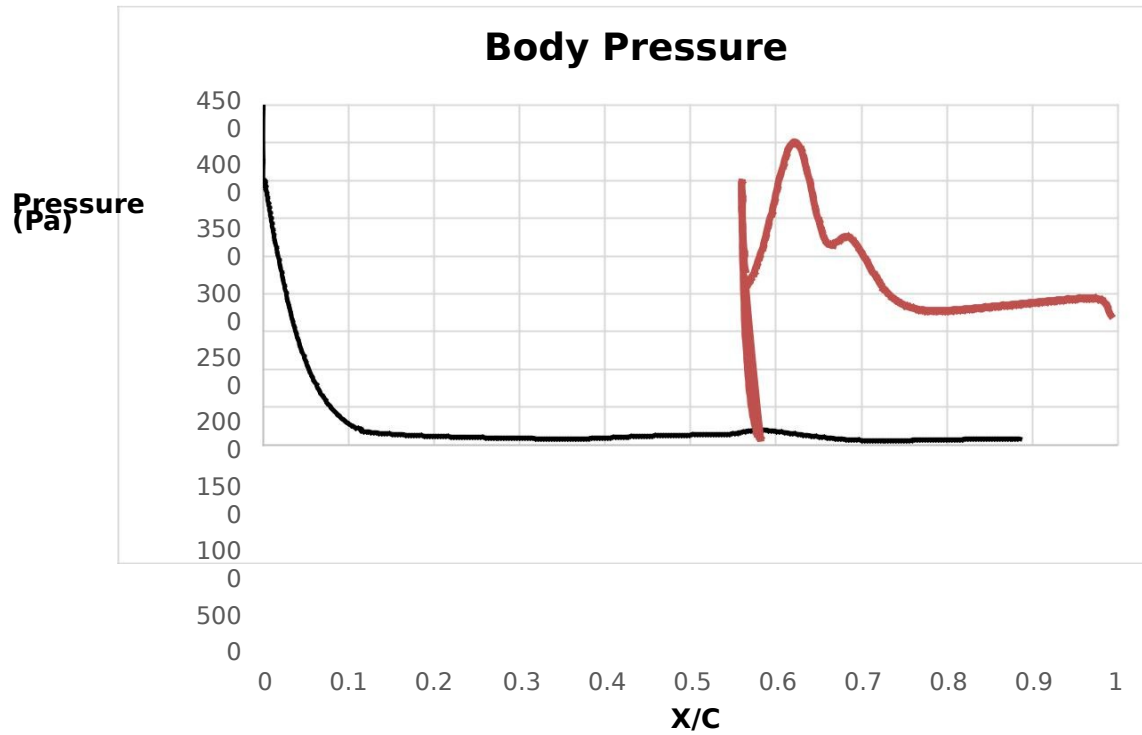
0.6

0.8

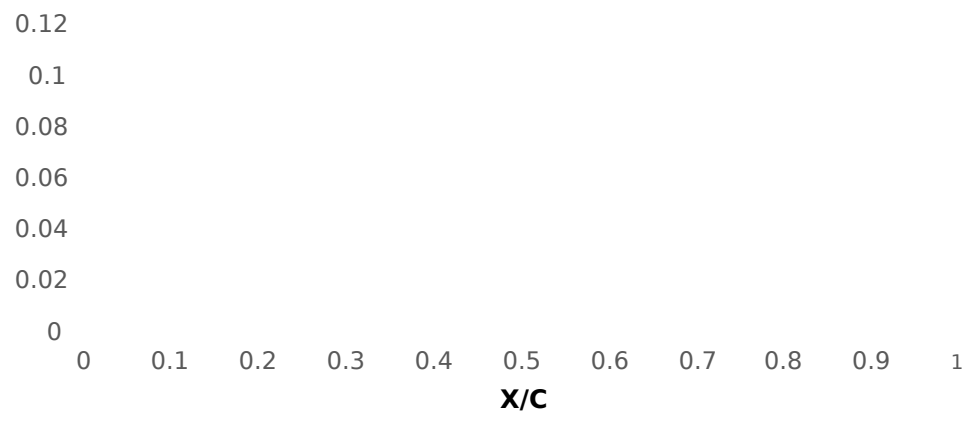
1

X/C

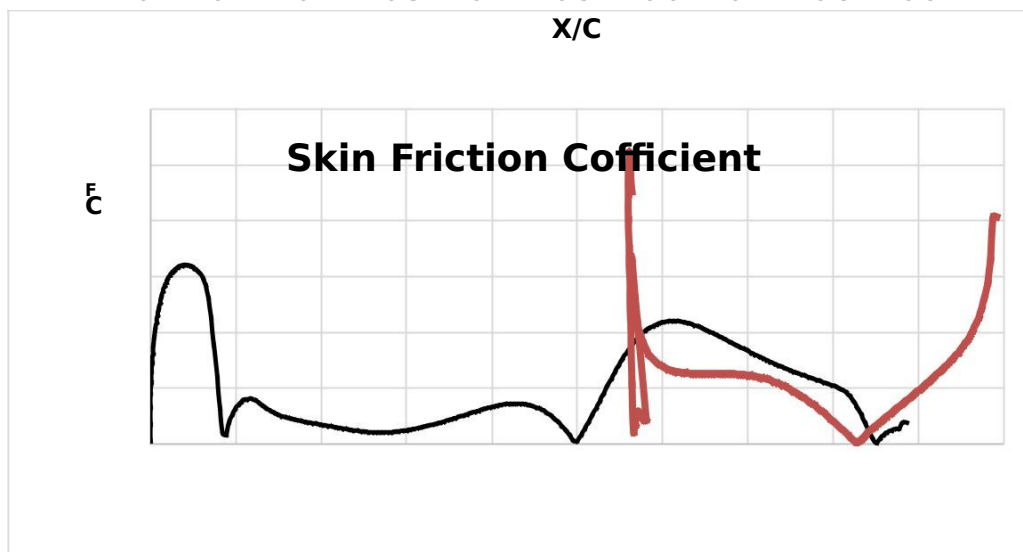
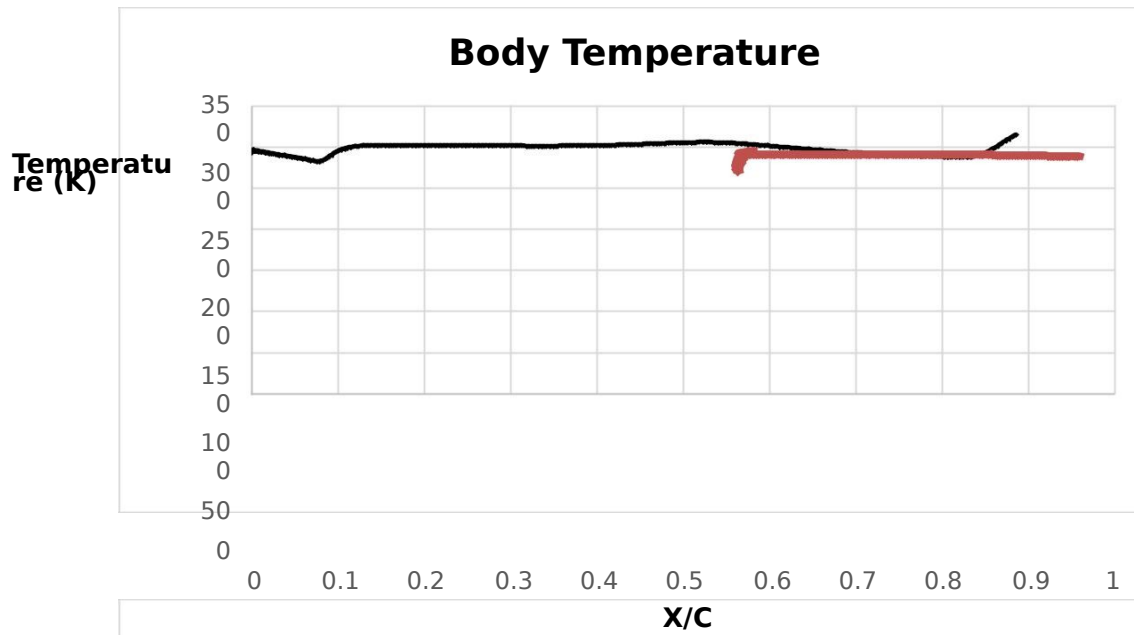
Case D – Gap Geometry



C_F

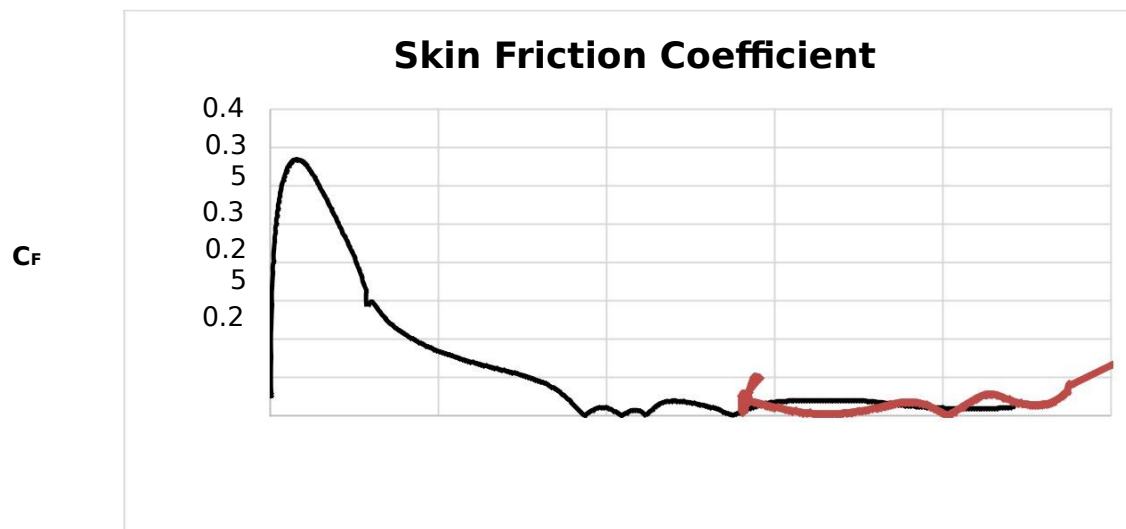
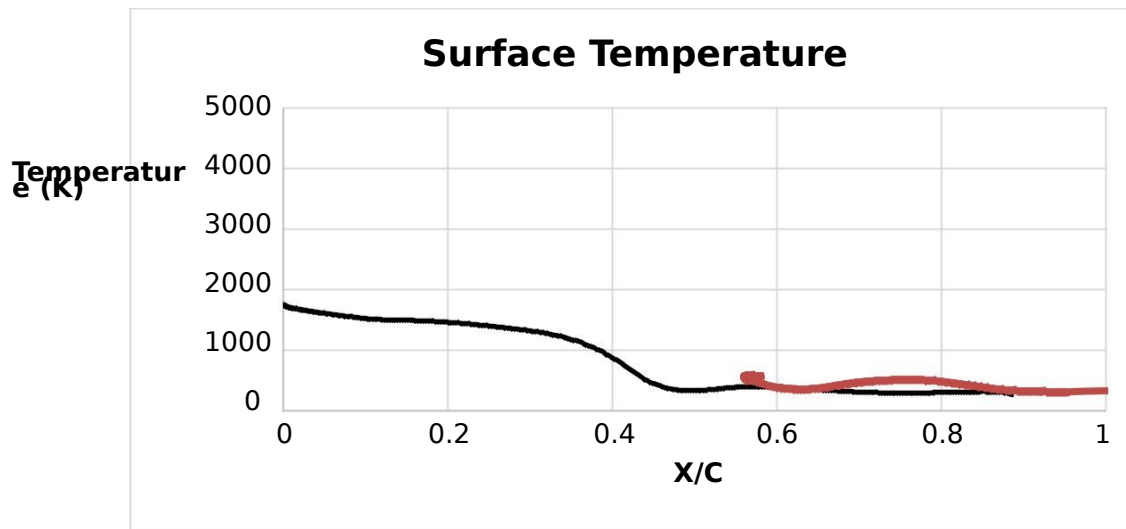
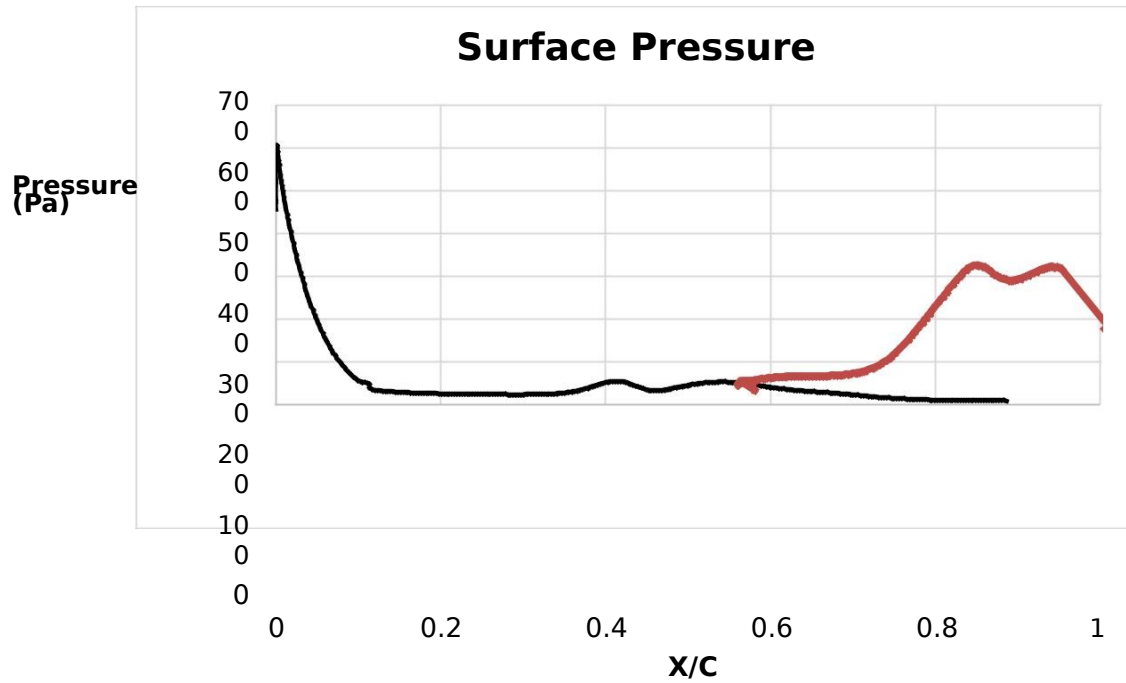


Case E – Gap Geometry





Case B – Shoulder Geometry



0
.
1
5
0
.
1
0
.
0
5
0

0

0.2

0.4

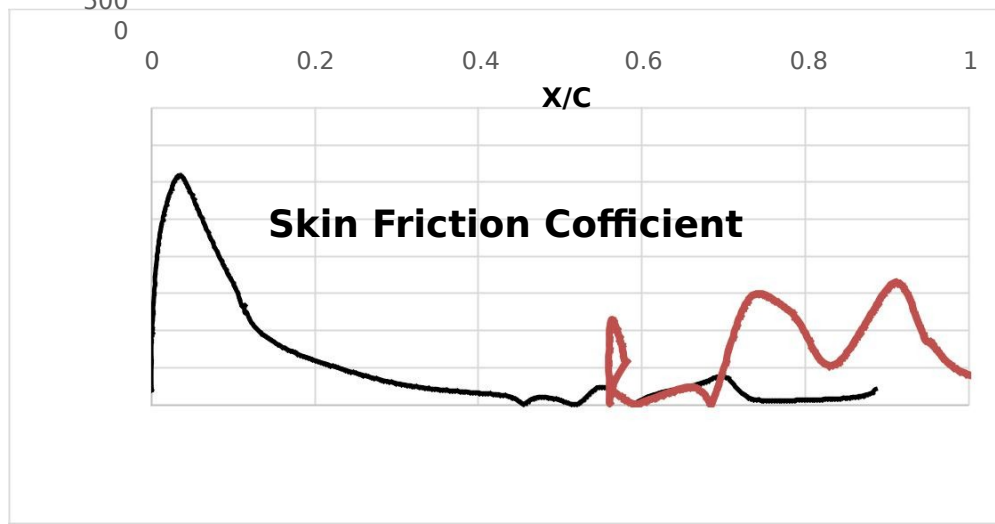
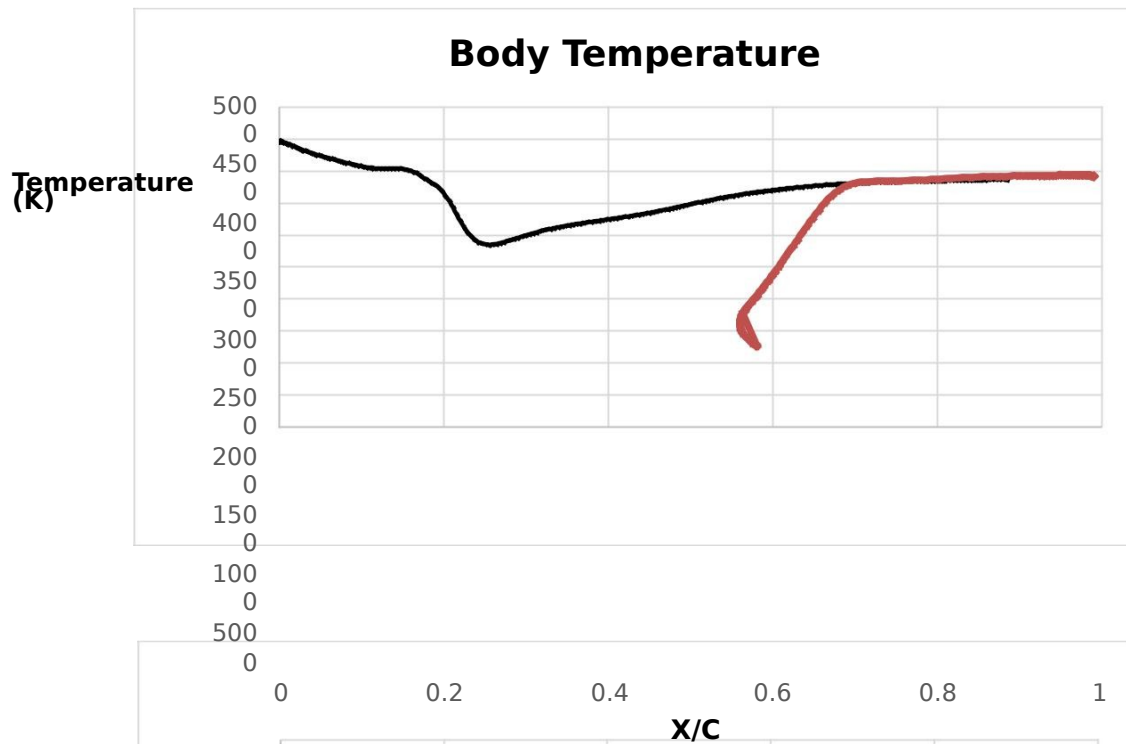
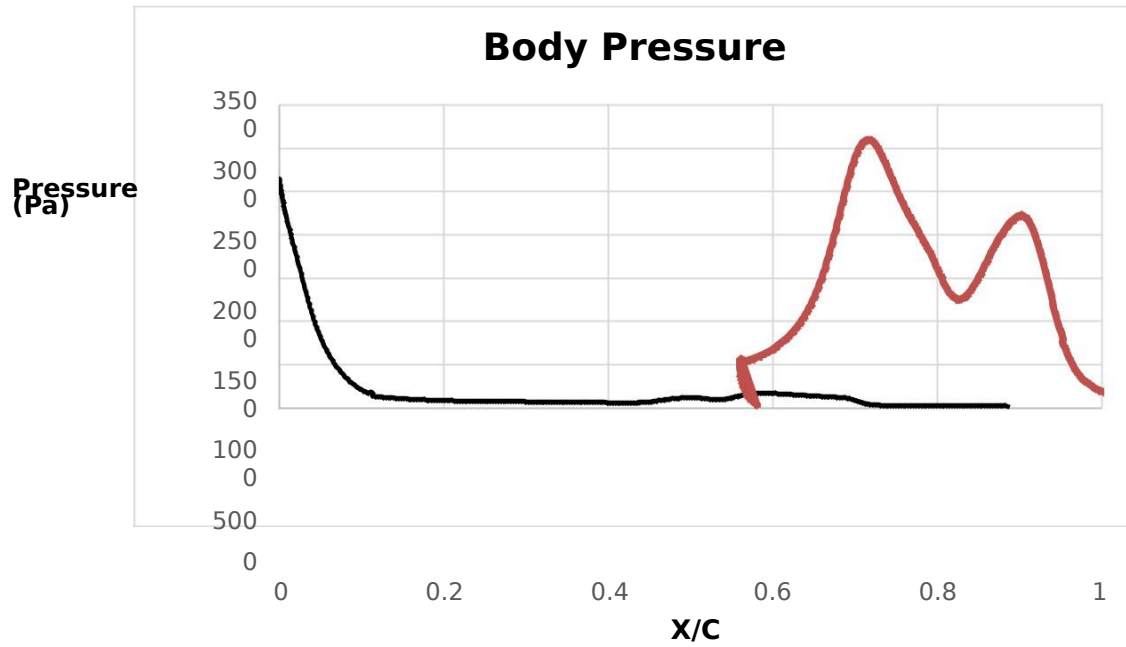
0.6

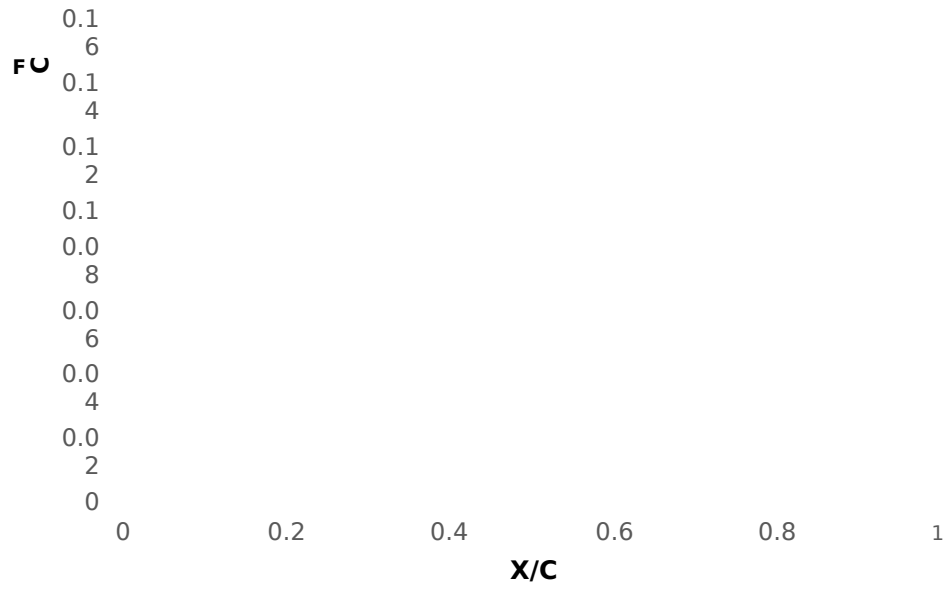
0.8

1

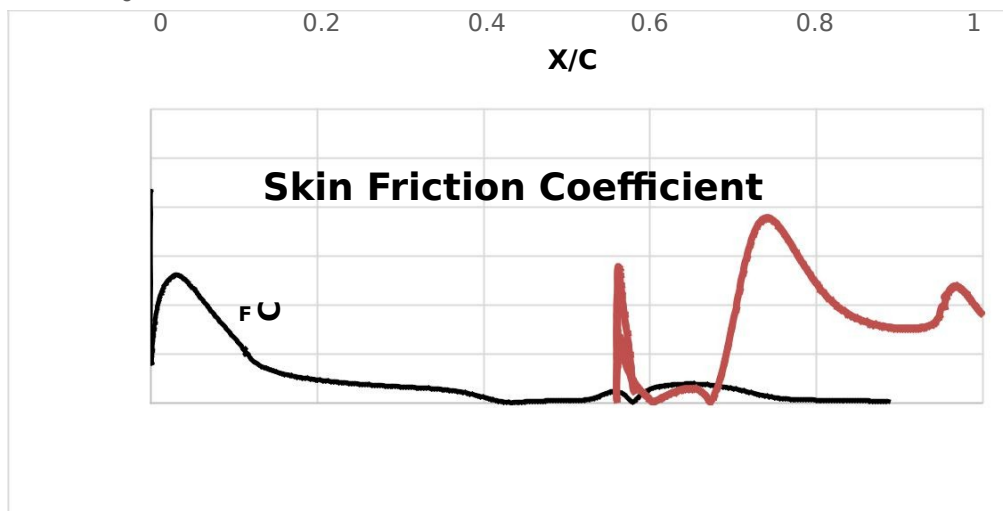
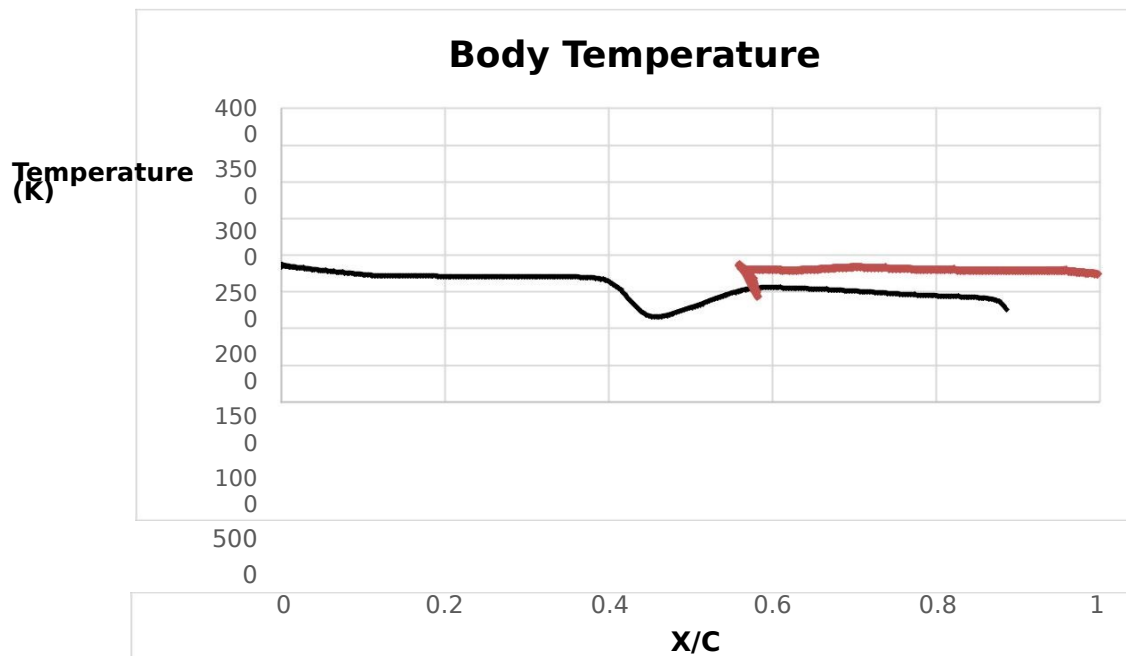
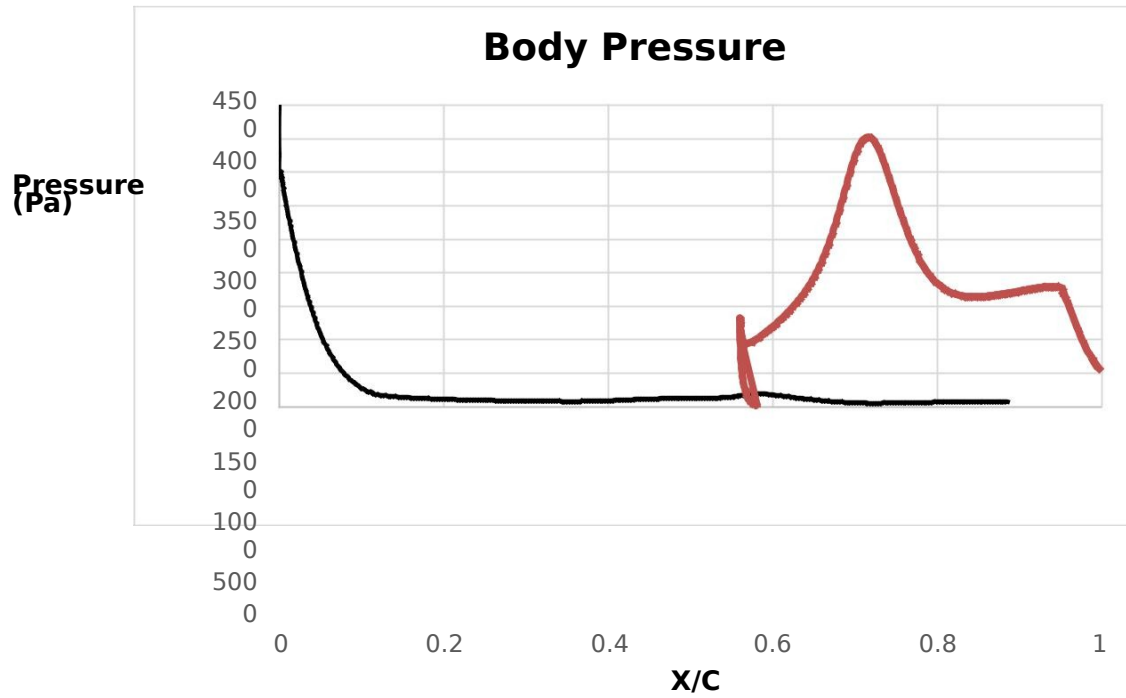
X/C

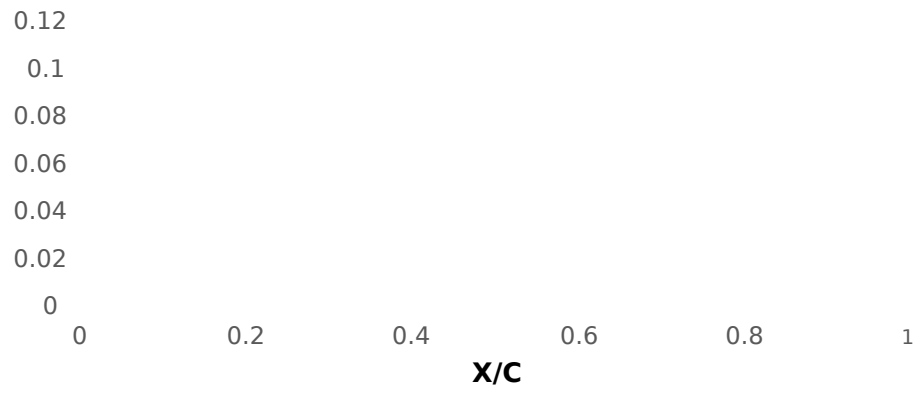
Case C – Shoulder Geometry



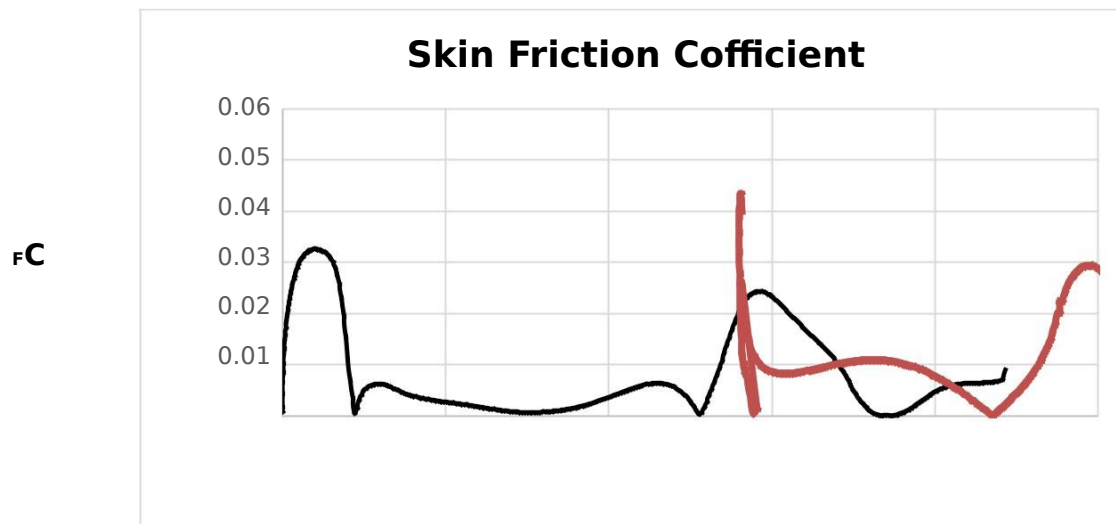
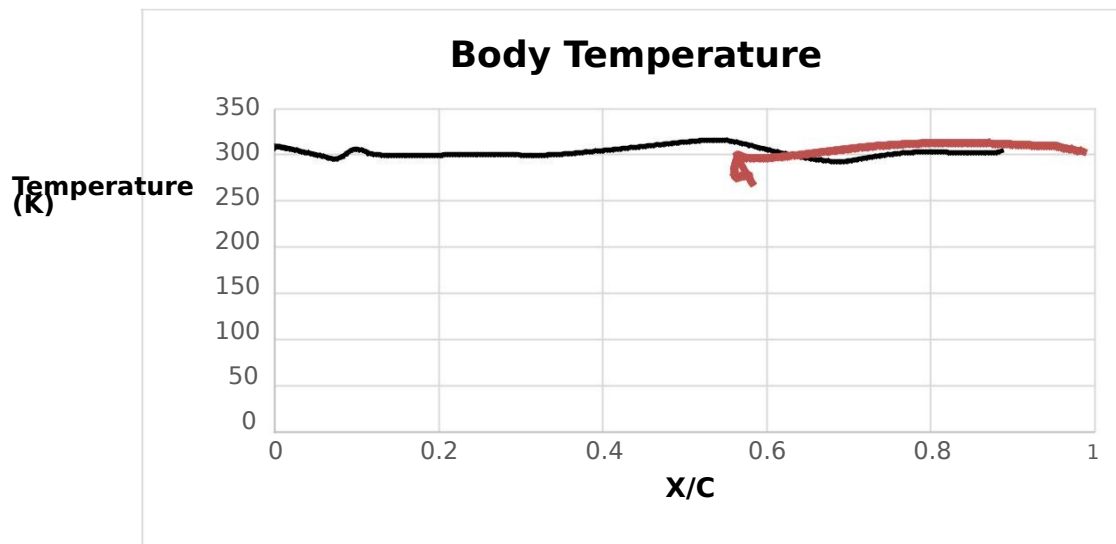
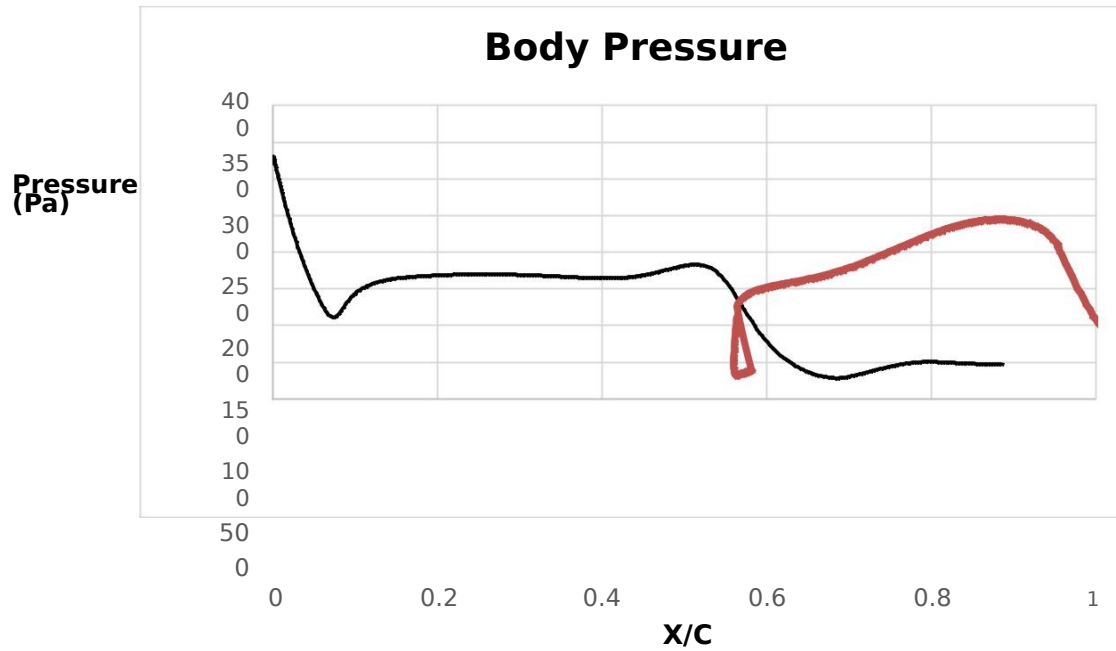


Case D – Shoulder Geometry





Case E – Shoulder Geometry



0

0

0.2

0.4

0.6

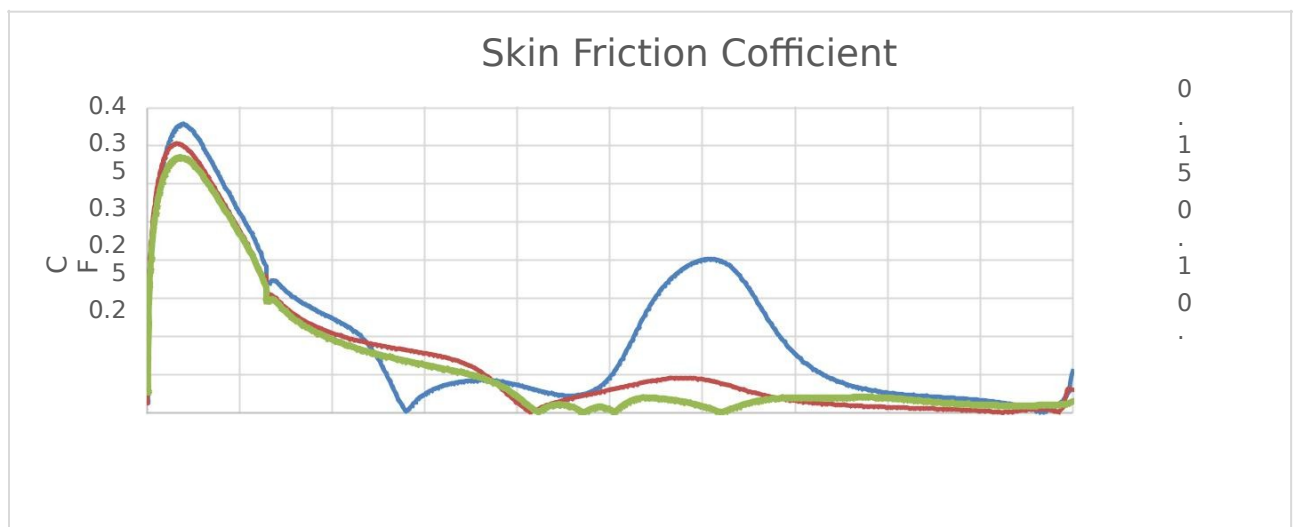
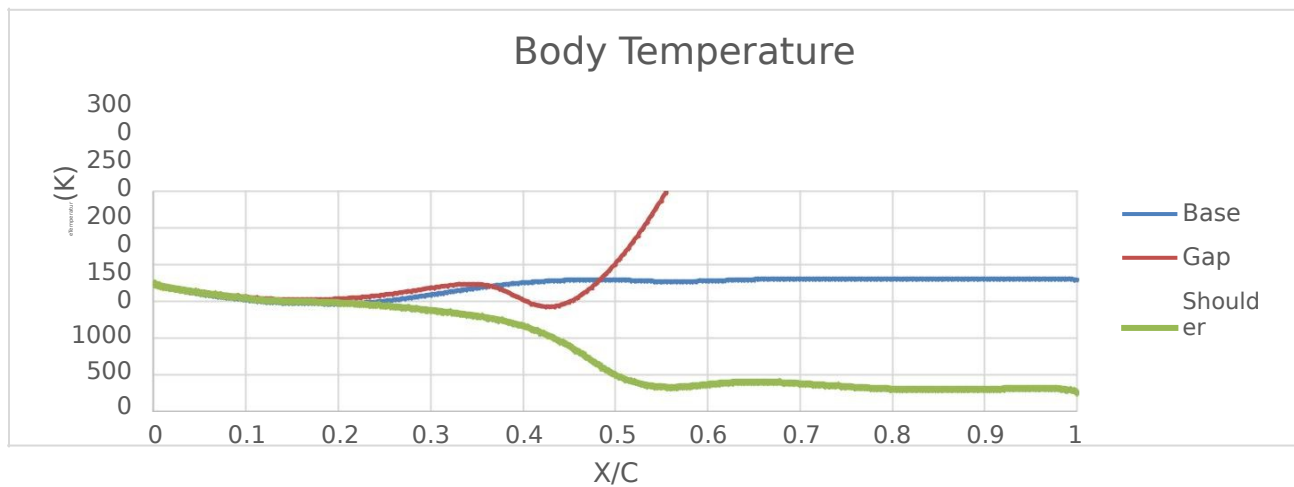
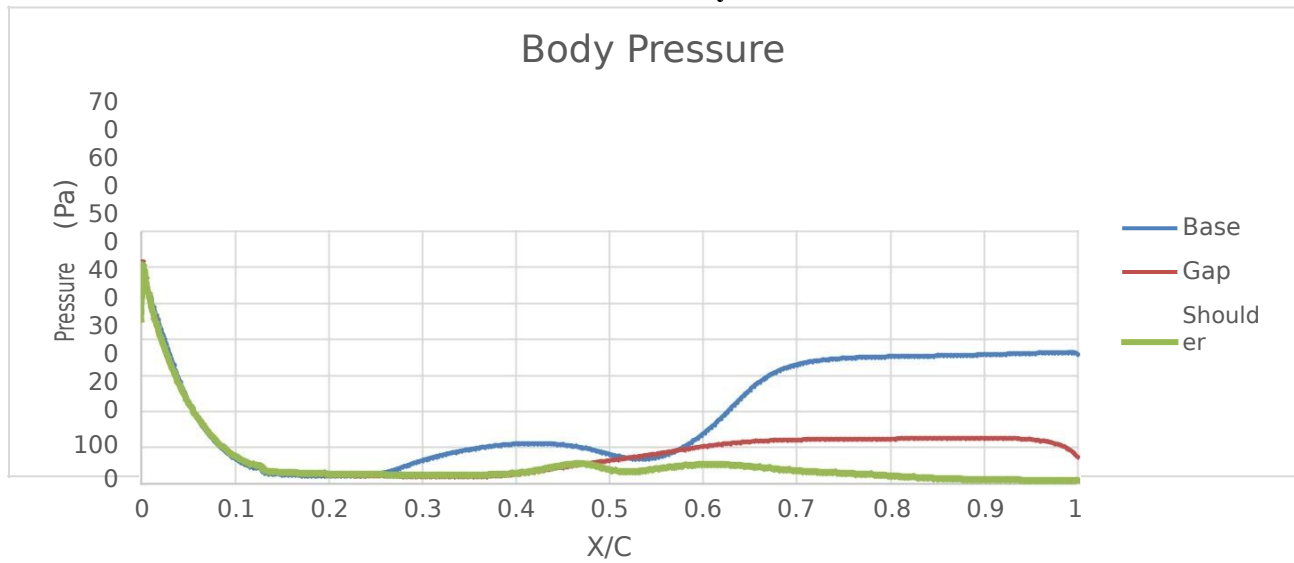
0.8

1

X/C

APPENDIX B
PARAMETRIC SURFACE PLOTS

Case B – Body



0
5
0

0

0 Base

1 Gap

0 Shoulder

.
2

0

.
3

0

.
4

0

.
5

0

.
6

0

.
7

0

.
8

0

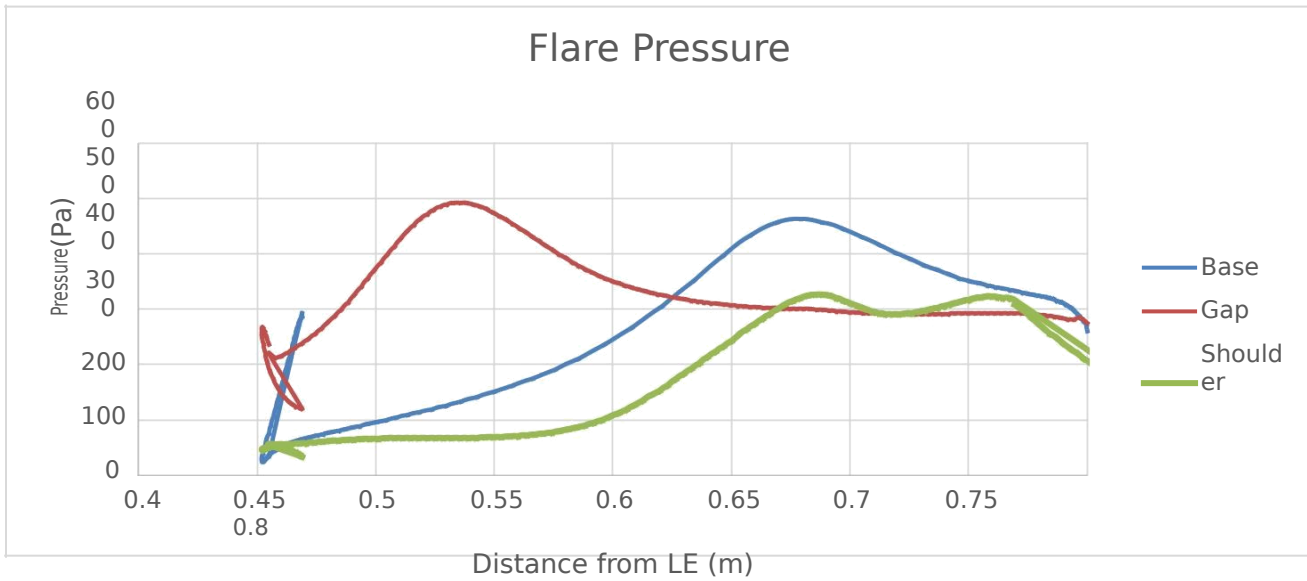
.
9

1

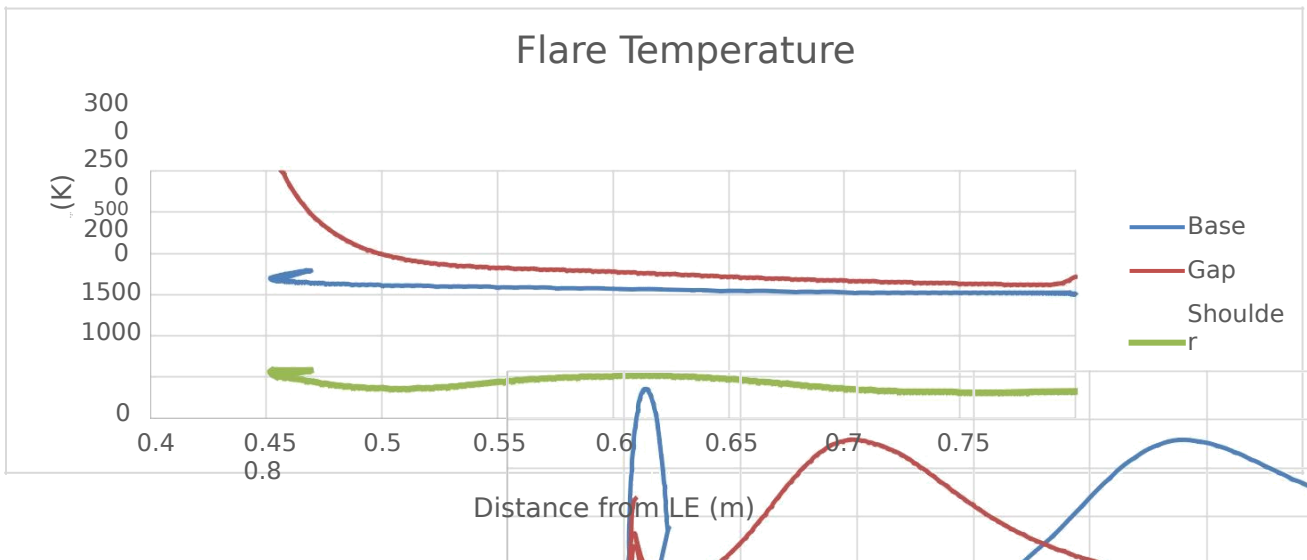
X/C

Case B – Flare

Flare Pressure



Flare Temperature

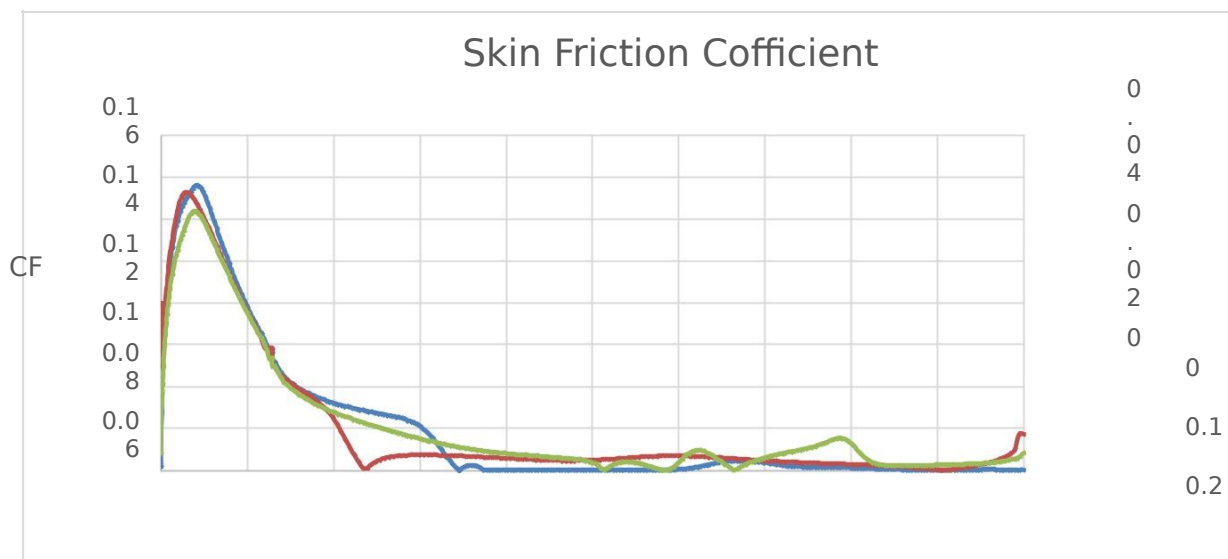
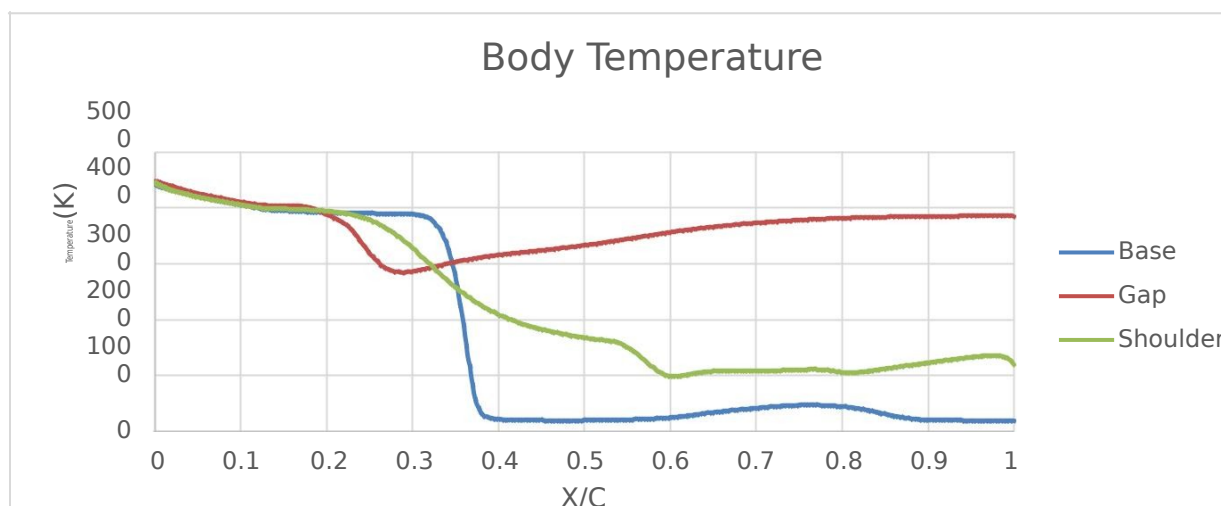
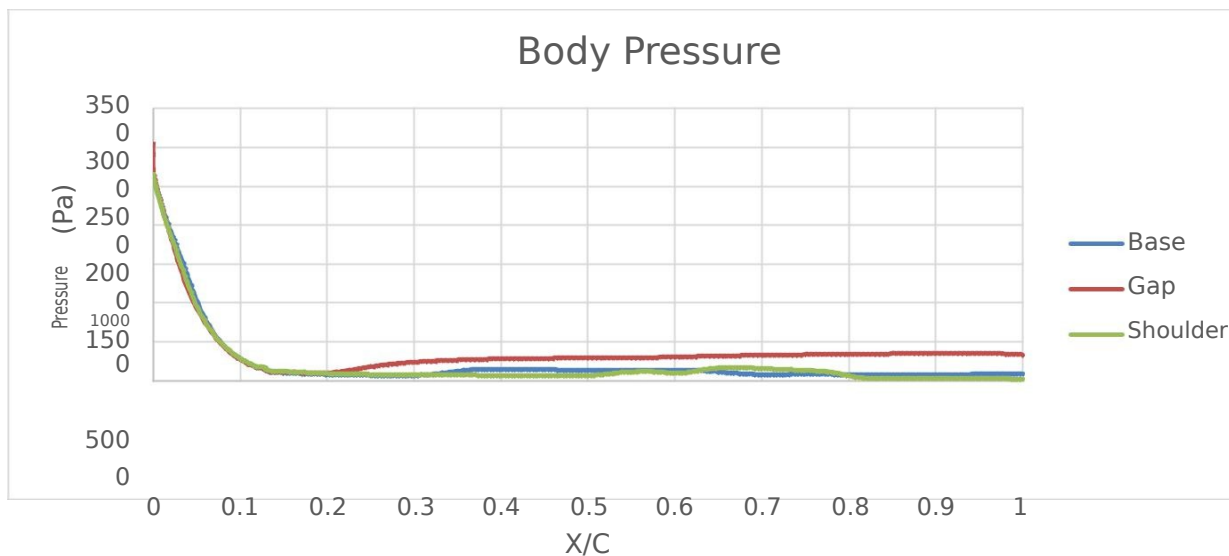


Skin Friction Coefficient



— Base
— Gap
— Shou
— lder

Case C – Body



0

.

3

0

— Base

4

— Gap

0

— Shoulder

.

5

0

.

6

0

.

7

0

.

8

0

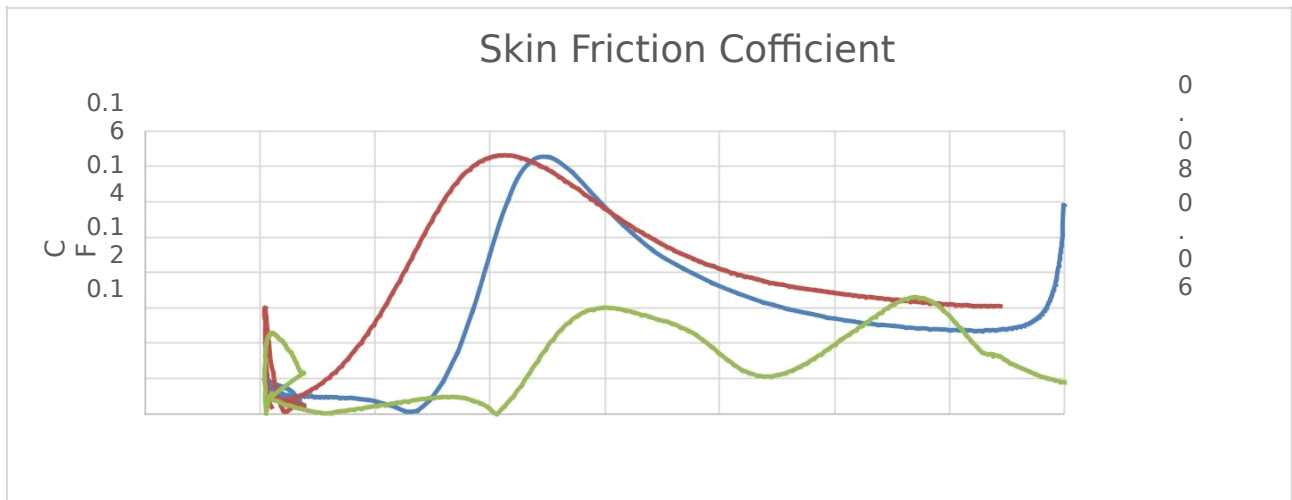
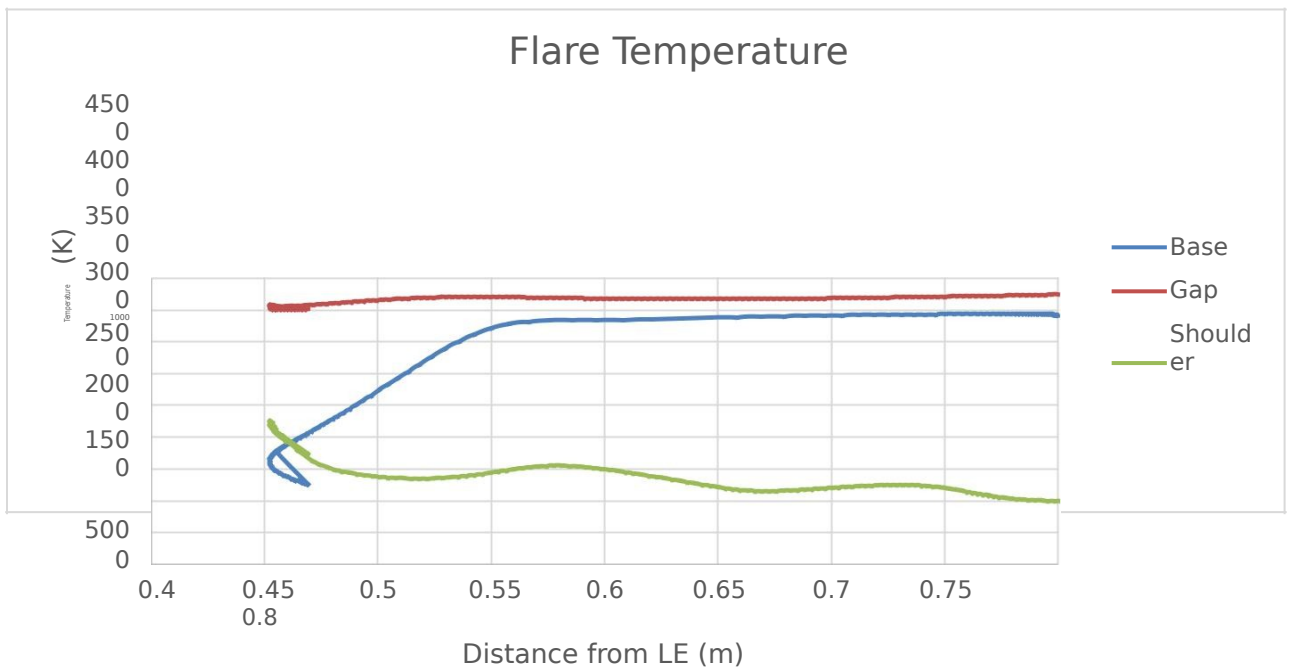
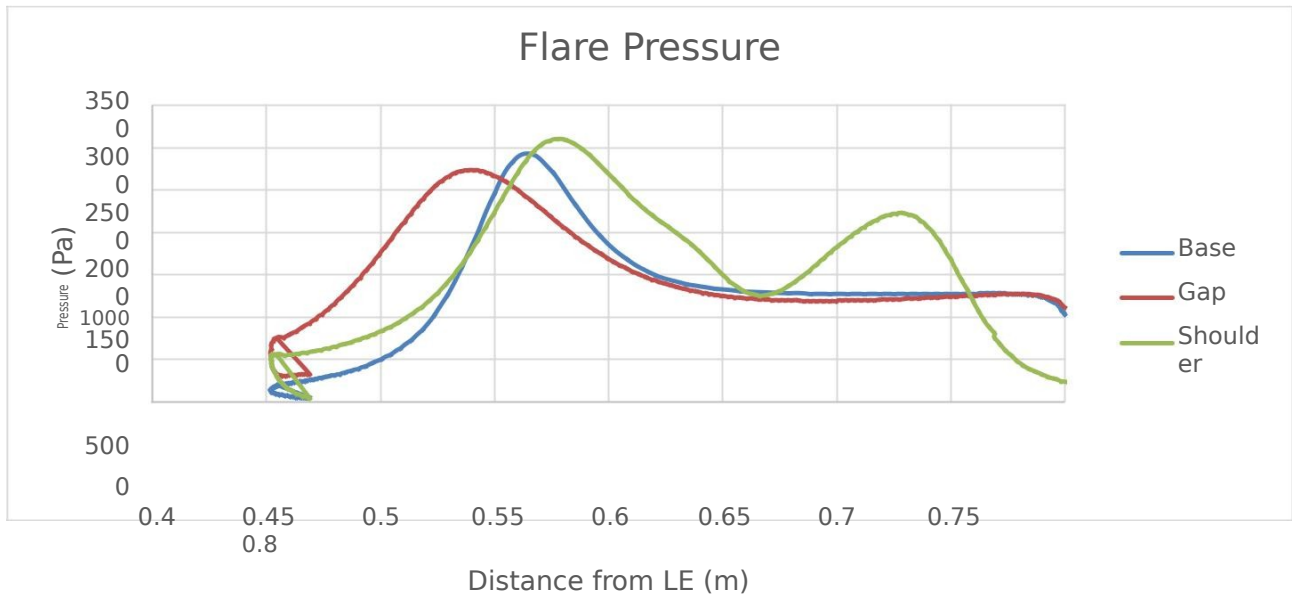
.

9

1

X/C

Case C – Flare

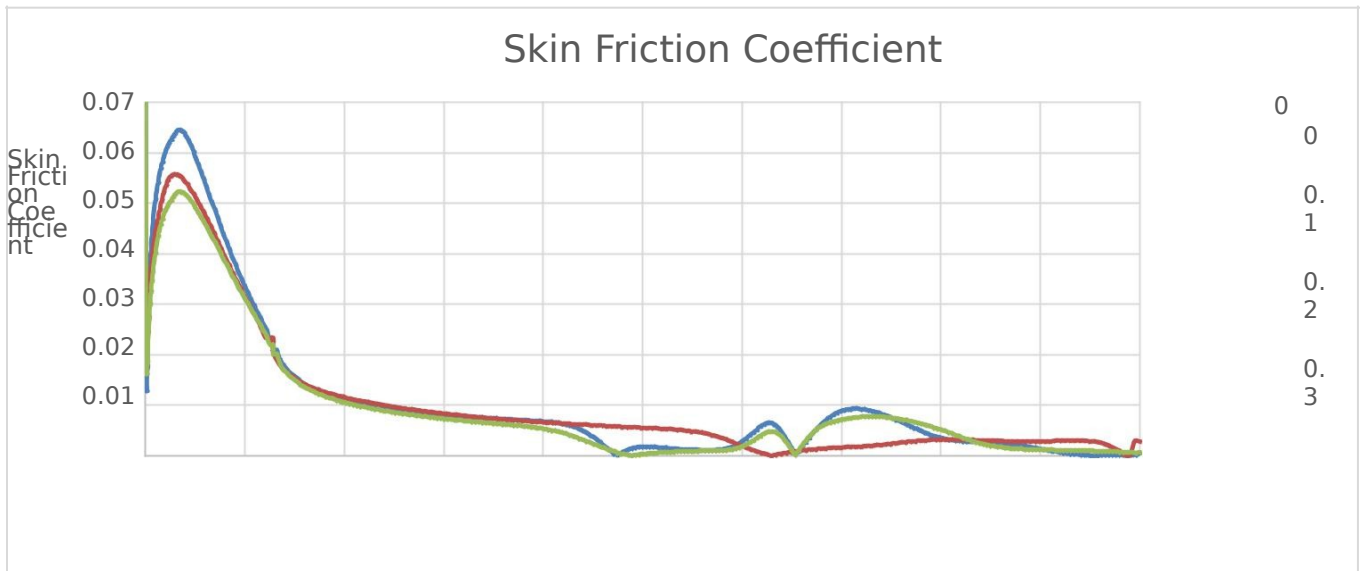
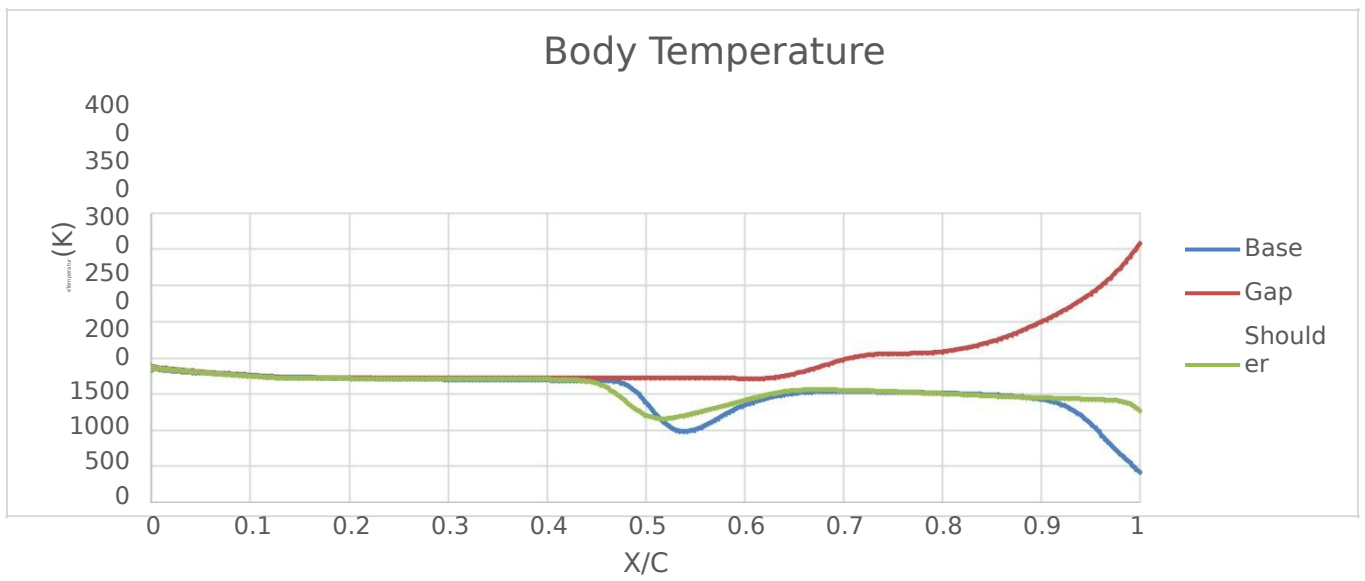
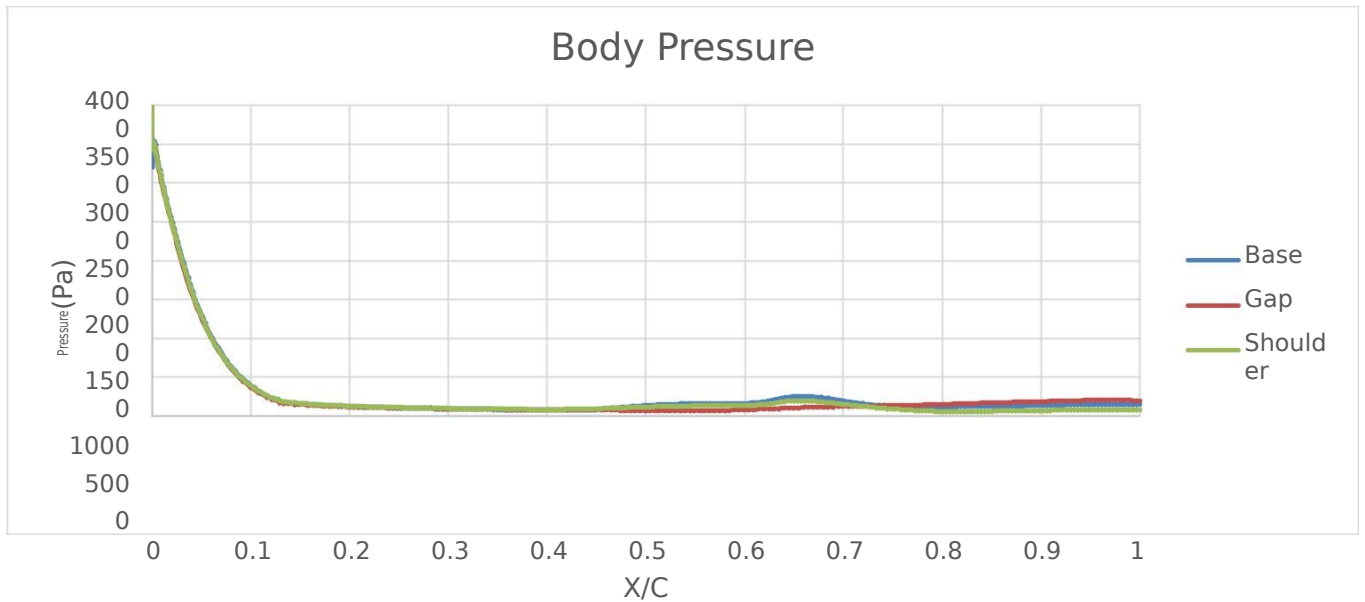


0
.
0
4
0
0 — Base
2 — Gap
0 — Shoulder

0
.
4
0
.
4
5
0
.
5
0
.
5
5
0
.
6
0
.
6
5
0
.
7
0
.
7
5
0
.
8

Distance from
LE (m)

Case D –Body



0

.

4

0

5 Base

Gap

Shoulder

6

0

.

7

0

.

8

0

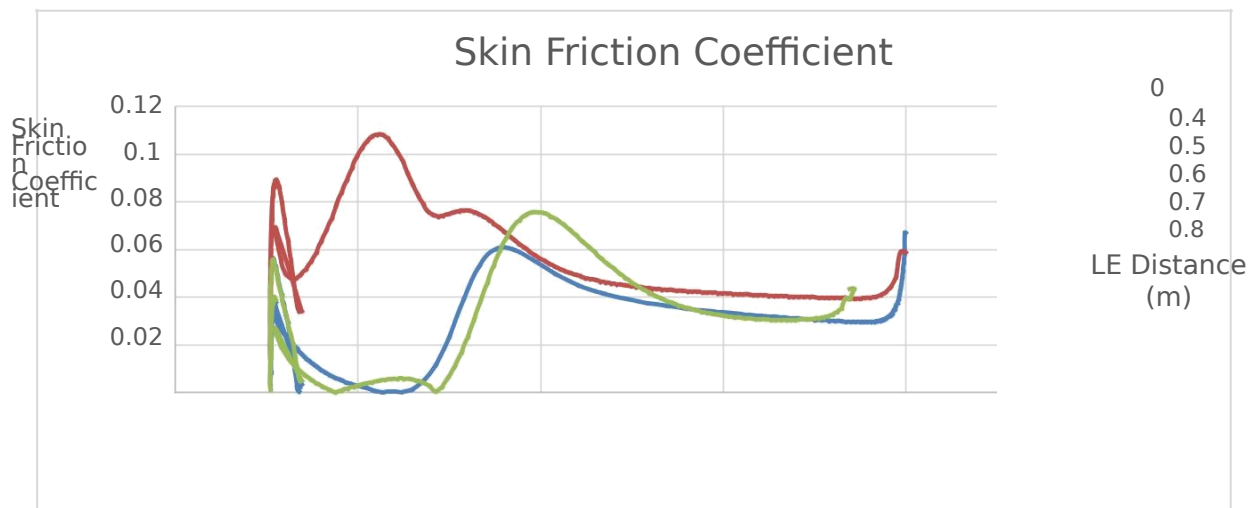
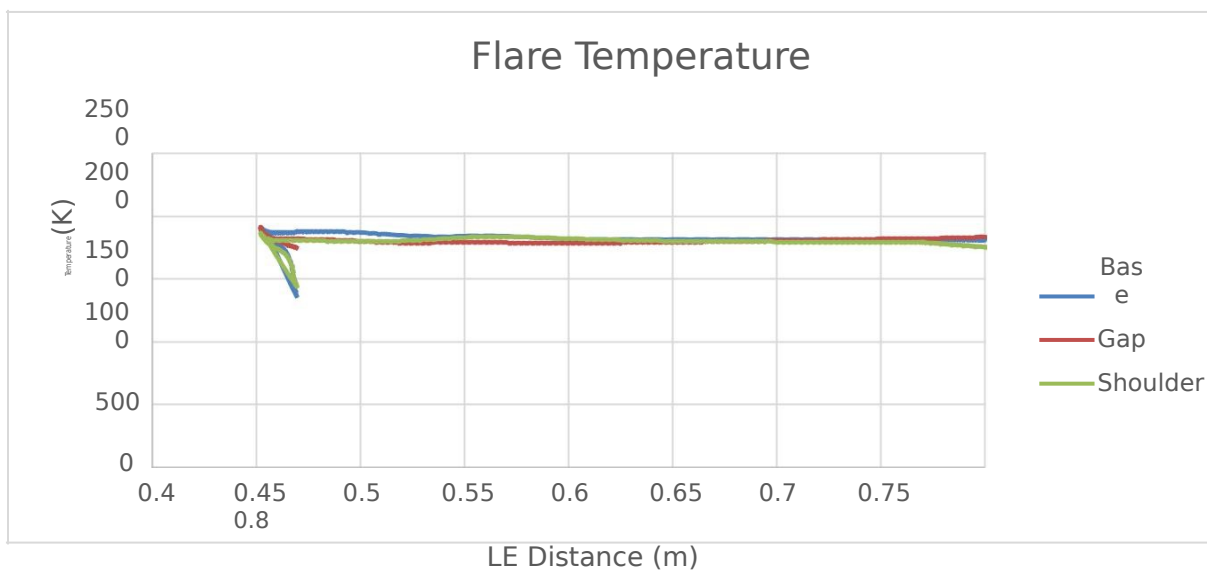
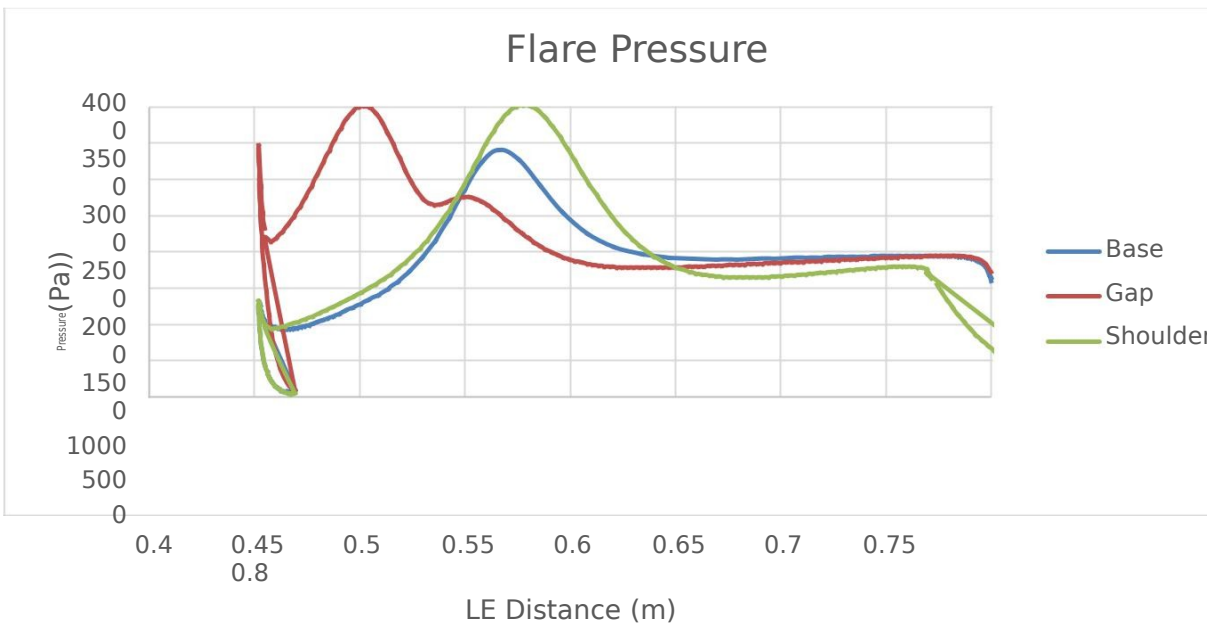
.

9

1

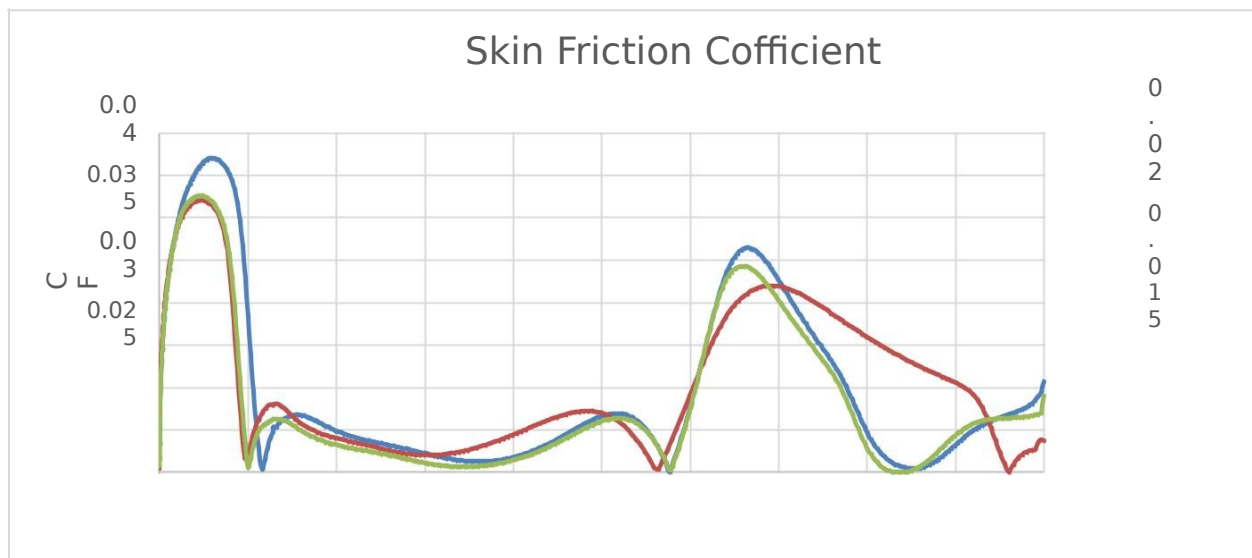
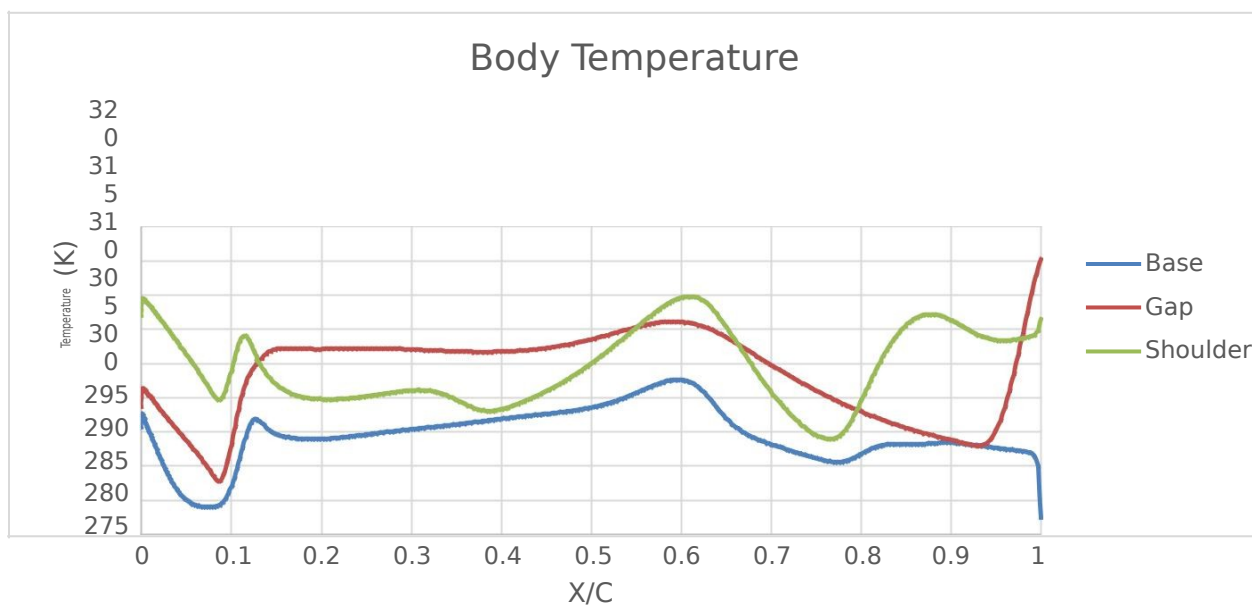
X/C

Case D – Flare



— Base
— Gap
Should
er

Case E – Near Body



0
.
0
1
0
.
0 — Base
0
5 — Gap
0 — Shoulder
0

0

.

1

0

.

2

0

.

3

0

.

4

0

.

5

0

.

6

0

.

7

0

.

8

0

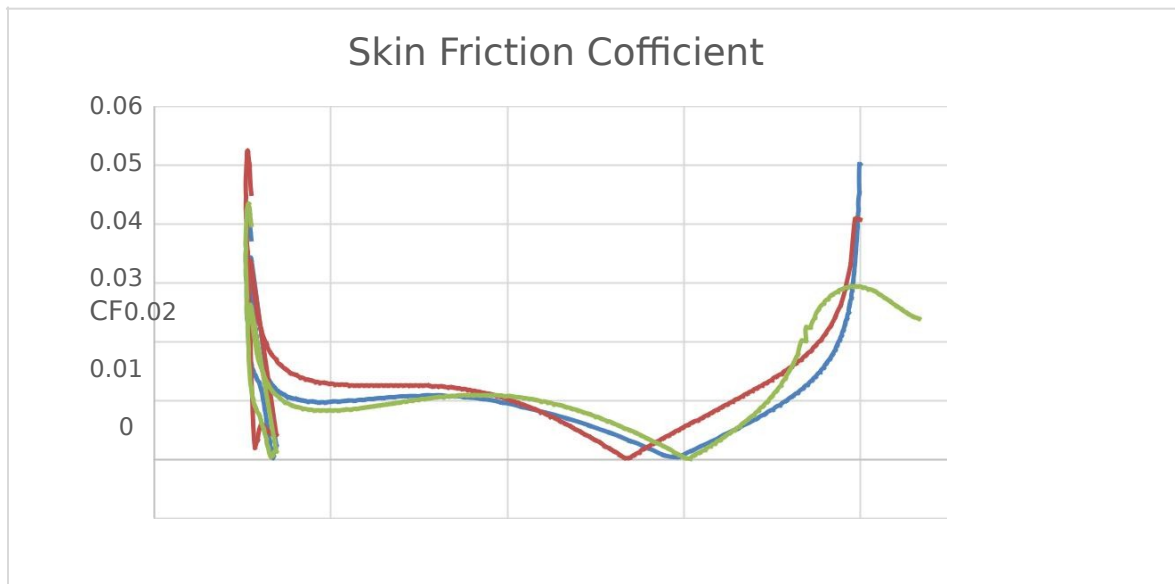
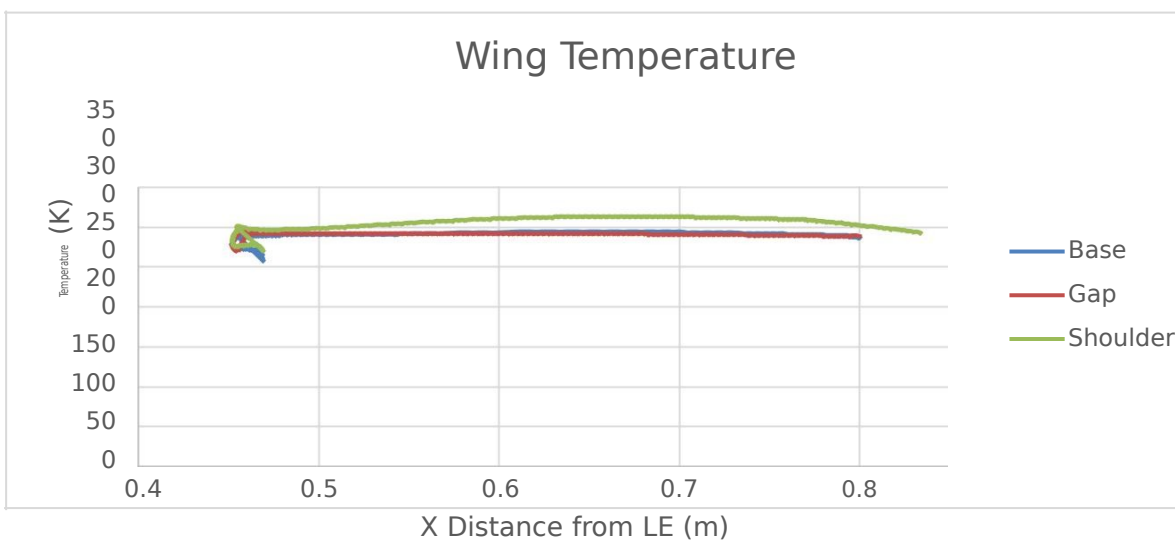
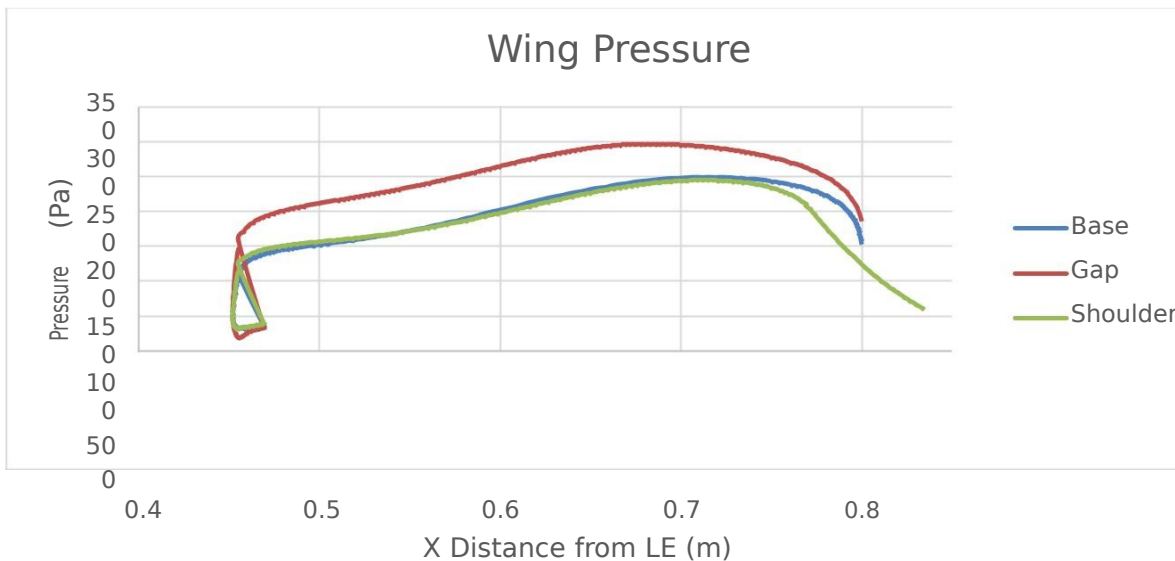
.

9

1

X/C

Case E – Near Wing



- Base
- Gap
- Shoulder

APPENDIX B

BODY PARAMETERIZATION MATLAB SCRIPT

```

% TDRV = [Nose Radius,      # points on nose radius
%         Body Length,     # points on cyl body
%         Body Angle,      # points on fin
%         Fin Angle,       Fin Radius
%         Shoulder Radius, # points on shoulder

%         Aft type - note # points on aft
%         #Points rear shoulder      0          ]

% TDRV = [R_nose,  n_nose;
%         l_body,  n_body;
%         t_body,  n_fin;
%         t_fin,   r_fin;
%         r_shld,  n_shld;
%         d_gap,   d_fin
%         n_shld2, n_aft
%         aft,     0
%         n_shld2          ]

% aft code
% 0 none
% 1 spherical
% 2 conical
% 3 straight
clear all
clc
TDRV = [92  100;      % Nose Radius    n Points on Nose
        623 20;      % Body Length  n Points on Body
         0  25;      % Body Angle   n Points on Fin
        45 507;      % Fin Angle    Total Body radius
         0  10;      % shldr radius n points on shoulder
        20 10;      % Gap distance Fin Rad / half thickness
         3  20;      % Aft type     n Points aft section
         5  0]; % n rear shoulder blank - Units in M Cpmx

= 1.87;

r_nose = TDRV(1,1); n_nose = TDRV(1,2);
l_body = TDRV(2,1); n_body = TDRV(2,2);
t_body = TDRV(3,1); n_fin = TDRV(3,2);
t_fin = TDRV(4,1); r_fin = TDRV(4,2);
r_shld = TDRV(5,1); n_shld = TDRV(5,2);
d_gap = TDRV(6,1); d_fin = TDRV(6,2);
aft = TDRV(7,1); n_aft = TDRV(7,2);
n_shld2= TDRV(8,1);

offset = 0; %

for n = 1:1:n_nose

```

```

theta_nose(n) = (n-1)*90/(n_nose-1);
x_nose(n) = r_nose - r_nose*cosd(theta_nose(n));
y_nose(n) = r_nose*sind(theta_nose(n)); end

for n = 1:1:n_body
x_body(n) = r_nose + n * l_body/n_body;
y_body(n) = r_nose + n * l_body*tand(t_body)/n_body;
end

if aft == 1
disp('Spherical aft body')
xafthinge = x_body(n_body);
yafthinge = 0;
r_aft = r_nose + l_body*sind(t_body);
for n = 1:1:n_aft
theta_aft(n) = (n-1)*90/(n_aft-1);
x_aft(n) = xafthinge + r_aft*sind(theta_aft(n));
y_aft(n) = r_aft*cosd(theta_aft(n));
end
elseif aft == 2
disp('Conical aft body')
r_aft = r_nose + l_body*sind(t_body);
for n = 1:1:n_aft
x_aft(n) = x_body(n_body) + r_aft * (n/n_aft);
y_aft(n) = y_body(n_body) - r_aft * (n/n_aft);
end
elseif aft == 3
disp('Straight aft body')
for n=1:1:n_aft
x_aft(n) = x_body(n_body);
y_aft(n) = y_body(n_body) *(1 - (n/n_body) );
end
else
disp('Aft input not valid')
end

% Start and End Centerpoints for fin radius
SBx = l_body + 2*r_nose;
SBY = r_fin-d_fin;
SAy = r_nose + tand(t_body)*offset + d_fin + d_gap;
SAx = SBx - (SBY - SAy)/tand(t_fin);

if r_shld == 0 %*****Straight Fin Generation*****
for n = 1:1:n_shld+1 % Leading side fin tip (A)
t_shld(n) = t_fin - 90 - 180*(n-1)/n_shld;
xtipa(n) = SAx + d_fin*cosd(t_shld(n)); ytipa(n)
= SAy + d_fin*sind(t_shld(n));
end
for n = 1:1:n_shld+1 % Trailing side fin tip (B)
t_shld(n) = t_fin + 90 - 180*(n-1)/n_shld; xtipb(n)
= SBx + d_fin*cosd(t_shld(n)); ytipb(n) = SBY +
d_fin*sind(t_shld(n));
end

```

```

cle = cosd(t_fin+90); % Initialize angles for fin surfaces
sle = sind(t_fin+90);
cte = cosd(t_fin-90);
ste = sind(t_fin-90);
for n = 1:1:n_fin
xfinab(n) = SAx + (SBx-SAx)*(n)/n_fin; % Fin center coords
yfinab(n) = SAy + (SBy-SAy)*(n)/n_fin;
xLE(n) = xfinab(n) + d_fin*cle; % Leading side
yLE(n) = yfinab(n) + d_fin*sle;
xTE(n) = xfinab(n) + d_fin*cte; % Trailing side
yTE(n) = yfinab(n) + d_fin*ste;
end

% Newtonian Drag (straight fin)*****
Cp = zeros(n_nose,1); Cp(1) = 2; cdn = 0; t_cp(1) = 90;
for n = 2:1:n_nose % Nose
dy(n) = y_nose(n) - y_nose(n-1);
dx(n) = x_nose(n) - x_nose(n-1);
t_cp(n) = 180 - atand(dy(n)/dx(n));
Cp(n) = Cpmax*sind(t_cp(n))*sind(t_cp(n));
cdn = cdn + Cp(n) * dy(n) / r_fin ;
end
cdt = 2 * cdn * d_fin/r_nose; % Fin Tips
Cp_fin = 2 * sind(180 - t_fin)^2; % Fin Body
cdf = Cp_fin * (yLE(n_fin) - yLE(1)) / r_fin ;

Cd_Newt = cdf+cdt+cdn
% *****
x1a = xtipa; y1a = ytipa; % Organize & Concat. Surfaces
x1b = xLE; y1b = yLE;
x1c = xtipb; y1c = ytipb;
x1d = fliplr(xTE); y1d = fliplr(yTE);
x1 = horzcat(x1a,x1b,x1c,x1d);
y1 = horzcat(y1a,y1b,y1c,y1d);

else % ***** Rounded Fin Generation *****
Sbx = SBx; % Trailing Edge Tip Hinge
Sby = SBy - r_shld;
for n = 1:1:n_shld
t_rad(n)= 90 + t_fin - (n-1)*t_fin/n_shld; % Fin spine angle
xrad(n) = Sbx + r_shld*cosd(t_rad(n)); % Shoulder centerline
yrad(n) = Sby + r_shld*sind(t_rad(n));
xfin(n) = xrad(n) + d_fin*cosd(t_rad(n)); % LE Shoulder Surface
yfin(n) = yrad(n) + d_fin*sind(t_rad(n)); %
xfinr(n) = xrad(n) + d_fin*cosd(t_rad(n)+180); % TE ""
yfinr(n) = yrad(n) + d_fin*sind(t_rad(n)+180);
end
for n = 1:1:n_shld+1
t_shld(n) = 180 - 180*(n-1)/n_shld; % TE side tip
xtipb(n) = SBx + d_fin*sind(t_shld(n));
ytipb(n) = SBy + d_fin*cosd(t_shld(n));
end
SAy = r_nose + d_gap + d_fin; % LE shoulder hinge
SAx = xfin(1) - (yfin(1) - SAy)/tand(t_fin);

```

```

for n = 1:1:n_shld+1
t_shld(n) = t_fin - 90 - 180*(n-1)/n_shld;
xtipa(n) = SAx + d_fin*cosd(t_shld(n)); % LE Tip surface
ytipa(n) = SAy + d_fin*sind(t_shld(n));
end
cle = cosd(t_fin+90); % Initialize fin surface angles
sle = sind(t_fin+90);
cte = cosd(t_fin-90);
ste = sind(t_fin-90);
for n = 1:1:n_fin
xfinab(n) = SAx +(xrad(1)-SAx)*(n)/n_fin; % Fin centerline
yfinab(n) = SAy +(yrad(1)-SAy)*(n)/n_fin;
xLE(n) = xfinab(n) + d_fin*cle; % Leading edge coords
yLE(n) = yfinab(n) + d_fin*sle;
xTE(n) = xfinab(n) + d_fin*cte; % Trailing edge coords
yTE(n) = yfinab(n) + d_fin*ste;
end

% Newtonian Drag (rounded fin)***** Cp
= zeros(n_nose,1); Cp(1) = 2; cdn = 0; t_cp(1) = 90;
for n = 2:1:n_nose % Nose
dy(n) = y_nose(n) - y_nose(n-1);
dx(n) = x_nose(n) - x_nose(n-1);
t_cp(n) = 180 - atand(dy(n)/dx(n));
Cp(n) = Cpmax*sind(t_cp(n))*sind(t_cp(n));
cdn = cdn + Cp(n) * dy(n) / r_fin ;
end
cdt = cdn * d_fin/r_nose; % Tip
Cp_fin = 2 * sind(180 - t_fin)^2;
cdf = Cp_fin * (yLE(n_fin) - yLE(1)) / r_fin ; % Fin Body
Cp = zeros(n_shld,1); Cp(1) = Cp_fin; cds = 0; t_cp(1) = t_fin;
for n = 2:1:n_shld
dy(n) = yfin(n) - yfin(n-1);
dx(n) = xfin(n) - xfin(n-1);
t_cp(n) = 180 - atand(dy(n)/dx(n));
Cp(n) = Cpmax*sind(t_cp(n))*sind(t_cp(n));
cds = cds + Cp(n) * dy(n) / r_fin ; % Shoulder
end

Cd_Newt = cdf+cdt+cdn+cds % Total Cd
% *****
x1a=xtipb; y1a= ytipb; % Organize & concat
x1b =fliplr(xfin); y1b= fliplr(yfin); % all fin surfaces
x1c=fliplr(xLE); y1c= fliplr(yLE);
x1d =fliplr(xtipa); y1d= fliplr(ytipa);
x1e =xTE; y1e= yTE;
x1f=xfinr; y1f= yfinr;
x1 = horzcat(x1a,x1b,x1c,x1d,x1e,x1f);
y1 = horzcat(y1a,y1b,y1c,y1d,y1e,y1f);
x1 = x1 - offset;
end
% *****
x=horzcat(x_nose,x_body,x_aft);
y=horzcat(y_nose,y_body,y_aft);
plot(x,y,x1,y1) % Plot Results axis([0
1.5*1_body 0 1.5*r_fin])

```

```
zlength = length(vertcat(x',x1'));
z = zeros(zlength,1);
data = [vertcat(x',x1') vertcat(y',y1') z];
a = length(data');
b = 1;
fileID = fopen('TDRVlin.lin','w');
fprintf(fileID, '%6u %6u\r\n',a,b);
fprintf(fileID, '%6.5f %6.5f %6.5f\r\n', data');
fclose(fileID);

zlength = length(x');
z = zeros(zlength,1);
data = [x',y',z];
a = length(data');
b = 1;
fileID = fopen('TDRVlinA.lin','w');
fprintf(fileID, '%6u %6u\r\n',a,b);
fprintf(fileID, '%6.5f %6.5f %6.5f\r\n', data');
fclose(fileID);

zlength = length(x1');
z = zeros(zlength,1);
data = [x1' y1' z;
        x1(1) y1(1) 0];
a = length(data');
b = 1;
fileID = fopen('TDRVlinB.lin','w');
fprintf(fileID, '%6u %6u\r\n',a,b);
fprintf(fileID, '%6.5f %6.5f %6.5f\r\n', data');
fclose(fileID);
```

APPENDIX D

TRAJECTORY CALCULATION MATLAB SCRIPT

```

% kg-m-s - yent degrees, y rad
% entry interface 141.8km entry v ~ 7km/s
%plot(y,q_s,'DisplayName','q* stag (W/m^2)' y,V,'DisplayName',
%'Velocity (m/s)', y,q,'DisplayName','Dyn. Press (Pa)') clc
clear all
H = 140000; g = 3.8; % atm. interface alt. (m); mars grav. (m/s^2)
yent = 13.25; % atm. interface angle (deg)
y = yent*pi/180; sy =sin(y); cy =cos(y); %abbreviate sin/cos
Rn = 0.092; Rtot = 0.507; % LE radius; total body radius A =
[pi*(Rtot).^2]; % Body area
Ve = 7000; % Atm. interface vel. (m/s)
B = 1/11100; % Mars atm. constant
rho0 = 0.0125; % Mars surface density (kg/m^3)
k = 1.9027E-4; % Sutton-Graves Constant
Cf = 0.2; % Stagnation skin fric coefficient
M = 20; % Probe mass (kg)
CD = 0.9; % Probe drag coeff
bc = M/(CD*A); bc = [27.7]; mmax=size(bc,2);
nmax = 28; ystep = H/nmax; % Number of samples;
C = H*rho0/(2*bc*sy);
y=zeros(nmax,mmax); x=zeros(nmax,mmax); t=zeros(nmax,mmax);
V=zeros(nmax,mmax); rho=zeros(nmax,mmax); a=zeros(nmax,mmax);
qs_max=zeros(mmax,1); Qs=zeros(mmax,1); h_qmax=zeros(mmax,1);
decmax=zeros(mmax,1); ydecmax=zeros(mmax,1);
q=zeros(nmax,mmax); q_s=zeros(nmax,mmax); vds2 = V; vb2 = V;
qds2 = q_s; qb2 = q_s;
ads2 = a; ab2 = a;
n = 1; m = 1; % initialize count & arrays
alt = [20000 35000 50000 65000 80000];
den = [2.2E-3 4.25E-4 8.26E-5 1.33E-5 1.88E-6];
qsim= [188 34900 123000 71900 29300]; vel =
[400 3000 6000 6800 7000];

for m = 1:1:mmax
for h = H:-ystep:0
y(n,m) = h ; x(n,m) = y(n,m)*cy/sy;
rho(n,m) = rho0*exp(-y(n)*B);
V(n,m) = Ve*exp((-exp(-B*y(n))*CD*rho0*A)/(2*B*m*sy));
a(n,m) = exp(-B*y(n))*(rho0*V(n)*V(n)) / (2*bc); q(n,m)
= 0.5*rho(n)*V(n).^2;
q_s(n,m) = (6.8E-6)*sqrt(rho(n,m)/Rn)*(V(n,m).^3);
t(n) = ystep/(V(n)*sy);
vds2(n)=7000*exp((exp(B*y(n))*1.05*rho0*(pi*0.175.^2))/(2*B*2.73*sind(13.25)));
qds2(n) = (6.8E-6)*sqrt(rho(n,m)/0.0875)*(vds2(n,m).^3);
ads2(n) = exp(-B*y(n))*(rho0*vds2(n).^2) / (2*27);
vb2(n) = 7000*exp((exp(B*y(n))*1.05*rho0*(pi*0.45.^2))/(2*B*60*sind(13.25)));
qb2(n) = (6.8E-6)*sqrt(rho(n,m)/0.417)*(vb2(n,m).^3);
ab2(n) = exp(-B*y(n))*(rho0*vds2(n).^2) / (2*70);
n = n+1;
end
qs_max(m) = k*sqrt(Rn.^-1)*sqrt(bc(m)*sy/(3*H))*(0.6055*Ve.^3);

```

```

Qs(m) = k*Ve*Ve*[sqrt(bc(m)*pi*H/(rho0*Rn*sy))];
h_qmax(m) = -H*log(bc(m)*sy/(3*H*rho0));
decmax(m) = B*Ve*Ve*sy/(2*exp(1));
ydecmax(m) = (1/B)*log(rho0/(B*bc(m)*sy));
Qsb2(m) = k*Ve*Ve*[sqrt(70*pi*H/(rho0*.417*sy))];
Qsds2(m) = k*Ve*Ve*[sqrt(27*pi*H/(rho0*.0875*sy))];
n = 1;
end
yp = y(:,1);
subplot(2,1,1)
p1 = plot(yp,q_s,alt,qsim,'ro',yp,qds2,'--',yp,qb2,':');
xlabel('Altitude (m)')
ylabel('Stagnation Point Heat Flux (W/m^2)')
subplot(2,1,2)
p2 = plot(yp,V,alt,vel,'ro',yp,vds2,'--',yp,vb2,':');
xlabel('Altitude (m)');
ylabel('Velocity(m/s)');
legend('SCRAMP','Test Cases','DS-2','Beagle 2','location','southeast')

```